

The radio/gamma-ray connection in Active Galactic Nuclei in the era of the *Fermi* Large Area Telescope

M. Ackermann², M. Ajello², A. Allafort², E. Angelakis³, M. Axelsson^{4,5,6}, L. Baldini⁷, J. Ballet⁸,
G. Barbiellini^{9,10}, D. Bastieri^{11,12}, R. Bellazzini⁷, B. Berenji², R. D. Blandford², E. D. Bloom²,
E. Bonamente^{13,14}, A. W. Borgland², A. Bouvier¹⁵, J. Bregeon⁷, A. Brez⁷, M. Brigida^{16,17},
P. Bruel¹⁸, R. Buehler², S. Buson^{11,12}, G. A. Caliendo¹⁹, R. A. Cameron², A. Cannon^{20,21},
P. A. Caraveo²², J. M. Casandjian⁸, E. Cavazzuti²³, C. Cecchi^{13,14}, E. Charles², A. Chekhtman²⁴,
C. C. Cheung²⁵, S. Ciprini¹⁴, R. Claus², J. Cohen-Tanugi²⁶, S. Cutini²³, F. de Palma^{16,17},
C. D. Dermer²⁷, E. do Couto e Silva², P. S. Drell², R. Dubois², D. Dumora²⁸, L. Escande^{28,29},
C. Favuzzi^{16,17}, S. J. Fegan¹⁸, W. B. Focke², P. Fortin¹⁸, M. Frailis^{30,31}, L. Fuhrmann³,
Y. Fukazawa³², P. Fusco^{16,17}, F. Gargano¹⁷, D. Gasparrini²³, N. Gehrels²⁰, N. Giglietto^{16,17},
P. Giommi²³, F. Giordano^{16,17}, M. Giroletti^{33,1}, T. Glanzman², G. Godfrey², P. Grandi³⁴,
I. A. Grenier⁸, S. Guiriec³⁵, D. Hadasch¹⁹, M. Hayashida², E. Hays²⁰, S. E. Healey²,
G. Jóhannesson³⁶, A. S. Johnson², T. Kamae², H. Katagiri³², J. Kataoka³⁷, J. Knödseder³⁸,
M. Kuss⁷, J. Lande², S.-H. Lee², F. Longo^{9,10}, F. Loparco^{16,17}, B. Lott²⁸, M. N. Lovellette²⁷,
P. Lubrano^{13,14}, A. Makeev²⁴, W. Max-Moerbeck³⁹, M. N. Mazziotta¹⁷, J. E. McEnery^{20,40},
J. Mehault²⁶, P. F. Michelson², T. Mizuno³², C. Monte^{16,17}, M. E. Monzani², A. Morselli⁴¹,
I. V. Moskalenko², S. Murgia², M. Naumann-Godo⁸, S. Nishino³², P. L. Nolan², J. P. Norris⁴²,
E. Nuss²⁶, T. Ohsugi⁴³, A. Okumura⁴⁴, N. Omodei², E. Orlando^{45,2}, J. F. Ormes⁴², M. Ozaki⁴⁴,
D. Paneque^{46,2}, V. Pavlidou^{39,1}, V. Pelassa²⁶, M. Pepe^{13,14}, M. Pesce-Rollins⁷, M. Pierbattista⁸,
F. Piron²⁶, T. A. Porter², S. Rainò^{16,17}, M. Razzano⁷, A. Readhead³⁹, A. Reimer^{47,2,1},
O. Reimer^{47,2}, J. L. Richards³⁹, R. W. Romani², H. F.-W. Sadrozinski¹⁵, J. D. Scargle⁴⁸,
C. Sgrò⁷, E. J. Siskind⁴⁹, P. D. Smith⁵⁰, G. Spandre⁷, P. Spinelli^{16,17}, M. S. Strickman²⁷,
D. J. Suson⁵¹, H. Takahashi⁴³, T. Tanaka², G. B. Taylor⁵², J. G. Thayer², J. B. Thayer²,
D. J. Thompson²⁰, D. F. Torres^{19,53}, G. Tosti^{13,14}, A. Tramacere^{2,54,55}, E. Troja^{20,56},
J. Vandenbroucke², G. Vianello^{2,54}, V. Vitale^{41,57}, A. P. Waite², P. Wang², B. L. Winer⁵⁰,
K. S. Wood²⁷, Z. Yang^{58,6}, M. Ziegler¹⁵

¹Corresponding authors: M. Giroletti, giroletti@ira.inaf.it; V. Pavlidou, pavlidou@astro.caltech.edu; A. Reimer, afr@slac.stanford.edu.

²W. W. Hansen Experimental Physics Laboratory, Kavli Institute for Particle Astrophysics and Cosmology, Department of Physics and SLAC National Accelerator Laboratory, Stanford University, Stanford, CA 94305, USA

³Max-Planck-Institut für Radioastronomie, Auf dem Hügel 69, 53121 Bonn, Germany

⁴Department of Astronomy, Stockholm University, SE-106 91 Stockholm, Sweden

⁵Lund Observatory, SE-221 00 Lund, Sweden

⁶The Oskar Klein Centre for Cosmoparticle Physics, AlbaNova, SE-106 91 Stockholm, Sweden

⁷Istituto Nazionale di Fisica Nucleare, Sezione di Pisa, I-56127 Pisa, Italy

⁸Laboratoire AIM, CEA-IRFU/CNRS/Université Paris Diderot, Service d’Astrophysique, CEA Saclay, 91191 Gif sur Yvette, France

⁹Istituto Nazionale di Fisica Nucleare, Sezione di Trieste, I-34127 Trieste, Italy

¹⁰Dipartimento di Fisica, Università di Trieste, I-34127 Trieste, Italy

¹¹Istituto Nazionale di Fisica Nucleare, Sezione di Padova, I-35131 Padova, Italy

¹²Dipartimento di Fisica “G. Galilei”, Università di Padova, I-35131 Padova, Italy

¹³Istituto Nazionale di Fisica Nucleare, Sezione di Perugia, I-06123 Perugia, Italy

¹⁴Dipartimento di Fisica, Università degli Studi di Perugia, I-06123 Perugia, Italy

¹⁵Santa Cruz Institute for Particle Physics, Department of Physics and Department of Astronomy and Astrophysics, University of California at Santa Cruz, Santa Cruz, CA 95064, USA

¹⁶Dipartimento di Fisica “M. Merlin” dell’Università e del Politecnico di Bari, I-70126 Bari, Italy

¹⁷Istituto Nazionale di Fisica Nucleare, Sezione di Bari, 70126 Bari, Italy

¹⁸Laboratoire Leprince-Ringuet, École polytechnique, CNRS/IN2P3, Palaiseau, France

¹⁹Institut de Ciències de l’Espai (IEEC-CSIC), Campus UAB, 08193 Barcelona, Spain

²⁰NASA Goddard Space Flight Center, Greenbelt, MD 20771, USA

²¹University College Dublin, Belfield, Dublin 4, Ireland

²²INAF-Istituto di Astrofisica Spaziale e Fisica Cosmica, I-20133 Milano, Italy

²³Agenzia Spaziale Italiana (ASI) Science Data Center, I-00044 Frascati (Roma), Italy

²⁴College of Science, George Mason University, Fairfax, VA 22030, resident at Naval Research Laboratory, Washington, DC 20375, USA

²⁵National Research Council Research Associate, National Academy of Sciences, Washington, DC 20001, resident at Naval Research Laboratory, Washington, DC 20375, USA

²⁶Laboratoire de Physique Théorique et Astroparticules, Université Montpellier 2, CNRS/IN2P3, Montpellier, France

²⁷Space Science Division, Naval Research Laboratory, Washington, DC 20375, USA

²⁸Université Bordeaux 1, CNRS/IN2P3, Centre d’Études Nucléaires de Bordeaux Gradignan, 33175 Gradignan,

France

²⁹CNRS/IN2P3, Centre d’Études Nucléaires Bordeaux Gradignan, UMR 5797, Gradignan, 33175, France

³⁰Dipartimento di Fisica, Università di Udine and Istituto Nazionale di Fisica Nucleare, Sezione di Trieste, Gruppo Collegato di Udine, I-33100 Udine, Italy

³¹Osservatorio Astronomico di Trieste, Istituto Nazionale di Astrofisica, I-34143 Trieste, Italy

³²Department of Physical Sciences, Hiroshima University, Higashi-Hiroshima, Hiroshima 739-8526, Japan

³³INAF Istituto di Radioastronomia, 40129 Bologna, Italy

³⁴INAF-IASF Bologna, 40129 Bologna, Italy

³⁵Center for Space Plasma and Aeronomic Research (CSPAR), University of Alabama in Huntsville, Huntsville, AL 35899, USA

³⁶Science Institute, University of Iceland, IS-107 Reykjavik, Iceland

³⁷Research Institute for Science and Engineering, Waseda University, 3-4-1, Okubo, Shinjuku, Tokyo, 169-8555 Japan

³⁸Centre d’Étude Spatiale des Rayonnements, CNRS/UPS, BP 44346, F-30128 Toulouse Cedex 4, France

³⁹Cahill Center for Astronomy and Astrophysics, California Institute of Technology, Pasadena, CA 91125, USA

⁴⁰Department of Physics and Department of Astronomy, University of Maryland, College Park, MD 20742, USA

⁴¹Istituto Nazionale di Fisica Nucleare, Sezione di Roma “Tor Vergata”, I-00133 Roma, Italy

⁴²Department of Physics and Astronomy, University of Denver, Denver, CO 80208, USA

⁴³Hiroshima Astrophysical Science Center, Hiroshima University, Higashi-Hiroshima, Hiroshima 739-8526, Japan

⁴⁴Institute of Space and Astronautical Science, JAXA, 3-1-1 Yoshinodai, Chuo-ku, Sagami-hara, Kanagawa 252-5210, Japan

⁴⁵Max-Planck Institut für extraterrestrische Physik, 85748 Garching, Germany

⁴⁶Max-Planck-Institut für Physik, D-80805 München, Germany

⁴⁷Institut für Astro- und Teilchenphysik and Institut für Theoretische Physik, Leopold-Franzens-Universität Innsbruck, A-6020 Innsbruck, Austria

⁴⁸Space Sciences Division, NASA Ames Research Center, Moffett Field, CA 94035-1000, USA

⁴⁹NYCB Real-Time Computing Inc., Lattingtown, NY 11560-1025, USA

⁵⁰Department of Physics, Center for Cosmology and Astro-Particle Physics, The Ohio State University, Columbus, OH 43210, USA

⁵¹Department of Chemistry and Physics, Purdue University Calumet, Hammond, IN 46323-2094, USA

⁵²University of New Mexico, MSC07 4220, Albuquerque, NM 87131, USA

⁵³Institució Catalana de Recerca i Estudis Avançats (ICREA), Barcelona, Spain

⁵⁴Consorzio Interuniversitario per la Fisica Spaziale (CIFS), I-10133 Torino, Italy

⁵⁵INTEGRAL Science Data Centre, CH-1290 Versoix, Switzerland

⁵⁶NASA Postdoctoral Program Fellow, USA

ABSTRACT

We present a detailed statistical analysis of the correlation between radio and gamma-ray emission of the Active Galactic Nuclei (AGN) detected by *Fermi* during its first year of operation, with the largest datasets ever used for this purpose. We use both archival interferometric 8.4 GHz data (from the VLA and ATCA, for the full sample of 599 sources) and concurrent single-dish 15 GHz measurements from the Owens Valley Radio Observatory (OVRO, for a sub sample of 199 objects). Our unprecedentedly large sample permits us to assess with high accuracy the statistical significance of the correlation, using a surrogate-data method designed to simultaneously account for common-distance bias and the effect of a limited dynamical range in the observed quantities. We find that the statistical significance of a positive correlation between the cm radio and the broad band ($E > 100$ MeV) gamma-ray energy flux is very high for the whole AGN sample, with a probability $< 10^{-7}$ for the correlation appearing by chance. Using the OVRO data, we find that concurrent data improve the significance of the correlation from 1.6×10^{-6} to 9.0×10^{-8} . Our large sample size allows us to study the dependence of correlation strength and significance on specific source types and gamma-ray energy band. We find that the correlation is very significant (chance probability $< 10^{-7}$) for both FSRQs and BL Lacs separately; a dependence of the correlation strength on the considered gamma-ray energy band is also present, but additional data will be necessary to constrain its significance.

Subject headings: Gamma rays: galaxies – Radio continuum: galaxies – Galaxies: active – Galaxies: jets – BL Lacertae objects: general – quasars: general

1. Introduction

After more than 1 year of scanning the gamma-ray sky by the Large Area Telescope (LAT) onboard the *Fermi* Gamma-ray Space Telescope (*Fermi*), the most extreme class of Active Galactic Nuclei (AGN), blazars (used to refer collectively to BL Lac objects, hereafter BL Lacs, and flat spectrum radio quasars, hereafter FSRQs), remain among the most numerous gamma-ray source populations. Indeed, the First *Fermi*-LAT catalog of gamma-ray sources (hereafter 1FGL, Abdo et al. 2010a) includes more than 1400 sources and about half of them are believed to be AGNs (Abdo et al. 2010d) with most of them identified via radio catalogs (e.g., CRATES; Healey et al. 2007). More than 370 high-latitude ($|b| > 10^\circ$) sources in the 1FGL remain unidentified.

⁵⁷Dipartimento di Fisica, Università di Roma “Tor Vergata”, I-00133 Roma, Italy

⁵⁸Department of Physics, Stockholm University, AlbaNova, SE-106 91 Stockholm, Sweden

41 Blazars have been observed to emit at all energies, from the radio band up to very-high energy
 42 gamma-rays. Many of the gamma-ray blazars detected so far appear to emit the bulk of their
 43 total radiative output at gamma-ray energies. Strong variability across the whole electromagnetic
 44 spectrum and on various time scales is considered as one of the most intriguing properties of this
 45 source type. In particular their high-energy emission can easily vary by more than an order of
 46 magnitude from one observing epoch to the next (e.g. Mukherjee et al. 1997; Abdo et al. 2010c),
 47 and variability time scales at high energies are mostly much shorter (even down to just a few
 48 minutes in the TeV band, e.g. Aharonian et al. 2007) than in the long wavelength bands.

49 The high inferred bolometric luminosities, rapid variability, and apparent superluminal motions
 50 observed from a range of blazars provide compelling evidence that the non-thermal emission of
 51 blazars originates from a region which is propagating relativistically along a jet directed at a small
 52 angle with respect to our line of sight.

53 Because most identified gamma-ray AGN are classified as radio-loud objects, a luminosity
 54 correlation between those two wavebands appears possible. If proved true, constraints on the
 55 physics and location of the jet emission from such AGN may be deduced. Many attempts have
 56 been made in the past to investigate correlations between radio (cm)- and gamma-ray luminosities of
 57 AGN (e.g., Stecker et al. 1993; Padovani et al. 1993; Salamon & Stecker 1994; Taylor et al. 2007).
 58 However, the relation has not been conclusively demonstrated when all relevant biases and selection
 59 effects are taken into account (see, e.g. Mücke et al. 1997).

60 For example, while luminosities represent the intrinsic source property, as opposed to fluxes,
 61 the use of luminosities always introduces a redshift bias in samples which cover a wide distance
 62 range since luminosities are strongly correlated with redshift (Elvis et al. 1978). Such redshift
 63 dependence can be removed by means of a partial correlation analysis (see e.g., Dondi & Ghisellini
 64 1995). On the other hand, intrinsic correlations between the gamma-ray and radio luminosities
 65 may be smeared out, or even lost in the corresponding flux diagrams whereas artificial flux-flux
 66 correlations can be induced due to the effect of a common distance modulation of gamma-ray and
 67 radio luminosities (the “common-distance” bias, see e.g. Pavlidou et al. 2011).

68 Samples that are strongly sensitivity limited restrict the populated region in the luminosity-
 69 luminosity diagram to a narrow band, thereby causing serious biases. Therefore, Feigelson & Berg
 70 (1983) proposed to include all upper limits to avoid artificial correlations and incorrect conclusions
 71 (Schmitt 1985). However, upper limits are usually not distributed randomly in the flux-flux or
 72 luminosity-luminosity plane, but are localized in a particular area. In this case, a survival analysis
 73 may give misleading results (Isobe 1989). Furthermore, this analysis cannot account for biases
 74 caused by misidentification of sources or by truncation effects. Finally, the use of rank correla-
 75 tion tests (e.g., Kendall’s τ , Spearman rank correlation coefficient ρ) complicates the inclusion of
 76 observational uncertainties.

77 Another problem is the data and source selection. Blazars are inherently variable sources in the
 78 radio as well as the gamma-ray band on a broad range of time scales. Simultaneous observations are

79 therefore the only appropriate data for a correlation analysis. However, due to the lack of such data,
80 the mean (e.g., Padovani et al. 1993) or the brightest flux values (e.g., Dondi & Ghisellini 1995)
81 have often been used instead. As a consequence the dynamical range in the luminosity-luminosity
82 plane is significantly reduced in those cases, and can hence mimic a correlation (Mücke et al. 1997).

83 The question of a correlation between the radio and GeV band on the basis of *Fermi* data has re-
84 cently generated a lot of interest and has been the subject of a series of investigations (Kovalev et al.
85 2009; Ghirlanda et al. 2010, 2011; Mahony et al. 2010). However, these studies have been gener-
86 ally limited to a small fraction of the *Fermi*-detected AGN and have used non-simultaneous or
87 quasi-simultaneous measurements. Moreover, these works have primarily addressed the issue of the
88 *apparent strength* of the correlation, rather than that of its *intrinsic significance*, which requires a
89 dedicated method of statistical analysis. In this paper, we will use the term "apparent correlation
90 strength" for measures of the tightness of a correlation between radio and gamma-ray *fluxes* (such
91 as various correlation coefficients) as seen in the raw data, without applying any correction or sig-
92 nificance assessment to address common-distance bias and the limits on the measured fluxes (the
93 issue of "censored data"). In contrast, we will use the term "intrinsic correlation" for the physical
94 correlation between radio and gamma-ray (time-averaged) luminosities, in the limit of an infinite
95 survey, and "intrinsic correlation significance" for the statistical significance of the claim that a
96 specific dataset exhibits a non-zero intrinsic correlation.

97 In this paper, we revisit this topic exploiting for the first time the *Fermi*-LAT data in full, in two
98 ways. First, we make use of archival data for about 600 sources, a dataset more than twice as large
99 as that used in Ghirlanda et al. (2010) and Mahony et al. (2010). Second, we take advantage of the
100 large set of concurrent measurements provided by the OVRO monitoring program (Richards et al.
101 2010). The pre-*Fermi*-launch OVRO sample included ~ 200 blazars that are included in the 1FGL
102 catalog, and for which average 15 GHz fluxes measured *concurrently* with the 1FGL gamma-ray
103 fluxes can be calculated. In addition, we exploit a new statistical method (Pavlidou et al. 2011) to
104 assess the significance of the correlation coefficients.

105 The paper is structured as follows: in Sect. 2, we present the gamma-ray and radio data and
106 the association procedure; the results are presented in Sect. 3 and discussed in Sect. 4 using a
107 dedicated statistical analysis based on the method of surrogate data. A more general discussion is
108 given in Sect. 5 and the main conclusions are summarized in Sect. 6.

109 In the following, we use a Λ CDM cosmology with $h = 0.71$, $\Omega_m = 0.27$, and $\Omega_\Lambda = 0.73$
110 (Komatsu et al. 2009). The radio spectral index is defined such that $S(\nu) \propto \nu^{-\alpha}$ and the gamma-
111 ray photon index Γ such that $dN_{\text{photon}}/dE \propto E^{-\Gamma}$.

2. Observations and dataset

2.1. Gamma-ray data

The gamma-ray sources in the present paper are a subset of those in the First *Fermi*-LAT catalog (1FGL, Abdo et al. 2010a). The 1FGL is a catalog of high-energy gamma-ray sources detected by the LAT during the first 11 months of the science phase of *Fermi*, i.e. between 2008 August 4 and 2009 July 4. The procedures used in producing the 1FGL catalog are discussed in detail in Abdo et al. (2010a); in total, the 1FGL contains 1451 sources detected and characterized in the 100 MeV to 100 GeV range and belonging to a number of populations of gamma-ray emitters.

In general, associations of gamma-ray sources with lower-energy counterparts necessarily rely on a spatial coincidence between the two. A firm counterpart identification requires the search for correlated variability, which is a major effort in the case of AGNs; therefore, only 5 AGNs are listed as firm identifications by Abdo et al. (2010a), although ongoing studies will undoubtedly expand this set. For the rest, associations in 1FGL use a method for finding correspondence between LAT sources and AGNs based on the calculation of association probabilities using a Bayesian approach implemented in the *gtsrcid* tool included in the LAT *ScienceTools* package. A detailed description and a complete list of the source catalogs used by *gtsrcid* to draw candidate counterparts can be found in Abdo et al. (2010a).

The set of all high-latitude ($|b| > 10^\circ$) 1FGL sources with an AGN association from *gtsrcid* constitutes the First LAT AGN Catalog (1LAC, Abdo et al. 2010d). Some LAT sources are associated with multiple AGNs, and consequently, the catalog includes 709 AGN associations for 671 distinct 1FGL sources. Each source has an association probability P , evaluated by examining the local density of counterparts from a number of source catalogs in the vicinity of the LAT source. The main catalogs used are the Combined Radio All-sky Targeted Eight GHz Survey (CRATES; Healey et al. 2007), the Candidate Gamma-Ray Blazar Survey (CGRaBS; Healey et al. 2008), and the Roma-BZCAT (Massaro et al. 2009). Since a few gamma-ray sources have more than one possible association, and not all associations are highly significant, Abdo et al. (2010d) have further defined an AGN “clean” sample consisting of those AGNs that (1) are the sole AGN associated with the corresponding 1FGL gamma-ray source and (2) have an association probability $P \geq 80\%$; a few sources, “flagged” in the 1FGL catalog as exhibiting some problem, have also been discarded and do not belong in the 1LAC clean sample. This clean sample contains 599 AGNs. In the following analysis, whenever we mention the 1LAC sample, we will always be referring to the clean sample even if we do not state so explicitly.

For each source in the 1FGL (and hence in the 1LAC), Abdo et al. (2010a) have first obtained good estimates of the significance and the overall spectral slope Γ . Then, in order to obtain good estimates of the energy flux, each of the five energy bands (from 100 to 300 MeV, 300 MeV to 1 GeV, 1 to 3 GeV, 3 to 10 GeV, and 10 to 100 GeV) has been fit independently, fixing the spectral index of each source to Γ as derived from the fit over the full interval; finally, the sum of the energy

flux in the five bands provided a reliable estimate of the overall flux.

In sources with a poorly measured flux (88/599), Abdo et al. (2010a) replaced the value from the likelihood analysis with a 2σ upper limit. However, since these sources are significantly detected when the full band is considered, we estimated their energy fluxes from the flux densities at the pivot energies given by Abdo et al. (2010a), and using the tabulated photon indices and the relative uncertainties on the corresponding quantities. All the obtained data are consistent with the 2σ limits and so have been used for our analysis.

We maintain the 1LAC classification of each AGN on the basis of its optical spectrum either as an FSRQ or a BL Lac using the same scheme as in CGRaBS (Healey et al. 2008). In particular, following Stocke et al. (1991), Urry & Padovani (1995), and Marchã et al. (1996), an object is classified as a BL Lac if the equivalent width (EW) of the strongest optical emission line is $< 5 \text{ \AA}$, the optical spectrum shows a Ca II H/K break ratio $C < 0.4$, and the wavelength coverage of the spectrum satisfies $(\lambda_{\text{max}} - \lambda_{\text{min}})/\lambda_{\text{max}} > 1.7$ in order to ensure that at least one strong emission line would have been detected if it were present.

In addition to the optical spectrum classification, the 1LAC blazars are also classified based on the position of the synchrotron peak, following the scheme proposed by Abdo et al. (2010e); we therefore consider also the three following spectral types: low-synchrotron-peaked blazars (LSP, $\nu_{\text{peak}}^{\text{S}} < 10^{14} \text{ Hz}$); intermediate-synchrotron-peaked (ISP, $10^{14} \text{ Hz} < \nu_{\text{peak}}^{\text{S}} < 10^{15} \text{ Hz}$); or high-synchrotron-peaked (HSP, $\nu_{\text{peak}}^{\text{S}} > 10^{15} \text{ Hz}$). Although the two classification schemes do have some degeneracy (e.g., HSP sources are largely BL Lacs, while most FSRQs are LSP sources), it is relevant to discuss them both, as the spectral classification is linked to the physical process (synchrotron radiation) responsible for the low frequency emission.

In our study we will of course be using only sources that have been associated with a low-energy AGN counterpart. However, we note that 1FGL also contains 374 unassociated sources. If some of these sources are AGN that were not associated with a lower-energy counterpart because they happen to be too faint in radio, then this could potentially introduce a bias in our assessment of the radio/gamma flux correlations. In Fig. 1, we show normalized histograms of the gamma-ray fluxes of the high-latitude ($|b| > 10^\circ$) AGNs and of the high-latitude unassociated sources. Although in both distributions the sources tend to cluster in the low flux bins, this effect is much more pronounced in the unassociated gamma-ray sources, and there is strong statistical evidence that the two samples are not drawn from the same population (K-S probability of 4.3×10^{-13}). This makes it unlikely that we significantly overestimate the strength of the correlation because of the existence of yet-unassociated, radio-faint and gamma-ray-bright blazars.

On the other hand, in any given radio flux limited sample there are sources that are radio bright and gamma-ray quiet (see e.g. §2.2.2 below for the case of the OVRO sample). This fact can be the consequence of long-term variability and/or low duty cycle in gamma-rays (Ghirlanda et al. 2011); in any case, in this paper we only deal with the sources detected by LAT.

2.2. Radio data

In Table 1, we list the radio flux densities used for the present work, along with some basic information on the sources (position, optical and spectral type, redshift). In particular, we give the archival 8 GHz interferometric flux density in Col. 8 (with the corresponding reference in Col. 9) and the 15 GHz single dish flux density, when available, in Cols. 10–12. A summary of the details of the relevant observations are given in the following subsections.

2.2.1. CRATES/Other catalogs

For all sources in the 1LAC, we were able to collect interferometric measurements of the historic radio flux density. This provides us with the largest database of radio and gamma-ray measurements ever obtained and we use it for a discussion of the correlation between the two bands.

Most of these data come from CRATES (478 sources) or CRATES-like (96 sources) observations. The CRATES catalog (Healey et al. 2007) contains precise positions, 8.4 GHz flux densities, and radio spectral indices for over 11,000 flat-spectrum sources over the entire $|b| > 10^\circ$ sky. In the region $\delta > -40^\circ$, the 8.4 GHz data were obtained with the VLA in its largest (A) configuration, and the spectral indices were determined by comparing the 8.4 GHz flux density and the 1.4 GHz flux density from the NRAO VLA Sky Survey (NVSS; Condon et al. 1998). In the region $\delta < -40^\circ$, the 8.4 GHz data were obtained with ATCA in a variety of large configurations (6A/C/D, 1.5B/C/D), and the spectral indices were determined by comparing the 8.4 GHz flux density and the 843 MHz flux density from the Sydney University Molonglo Sky Survey (SUMSS; Mauch et al. 2003).¹

The data for sources that are not in CRATES are often of identical or very similar quality to those for CRATES sources. For example, 8.4 GHz data from the Cosmic Lens All-Sky Survey (CLASS; Myers et al. 2003; Browne et al. 2003), from which the CRATES catalog obtained much of its northern hemisphere data in the first place, were all taken with the VLA in the A configuration. Similarly, the PMN-CA catalog² of over 6600 radio sources was compiled from 8.6 GHz data obtained with ATCA in the 6A, 6C, and 6D configurations. As a result, the radio flux densities and spectral indices of most non-CRATES sources can still be compared directly to those of true CRATES sources without introducing any systematic errors or biases.

For 19 sources, for which 8.4 GHz VLA or ATCA measurements are not available, we extrapolate from lower frequency interferometric measurements (e.g. those reported from the Roma-BZCAT, Massaro et al. 2009). The spectral indices used for the extrapolation are those available

¹Strictly speaking, the ATCA observations were performed at 8.6 GHz, and the flux densities were converted to 8.4 GHz by interpolation using the spectral index, but even for a very inverted source ($\alpha = -1$), this represents an adjustment of <3% to the flux density.

²Survey results can be downloaded from <http://www.parkes.atnf.csiro.au/observing/databases/pmn/casouth.pdf>

from NED; when none was available, it was conventionally set to $\alpha = 0.0$.

Finally, there are 6 sources in the 1LAC that possess a significant amount of extended radio emission (such as the misaligned AGNs discussed by Abdo et al. 2010b) and escape the selection criteria of CRATES and similar surveys. However, these are all rather well known radio sources, and it has been straightforward to obtain interferometric measurements of their radio core flux density from the literature, either directly or with trivial calculations (e.g. interpolation).

2.2.2. OVRO

Since late 2007, the Owens Valley Radio Observatory (OVRO) 40 m Telescope has been engaged in a blazar monitoring program to support the *Fermi*-LAT (Richards et al. 2010). In this program, all 1158 CGRaBS blazars north of declination -20° have been observed approximately twice per week or more frequently since June 2007 (Healey et al. 2008). Gamma-ray blazars and other sources detected by *Fermi* have been added to the program which makes the total number of monitored sources close to 1500. Of these sources, 199 appear as “clean” associations in the 1LAC catalog.

The OVRO flux densities are measured in a single 3 GHz wide band centered on 15 GHz. Observations were performed using azimuth double switching as described in Readhead et al. (1989), which removes much atmospheric and ground interference. The relative uncertainties in flux density result from a 5 mJy typical thermal uncertainty in quadrature with a 1.6% systematic uncertainty. The absolute flux density scale is calibrated to about 5% via observations of the steady calibrator 3C 286, using the Baars et al. model (Baars et al. 1977). A complete description of the OVRO program, population studies of the radio variability, their relation with other physical properties and a study of the time relation between radio and gamma-ray emission are presented in a series of dedicated publications (Richards et al. 2010; Pavlidou et al. 2011; Max-Moerbeck et al. 2011).

Because the *Fermi*-LAT flux densities used in this study represent time averages over the observation period, we produce estimates of the 15 GHz time average flux density from the OVRO data for each source by linearly interpolating between successive light curve values, integrating between the start and end dates, then dividing by the time interval. For the 11 month data here, the start date was midnight August 4, 2008 (MJD 54682), and the end date was midnight July 4, 2009 (MJD 55016). Hereafter, we will be referring to average 15 GHz radio fluxes obtained in this manner as the OVRO *concurrent* data.

The normalized distribution of average fluxes of the OVRO subset is shown in Fig. 2, overplotted with the distribution of average fluxes, obtained in the same manner, of gamma-ray quiet CGRaBS sources north of declination -20° . The sources which are also in 1LAC have generally higher 15 GHz average fluxes. However, there is substantial overlap between the two distributions, so the existence of sources with large fluxes at 15 GHz but which are faint in gamma rays is not unexpected. Therefore, our expectation from the distribution of fluxes alone is that if a statistically

significant correlation between radio and gamma-ray fluxes indeed exists, it will likely have a substantial scatter.

3. Results

In this section we present the results of our search for possible correlations between radio flux densities and the gamma-ray photon flux for the sources in the 1LAC sample. In particular, in Sect. 3.1 we consider the full 1LAC sample and search for correlations with archival radio data, while in Sect. 3.2 we focus on the subset of sources observed at OVRO, considering both concurrent and archival radio data; finally, in Sect. 3.3 we present results for a subset of the 1LAC composed of sources detected in at least 4 individual energy bands. There are 599 sources in the 1LAC clean sample and 199 in the 1LAC-OVRO sample. The OVRO 15 GHz concurrent fluxes are averaged (time-integrated, as in the gamma-ray data) over the same interval as the LAT observations, and for all of sources considered here there exists *gamma-ray* variability on timescales shorter than the averaging period.

For each sample, we have compared the radio flux density to the 1-yr gamma-ray energy flux at $E > 100$ MeV. Moreover, since we have unprecedentedly large datasets, we can also explore whether the strengths of any observed correlations are dependent on the gamma-ray energy band in which the flux is calculated, or on the source spectral type. For this reason, we also compare radio flux densities to gamma-ray photon fluxes calculated in the single energy bands $100 \text{ MeV} < E < 300 \text{ MeV}$, $300 \text{ MeV} < E < 1 \text{ GeV}$, $1 \text{ GeV} < E < 3 \text{ GeV}$, $3 \text{ GeV} < E < 10 \text{ GeV}$, $10 \text{ GeV} < E < 100 \text{ GeV}$. In each energy band, we consider only the sources that are significant in that band. Not every source is detected in all energy bands; actually, only a small minority is, i.e. 51/599 (8.5%). As a consequence of their different spectral properties, FSRQs are generally more abundant in the lowest energy bands, while BL Lacs are more numerous in the most energetic ones. For instance, for the 1LAC sources, we have 128 FSRQs and 47 BL Lacs in the 100–300 MeV band, and 22 FSRQs and 99 BL Lacs in the 10–100 GeV band.

Since FSRQs and BL Lacs have different spectral properties and showed different behaviors in the preliminary analysis (Abdo et al. 2009; Giroletti et al. 2010), we also tested the two populations separately, in addition to the full set of sources. Moreover, a classification based on the broadband spectral properties is physically more meaningful, so we also consider the populations of low-, intermediate-, and high-synchrotron-peaked blazars (LSP, ISP, and HSP respectively).

In total, we have 36 combinations of source type and gamma-ray energy band for the 1LAC. For the OVRO sample, we have also the possibility to consider the radio data obtained at 15 GHz during the same interval of the gamma-ray observations, both as mean and peak flux density measurements, and in a different time domain. For each combination, we produced a scatter plot of the radio vs. gamma-ray flux densities and determined the Spearman’s rank correlation ρ , which are presented in the following subsections.

The value of ρ is characteristic of the strength of the correlation, and it can be related to the significance of an *apparent* correlation between radio and gamma-ray fluxes. However, an assessment of the statistical significance of an *intrinsic* correlation in each case (after the effects of a common distance and a limited dynamical range are accounted for) is nontrivial and cannot be based on a conventional assumption of unbiased samples. Therefore, we use simulations based on the method of surrogated data to evaluate the significance of intrinsic correlations and discuss them in Sect. 4.

3.1. Full sample

The sources associated to the 1LAC members span over 4 orders of magnitude in radio flux density, ranging between a few mJy for the faintest BL Lacs to several 10's of Jy for the brightest quasars (e.g. 3C 273 and 3C 279). The flux density distributions for the whole population and divided by source type are shown in Abdo et al. (2010d). The overall distribution shows a broad peak at $S \sim 800$ mJy, which is the result of the combination of the two peaks of the single population distributions, with BL Lacs peaking around $S \sim 400$ mJy and FSRQs at $S \sim 1300$ mJy. In gamma-rays, the energy fluxes span over 3 orders of magnitude (between 4.8×10^{-12} and 6.6×10^{-10} erg cm $^{-2}$ s $^{-1}$ at $E > 100$ MeV), with BL Lacs typically fainter than FSRQs; the mean photon fluxes at $E > 100$ MeV are 8.5×10^{-8} ph cm $^{-2}$ s $^{-1}$ and 2.9×10^{-8} ph cm $^{-2}$ s $^{-1}$ for FSRQs and BL Lacs respectively (Abdo et al. 2010d).

We show the gamma-ray and radio flux scatter plots for the 1LAC sources in Fig. 3, 4, and 5. Each figure shows a collection of panels showing various combinations of the 1FGL gamma-ray flux and radio historical flux density. In particular, Fig. 3 shows the gamma-ray energy flux vs. radio flux density for all sources (top left panel), sources divided by optical type (FSRQ and BL Lacs in the centre and right top panels, respectively), and sources divided by spectral type (bottom row, with LSP, ISP, and HSP in the left, middle, and right panels, respectively); in Fig. 4 and Fig. 5, we show the gamma-ray photon flux vs. radio flux in the five individual LAT energy bands (left to right), divided by source type: in Fig. 4, the top row shows all sources, the middle one shows FSRQs, and the bottom one BL Lacs; in Fig. 5, top, middle, and bottom rows are for the three different synchrotron peak classes: LSP, ISP, and HSP blazars, respectively. Symbols in magenta show sources for which a redshift is not available.

We report the correlation coefficients between radio and gamma-ray flux for the full sample in Table 2, divided by source type and energy band, and we visualize them in Fig. 6. In this figure, the correlation coefficients are shown across the five energy bands and are connected with lines of different color and style for the various sub-populations: solid black line for the full 1LAC sample, dashed lines for optical type sub-groups (red for FSRQ and blue for BL Lacs), dotted lines for sub-groups defined by the spectral properties (magenta for LSP, green for ISP, cyan for HSP). The accuracy to which the correlation coefficients are determined, based on the number of sources and the strength of the correlation, is shown by the error bars, which correspond to the standard

deviation for ρ , defined as $\sigma_\rho = (1 - \rho^2)/\sqrt{N-1}$; although this standard deviation is formally defined only for the Pearson product-moment correlation coefficient r (Wall & Jenkins 2003), we extend it to our case, since the distribution of the Spearman ρ for $N > 30$ approaches that of the Pearson product-moment.

The Spearman correlation coefficient for all (599) sources is $\rho = 0.43$. FSRQs and BL Lacs reveal different behaviors. In general, BL Lacs exhibit larger values of ρ than FSRQs, both when the broad band gamma-ray energy flux is considered and in most of the single energy bands; for example, in the most populated energy band (for both populations, the 1–3 GeV band, with 220 FSRQ and 214 BL Lacs), we find $\rho = 0.54$ for BL Lacs and $\rho = 0.35$ for FSRQs, although the difference is less significant in the other energy bands. Moreover, in FSRQs the correlation coefficient is quite stable across the various energy ranges (between $\rho = 0.29$ and $\rho = 0.42$), while BL Lacs display some evolution, with ρ decreasing as fluxes at higher energy bands are considered. If one looks at the spectral type populations, HSPs are always the ones showing a tighter apparent correlation (except for the scarcely populated 100–300 MeV band), and as high as $\rho = 0.64$ in the 1–3 GeV band.

3.2. OVRO sample

The sources with OVRO data represent a 199 element subset of the 1LAC sample, going down to radio fluxes as low as 172 mJy (archival 8 GHz value for J1330+5202, the source associated to 1FGL J1331.0+5202) and 64.7 mJy (1-yr concurrent 15 GHz value for J1725+1152). FSRQs outnumber BL Lacs by 120/69. This sample provides the largest dataset of concurrent radio measurements to the 1LAC fluxes and is therefore highly valuable in order to understand the implications of variability on the radio/gamma-ray correlation.

In particular, we are in the position of comparing the correlation coefficient not only among different source types and energy bands, but also to assess the differences that arise when we use concurrent data or not. In Table 3, we give the correlation coefficients: for the radio/gamma-ray flux densities using historical radio flux densities at 8 GHz; the mean and peak flux density value at 15 GHz calculated over the first 11 months of activity of the LAT; and an average 15 GHz flux calculated over a one-week interval *after* the first 11 months of activity of the LAT (specifically, the period between January 23 – 31 2010).

Figures 7, 8 and 9 show the scatter plots of the concurrent radio and gamma-ray fluxes, using mean values for the radio flux density. As for the 1LAC case, we show 3 collections of scatter plots: radio vs. gamma-ray energy flux for all sources, FSRQ, BL Lacs, LSP, ISP, and HSP sources in Fig. 7, radio vs. gamma-ray photon flux for all sources, FSRQ, and BL Lacs in Fig. 8, and for LSP, ISP, and HSP sources in Fig. 9. Finally, the trend of ρ as a function of energy band for the various sub-classes is shown in Fig. 10, with the same notation as in Fig. 6.

Unlike for the larger 1LAC sample, in the sample with concurrently-measured radio fluxes

FSRQs generally display larger values of ρ than BL Lacs; as an example, in the 1–3 GeV energy band, $\rho_{\text{FSRQ}} = 0.48$ and $\rho_{\text{BLL}} = 0.13$. Moreover, the correlation coefficient for BL Lacs for the energy bands above 1 GeV is consistent with no correlation, becoming even marginally negative in the 10–100 GeV band. It has to be remembered that the OVRO sample is somewhat biased in favor of bright radio sources, so it contains relatively few BL Lacs, and in particular just a handful (10/199) of HSPs, as they are generally rather radio weak. Interestingly, the BL Lac curve falls below the three individual spectral type curves (LSP, ISP, HSP). We note that the sample also contains 41 sources (about 20% of the total) whose spectral type is unknown and that have almost uncorrelated radio and gamma-ray flux density. While this explains part of the difference between BL Lacs and LSP+ISP+HSP, it is also important to warn that the 33 LSP BL Lacs do show systematically lower values of ρ than the whole group of LSP sources (which is dominated by FSRQs).

As far as the radio variability is concerned, we find that for the whole sample the correlation coefficient with concurrent 15 GHz data is always larger than that obtained using archival 8 GHz data or non-concurrent 15 GHz OVRO data. This result is mostly driven by the FSRQ population, while the less numerous BL Lac population does not seem to reveal significant differences between the use of concurrent or non-concurrent radio data. Finally, the use of the peak 15 GHz flux density yields generally weaker correlations, in some cases even weaker than those found using non-concurrent data.

3.3. Sources significant in at least four energy bands

For both the 1LAC and the OVRO samples, we have considered in each energy range all the sources that were significant in that band. As a consequence of the different spectral characteristics of each individual source, the samples used to calculate the various coefficients have often little overlap between each other (even within the same population), particularly in energy bands that are far apart.

For this reason, we have also considered a third case, the sample of sources that are significant in at least four of the five individual energy bands. In this way, we build a relatively bright, well defined, and sizable sample. This sample is composed of 192 sources, and both FSRQ (94 sources) and BL Lacs (84) are well represented.

As in the full 1LAC sample, BL Lacs have generally higher values of ρ than FSRQ (e.g., $\rho_{\text{BLL}} = 0.54$ and $\rho_{\text{FSRQ}} = 0.29$ for the radio vs. energy flux at $E > 100$ MeV correlation). The individual values are reported in Table 4 and Figs. 11, 12, 13, and 14, using the same notation as in the full 1LAC and OVRO cases.

If we look at the three groups defined by the synchrotron spectral properties, we find that the maximum of the correlation coefficient is obtained in the lowest energy band for LSP ($\rho = 0.41$ between 100 and 300 MeV), in the 300 MeV–1 GeV for ISP ($\rho = 0.63$), and in the 1–3 GeV for HSP

397 ($\rho = 0.74$). Therefore – albeit with some overlap between the error bars – the higher the spectral
 398 frequency of the synchrotron spectral peak, the higher the energy at which the strongest apparent
 399 correlation is observed, and the higher the correlation coefficient itself.

400 4. Significance tests with the method of surrogate data

401 In order to quantitatively assess the significance of any apparent correlation between concur-
 402 rent radio and gamma-ray flux densities of blazars in the presence of distance effects, we have used a
 403 test based on the method of surrogate data. In studying possible intrinsic correlations between flux
 404 densities in different bands the null hypothesis is that they are *intrinsically* uncorrelated (implicitly
 405 assuming that any apparent correlation is due to the observational errors and/or biases). In a fre-
 406 quentist approach, we investigate how frequently a sample of objects with intrinsically uncorrelated
 407 gamma/radio flux densities, similar to the sample at hand, will yield an apparent correlation as
 408 strong as the one seen in the data, when subjected to the same distance effects as our actual sample
 409 (see Pavlidou et al. 2011, for a more detailed description of the test).

410 In our test the strength of the apparent correlation is quantified by the Pearson product-
 411 moment correlation coefficient r , defined as

$$r = \frac{\sum_{i=1}^N (X_i - \bar{X})(Y_i - \bar{Y})}{\sqrt{\sum_{i=1}^N (X_i - \bar{X})^2 \sum_{i=1}^N (Y_i - \bar{Y})^2}} \quad (1)$$

412 Since it is not always straightforward to construct simulated samples with the exact same
 413 selection criteria as the data sample, we have used *permutations* of measured quantities. To simulate
 414 the effect of a common distance on intrinsically uncorrelated luminosities, we permute in luminosity
 415 space:

- 416 • We split our sample in N redshift bins, with N determined so that each bin has at least ~ 10
 417 sources. The separation in bins ensures that the luminosity and redshift distributions of the
 418 simulated samples approximate those in the real data, thus avoiding the introduction of biases
 419 not present in the data. Note however that, as we have shown in detail in Pavlidou et al.
 420 (2011), the significance of the correlation we find increases with increasing N (the correlation
 421 becomes more significant), until it saturates for large enough N , provided that the number of
 422 sources is large enough.
- 423 • In each redshift bin: from the measured radio and gamma-ray flux densities, we calculate
 424 radio and gamma-ray luminosities at a common rest-frame radio frequency and rest-frame
 425 gamma-ray energy.³

³In order to implement the K-correction (project our calculated luminosities to a common rest-frame frequency in

- We permute the evaluated luminosities, to simulate objects with *intrinsically uncorrelated* radio/gamma luminosities.
- We assign a common redshift (one of the redshifts of the objects in the bin, randomly selected) to each luminosity pair, and return to flux-density space. Returning to flux-density space allows us to avoid Malmquist bias; assigning a common redshift allows us to simulate the common-distance effect on uncorrelated luminosities. In addition, by permuting in luminosity space we are guaranteed that the simulated samples have the same luminosity dynamical range as our actual sample.
- To avoid apparent correlations induced by a single very bright or very faint object *much brighter or fainter than the objects in our actual sample*, we reject any flux-density pairs where one of the flux densities is outside the flux-density dynamical range in our original sample. The rejection rate is however very low for $N \geq 3$, and it decreases with increasing N .

Using a number of flux density pairs equal to the number of objects in our actual sample, we calculate a value for r . We repeat the process a large number of times, and calculate a distribution of r -values for intrinsically uncorrelated flux densities. The fraction of the area under this distribution for $|r| \geq r_{\text{data}}$, where r_{data} is the r -value for the observed flux densities, is the probability to have obtained an apparent correlation at least as strong as the one seen in the data from a sample with intrinsically uncorrelated gamma-ray/radio emission. This quantifies the statistical significance of the observed correlation.

Our results for all the correlations discussed in the present paper are shown in Tables 5 (full 1LAC sample), 6 (OVRO sample, using concurrent radio data), 7 (OVRO sample, using non-concurrent radio data), and 8 (sample of sources detected in at least 4 bands); for every case examined, we give the number of sources in the studied subset, the number of redshift bins used in the analysis, the Spearman correlation coefficient ρ , the value of the Pearson correlation coefficient r of the dataset, and the statistical significance of the apparent correlation, which we define as the fraction of simulated datasets with the same number of points, same common-distance, luminosity-range, and flux-range effects as the actual dataset *but no intrinsic correlation* which had an absolute value of r at least as big as the actual dataset. The number of points in each dataset studied generally differs from the number of points in the corresponding dataset of §3.1, 3.2 and 3.3, because for the surrogate data studies we only use sources for which the redshifts are known. In the scatter plots of Figs. 3–5, 7–9, and 11–13, these sources are plotted with black points (while magenta is used for sources with unknown z). For the same reason, the Spearman correlation

each band) we are using the historical radio spectral index α and the 1FGL photon index; The spectral index has been shown, at least at radio frequencies, to vary with flux (Fuhrmann et al. 2011); however, as shown in Pavlidou et al. (2011), different choices in radio spectral indices do not have a large effect on the resulting correlation significance, as the sources of interest generally have flat radio spectra and the relevant K-correction is small.

coefficient for the sets submitted to the surrogate data analysis is also different but consistent with the value shown in Tables 2-4.

In the case of large samples and relatively high correlation coefficients, the apparent correlations between radio and gamma-ray flux are found to be also *intrinsically* very significant: for example, the probability of the correlation between $E > 100$ MeV gamma-ray flux and the 8 GHz archival data arising due to common-distance effects or the limited flux and luminosity ranges examined is smaller than 10^{-7} . However, for smaller subsets and weaker correlations (lower values of the correlation coefficients) the significance of the correlation cannot be established with such high confidence or not at all. A striking example is that of the correlation between 8 GHz archival flux densities and 10-100 GeV fluxes for sources that were detected at least in four bands: the simulated datasets are more strongly correlated than the actual dataset more than 30% of the time.

In Fig. 15 we show, for three example cases, the distribution of the absolute value of the Pearson product-moment r for simulated datasets. The value of r for the actual dataset in each case is indicated with an arrow. The three cases are selected so that they represent examples of low (top panel), medium (middle panel) and high (bottom panel) correlation significances. In some cases (as in the middle panel of these examples) the distribution of r for simulated, intrinsically uncorrelated datasets peaks at a finite positive value *even in flux space*. This generally indicates a clustering of intrinsic luminosities around a specific value; these luminosities then are more frequently selected, even by chance, and when a common redshift is applied to them they result in a positive correlation coefficient, which then becomes more common than the zero value (for a more detailed discussion of this effect, see also Pavlidou et al. 2011).

The interpretation of the quoted significances requires some care, owing to the large number of subsamples (a total of 144) examined using the data shuffling technique. The quoted significances are a useful tool in comparing the significance of any apparent correlation between different subsamples, however the correlation significance in any single subsample is severely mitigated because of the issue of trials. E.g., any effect that occurs 5% of the time by chance would have a probability of 99.9% to occur at least once in 144 independent trials; this probability becomes 76.3% for effects occurring by chance 1% of the time, and 1% for effects occurring by chance only 10^{-4} of the time. Although the subsamples considered are, in fact, not independent, the numbers above may serve as illustration that interpreting the here quoted significances at "face-value" can be misleading. However, for the largest samples considered here, we have found correlations with very high significance ($< 10^{-7}$), which remain very confident even in the face of the large number of trials.

We further remind that the method of surrogate data discussed above is applicable only to samples for which the redshifts of the sources are known. For this reason, when calculating significances for the apparent correlations of various subsamples, we discard sources for which the redshift is not known (most of such sources are BL Lacs). However, the omission of sources without known redshifts can affect the evaluated significance in two ways: by altering the redshift distribution of the sample, and by reducing the number of sources. As a quantitative example of these effects,

we have tested how our calculated significances change if we include the sources without known redshifts, and we assign redshifts to them in the following two ways: (a) assume that the missing redshifts have the same distribution as the known redshifts; in this case, we randomly select a redshift from sources of the same type (in most cases, BL Lacs) for the sources without redshifts; (b) assume that the missing redshifts have systematically higher values than the known redshifts; in particular, we assume that the distribution of the missing redshifts is that of known redshifts (for sources of the same type) translated to higher redshifts by $\Delta z = 0.5$. We have tested these two cases for the sample of HSP blazars using 8 GHz radio flux densities and gamma-ray flux in the 10-100 GeV band.

The results for these test cases are shown in Fig. 16. As an effect of the increased number of sources available for the test (47 instead of 21), the significance increases from 2.0×10^{-2} to 4.2×10^{-5} (if the sources without redshift follow the distribution generated with $\Delta z = 0.5$), or even to 3.0×10^{-8} (if they are distributed in the same way as the sources with a measured redshift). Note however that the results are substantially different depending on our choice of how to assign simulated redshifts, and for this reason we have not implemented this technique more extensively in our samples.

5. Discussion

The sources in the 1LAC sample have an overall positive correlation between radio flux density and gamma-ray photon flux, with a very high statistical significance as supported by the dedicated statistical analysis presented in Sect. 4. Moreover, the vast majority of the statistical tests run on the distribution of the gamma-ray and radio flux densities for the various source type/energy range combinations has also revealed some correlation (Sect. 3), with moderate-to-high statistical significance. Overall, this confirms the existence of a relationship between the emission in these two distant parts of the electromagnetic spectrum. This finding is consistent with other studies on the subject (Kovalev et al. 2009; Ghirlanda et al. 2010; Mahony et al. 2010). Most importantly, it has now been demonstrated to be robust against common-distance effects, and the effect of a limited flux and luminosity range.

In addition, the sensitivity of the LAT over three decades in energy range allows us to characterize a huge number of extragalactic gamma-ray sources across the gamma-ray band and to clarify some details of the relationship. The quality of the radio data provided by the archives as well as from concurrent monitoring are also crucial for a better understanding of the general picture.

For instance, BL Lacs are under represented in analyses performed starting from samples with moderate or high radio flux density limits, such as the AT20GHZ (Ghirlanda et al. 2010; Mahony et al. 2010) and the MOJAVE (Kovalev et al. 2009), whereas they actually constitute more than half of the 1LAC. Thanks to the archival interferometric data obtained for the full sample, we have studied the radio/gamma-ray connection within the two blazar sub-populations

separately with a large number of sources. Indeed, even when considered independently, 1LAC BL Lacs display a correlation between their radio and gamma-ray flux densities that is highly significant; the chance probability is, e.g., $< 10^{-7}$ when considering the full energy band, and 1.9×10^{-6} in the 1–3 GeV energy band (see Table 5). As the surrogate data method can only be applied to sources with a known distance, it would be desirable to have more redshifts available for BL Lacs in order to improve the significance of this correlation also for other sub-bands. However, even with the lack of more redshift measurements, the conclusions implied from Fig. 16 make one expect that such significance is no less than that of FSRQs, or even higher given the larger value of both Spearman’s ρ and Pearson r for BL Lacs.

The finding of a high apparent correlation strength for BL Lacs is not only present in the full 1LAC, but is also present – and actually with higher values of ρ – when one considers the results obtained for the sample of sources detected in at least four bands (§3.3). This sub-sample probably provides the most robust results, for two reasons. First, the ρ values are obtained by considering largely overlapping samples in each energy bin; second, since these are moderately bright gamma-ray sources (they would not be significant in 4/5 energy bands otherwise), the fluxes are better constrained and we are not too close to the detection limit. Still, we caution that the 4-band sample may not be a fully representative sample of the whole gamma-ray sky, as it is about 1/3 of the 1LAC.

As far as the OVRO sample is concerned, it seems to have yielded somewhat different details of the overall picture with respect to the full 1LAC. This is not entirely surprising, as the two samples represent different populations: the OVRO sample is generally brighter compared to the whole 1LAC set, and FSRQs are more strongly represented. In any case, the availability of the large, long-term, high-cadence monitored OVRO sample is of great importance in the assessment of the role of variability on the radio-gamma connection. The OVRO data clearly reveal, for the first time, that concurrent radio fluxes are more strongly correlated with gamma-ray fluxes than archival data, even at the same frequency. For example, the significance of the correlation between radio and gamma-ray broad band fluxes for all sources increases from 1.9×10^{-6} to 9.0×10^{-8} when going from non-simultaneous to concurrent data. Increased significance is found also for most of the various combinations of source type and energy band. This was a long-expected result, which has finally been demonstrated. Interestingly, the peak radio flux density during the time of collection of gamma-ray data shows a weaker correlation than the one obtained using the mean values; it is actually even weaker than that of non-concurrent radio data. The fact that the strongest correlation is obtained for the time-integral of the flux density in the two bands shows that the best correlation is between the overall energy dissipated in the two regimes.

A further advantage of such a large dataset, which distinguishes our results from past work, is that it provides sufficient number of sources for good statistical analysis, even when we divide the sample in finer sub-groups, for example on the basis of the spectral properties in the synchrotron component of the SED. The possibility of sub-grouping is interesting, particularly when we compare the results obtained dividing by optical type and position of the peak of the low-energy component

and/or considering each of the individual LAT energy bands. However, even if we are for the first time in the position of attempting such studies, we have to keep in mind that the statistical significance becomes inevitably lower when the samples are less populated, so the following discussion is certainly somewhat speculative.

First, the BL Lacs seem to follow a pattern of lower correlation coefficients when gamma-rays of increasing energy are considered – with flux densities that become apparently uncorrelated (or even anti-correlated) in the highest energy band; this is particularly prominent in the OVRO sample. However, when the spectral types are considered separately, a pattern emerges with HSP always being the class with the strongest correlation in the 1–3, 3–10, and 10–100 GeV energy bands. ISP BL Lacs, on the other hand, show much weaker or absent correlation at high energy, which affects the total population of BL Lacs when considered as a whole. This effect becomes most prominent when the ISP/HSP population ratio is higher.

Second, LSP blazars are more difficult to characterize, since they are a mixed population of both BL Lacs and FSRQs. We note that FSRQ and LSP however do not always follow the same trend. It is thus likely that the radio and gamma-ray emission in FSRQ-LSP and the BL Lac-LSP are not produced by the same kind of process. This may or may not be related to the other well known differences in the optical spectrum and in the accretion regime for these two populations.

The interpretation of the dependence of the correlation strength on the source type is therefore in general not straightforward. The fact that HSP sources show the strongest correlation could be related to the fact that these sources do not generally possess large amounts of extended emission, and even on parsec scales their jets are rather weak. So the interferometric flux density is probably more representative of the properties of the region where the gamma-rays are produced. Moreover, in HSP sources the high energy component of the SED extends to the TeV band, so that the particles involved in the radio and GeV emission could be low energy electrons, unlike the LSP case where the GeV emission requires high energy particles.

The physical reason why even within a single population the correlation coefficient is quite strongly dependant on the considered energy band is even more difficult to interpret. For example, ISP blazars have a peak of correlation in the low energy band, while their radio and gamma-ray flux densities become essentially uncorrelated at the highest energies: sources of any radio flux density seem to produce more or less the same amount of gamma-ray photons. In other words, the radio-bright ISP blazars would have much softer gamma-ray spectra than the radio weak, which would be somewhat consistent with the picture in the blazar sequence Fossati et al. (1998); however, the same trend is not observed in other blazar classes.

Finally, one should be cautioned against correlations that are driven from a minority of very high (or very low) data points. For instance, Linford et al. (2011) find a flux-flux correlation for 50 gamma-ray FSRQs in the VLBA Imaging and Polarimetry Survey (VIPS, Helmboldt et al. 2007), but they also discover that the correlation disappears when the 10% brightest sources in the radio are discarded. In our 247 FSRQs sample, the effect is not quite as dramatic, with only a modest

decrease of the correlation coefficient. As BL Lacs are entirely unaffected, however, this could still be an interesting clue about additional differences between the two classes.

5.1. Luminosity Distributions

Throughout this paper, we discuss the strength and the significance of radio/gamma correlations in terms of the flux density in each band. We do not discuss luminosity correlations, as the limited dynamical range in fluxes, combined with the aggregation of sources close to the flux limit and the square-distance effect always induce a strong apparent correlation in luminosity space, whereas plots in the flux density plane give a better visual impression of the scatter involved. Moreover, it is possible to show analytically that the information in the flux/flux and luminosity/luminosity correlations is essentially degenerate.

However, from the physical point of view it is interesting to examine also the ranges and distributions of luminosities in the gamma-ray band and in the radio band, which are shown in Abdo et al. (2010d). The luminosity ranges probed by our sample extend over approximately two orders of magnitude in each band for BL Lacs and FSRQs, while they are more extended for other AGN. Although there is significant overlap between the luminosities of different source types, FSRQs are generally more luminous than BL Lacs, which are in turn more luminous than the remaining AGNs (which includes radio galaxies and blazars of uncertain type); this result holds both for the radio and the gamma-ray bands. Therefore, we suggest that there is a lot of discovery space for sources of low gamma-ray luminosities, as the luminosity range of unclassified AGN and radio galaxies extends more than two orders of magnitude fainter than BL Lacs and FSRQ in the gamma-ray band, but it is so far much less populated than the higher luminosity domain. It is possible that some of the fainter unassociated gamma-ray sources at high latitudes are AGN in this luminosity range.

6. Conclusions

We have searched for a possible intrinsic correlation between gamma-ray and radio fluxes. We have found that such a correlation does exist, and it is statistically significant for the largest sample we have studied that includes all source types: the probability that it arises by chance (e.g., through common-distance effects, accentuated by the limited dynamical range of fluxes of the sample) is smaller than 10^{-7} . The significance is also very high when FSRQ and BL Lacs are considered independently. However, the distribution of sources along the correlation has appreciable scatter (which can be typically an order of magnitude). Therefore, we strongly caution that any use of this intrinsic connection between radio and gamma-ray emission in statistical descriptions of the gamma-ray population, such as to obtain gamma-ray luminosity functions from radio luminosity functions, should be done with care and always accounting for the scatter involved. When comparing archival

with concurrent data we find that the moderate significance of a correlation derived from the archival radio – gamma-ray sample increases appreciably when concurrent data are used.

The statistical significance of a correlation does not have a simple dependence on the *apparent correlation strength*. Various other factors play a role in an assessment of the significance of an apparent correlation, besides the tightness of the observed correlation itself. These include the following: (1) errors in the observed fluxes, (2) any biases, e.g., the presence of common-distance effects and flux limits, and (3) the number of sources in the sample. While underlying statistical errors (1) are inherent, in the present work we have explicitly accounted for biases (2). The sample size (3) affects the importance of “cosmic variance”: a small sample with a significant correlation but appreciable statistical errors or scatter might happen to appear uncorrelated, and, conversely, any single incarnation of a small, uncorrelated sample might appear correlated by chance. Considering all of these factors, we have established high significance for some correlations but the same is not possible for very small subsamples.

We have studied the radio/gamma correlation for different subsets of blazars, and we have found that the *apparent strength* of the correlation depends on the type of blazar; in particular, BL Lacs have been shown to possess a high apparent correlation strength using the largest sample ever considered. The *apparent strength* of the correlation depends also on the epoch of observation, in that concurrent radio and gamma-ray measurements correlate better than data obtained at different epochs in the two bands.

Finally, the specific gamma-ray energy band over which the gamma-ray flux is calculated seems also to affect the strength of the correlation, with HSP blazars generally displaying a stronger correlation. The highest apparent correlation strength appears at higher gamma-ray energy for HSPs than for LSPs and ISPs. Both the specific energy bands and source types considered impact also the significance of the correlation. These results have been obtained thanks to the large number of AGNs detected by the *Fermi*-LAT, although in some of the considered correlations the number of sources is small. Therefore, a further increase in the number of objects in each sub-group, as that expected for the 2LAC, is needed to improve the significance of individual results.

The *Fermi* LAT Collaboration acknowledges generous ongoing support from a number of agencies and institutes that have supported both the development and the operation of the LAT as well as scientific data analysis. These include the National Aeronautics and Space Administration and the Department of Energy in the United States, the Commissariat à l’Energie Atomique and the Centre National de la Recherche Scientifique / Institut National de Physique Nucléaire et de Physique des Particules in France, the Agenzia Spaziale Italiana and the Istituto Nazionale di Fisica Nucleare in Italy, the Ministry of Education, Culture, Sports, Science and Technology (MEXT), High Energy Accelerator Research Organization (KEK) and Japan Aerospace Exploration Agency (JAXA) in Japan, and the K. A. Wallenberg Foundation, the Swedish Research Council and the Swedish National Space Board in Sweden.

Additional support for science analysis during the operations phase is gratefully acknowledged from the Istituto Nazionale di Astrofisica in Italy and the Centre National d’Études Spatiales in France.

Facilities: *Fermi* LAT, OVRO:40m (), VLA, ATCA

REFERENCES

- Abdo, A. A., et al. 2009, *ApJ*, 700, 597 (LBAS)
- . 2010a, *ApJS*, 188, 405 (1FGL)
- . 2010b, *ApJ*, 720, 912
- . 2010c, *ApJ*, 722, 520
- . 2010d, *ApJ*, 715, 429 (1LAC)
- . 2010e, *ApJ*, 716, 30
- Aharonian, F., et al. 2007, *ApJ*, 664, L71
- Akujor, C. E., & Garrington, S. T. 1995, *A&AS*, 112, 235
- Baars, J. W. M., Genzel, R., Pauliny-Toth, I. I. K., & Witzel, A. 1977, *A&A*, 61, 99
- Browne, I. W. A., et al. 2003, *MNRAS*, 341, 13
- Condon, J. J., Cotton, W. D., Greisen, E. W., Yin, Q. F., Perley, R. A., Taylor, G. B., & Broderick, J. J. 1998, *AJ*, 115, 1693
- Danforth, C. W., Keeney, B. A., Stocke, J. T., Shull, J. M., & Yao, Y. 2010, *ApJ*, 720, 976
- Dondi, L., & Ghisellini, G. 1995, *MNRAS*, 273, 583
- Elvis, M., Maccacaro, T., Wilson, A. S., Ward, M. J., Penston, M. V., Fosbury, R. A. E., & Perola, G. C. 1978, *MNRAS*, 183, 129
- Feigelson, E. D., & Berg, C. J. 1983, *ApJ*, 269, 400
- Fossati, G., Maraschi, L., Celotti, A., Comastri, A., & Ghisellini, G. 1998, *MNRAS*, 299, 433
- Fuhrmann, L., et al. 2011, *ApJ*, in preparation (Bonn F-Gamma paper)
- Ghirlanda, G., Ghisellini, G., Tavecchio, F., & Foschini, L. 2010, *MNRAS*, 407, 791
- Ghirlanda, G., Ghisellini, G., Tavecchio, F., Foschini, L., & Bonnoli, G. 2011, *MNRAS*, 413, 852

- 706 Giroletti, M., Reimer, A., Fuhrmann, L., Pavlidou, V., & Richards, J. L. 2010, ArXiv e-prints,
707 arXiv:1001.5123
- 708 Healey, S. E., Romani, R. W., Taylor, G. B., Sadler, E. M., Ricci, R., Murphy, T., Ulvestad, J. S.,
709 & Winn, J. N. 2007, ApJS, 171, 61
- 710 Healey, S. E., et al. 2008, ApJS, 175, 97
- 711 Helmboldt, J. F., et al. 2007, ApJ, 658, 203
- 712 Isobe, T. 1989, PhD thesis, Pennsylvania State Univ., University Park.
- 713 Komatsu, E., et al. 2009, ApJS, 180, 330
- 714 Kovalev, Y. Y., et al. 2009, ApJ, 696, L17
- 715 Laurent-Muehleisen, S. A., Kollgaard, R. I., Ryan, P. J., Feigelson, E. D., Brinkmann, W., &
716 Siebert, J. 1997, A&AS, 122, 235
- 717 Linford, J. D., et al. 2011, ApJ, 726, 16
- 718 Mahony, E. K., Sadler, E. M., Murphy, T., Ekers, R. D., Edwards, P. G., & Massardi, M. 2010,
719 ApJ, 718, 587
- 720 Marchã, M. J. M., Browne, I. W. A., Impey, C. D., & Smith, P. S. 1996, MNRAS, 281, 425
- 721 Massaro, E., Giommi, P., Leto, C., Marchegiani, P., Maselli, A., Perri, M., Piranomonte, S., &
722 Sclavi, S. 2009, A&A, 495, 691
- 723 Mauch, T., Murphy, T., Buttery, H. J., Curran, J., Hunstead, R. W., Piestrzynski, B., Robertson,
724 J. G., & Sadler, E. M. 2003, MNRAS, 342, 1117
- 725 Max-Moerbeck, W., et al. 2011, ApJ, in preparation (OVRO variability paper)
- 726 Mücke, A., et al. 1997, A&A, 320, 33
- 727 Mukherjee, R., et al. 1997, ApJ, 490, 116
- 728 Myers, S. T., et al. 2003, MNRAS, 341, 1
- 729 Nagar, N. M., Wilson, A. S., & Falcke, H. 2001, ApJ, 559, L87
- 730 Padovani, P., Ghisellini, G., Fabian, A. C., & Celotti, A. 1993, MNRAS, 260, L21
- 731 Pavlidou, V., et al. 2011, ApJ, submitted (methodology paper)
- 732 Readhead, A. C. S., Lawrence, C. R., Myers, S. T., Sargent, W. L. W., Hardebeck, H. E., & Moffet,
733 A. T. 1989, ApJ, 346, 566

- 734 Richards, J. L., et al. 2010, ArXiv e-prints, arXiv:1011.3111
- 735 Salamon, M. H., & Stecker, F. W. 1994, ApJ, 430, L21
- 736 Schmitt, J. H. M. M. 1985, ApJ, 293, 178
- 737 Stecker, F. W., Salamon, M. H., & Malkan, M. A. 1993, ApJ, 410, L71
- 738 Stocke, J. T., Morris, S. L., Gioia, I. M., Maccacaro, T., Schild, R., Wolter, A., Fleming, T. A., &
739 Henry, J. P. 1991, ApJS, 76, 813
- 740 Taylor, G. B., et al. 2007, ApJ, 671, 1355
- 741 Tingay, S. J., Jauncey, D. L., King, E. A., Tzioumis, A. K., Lovell, J. E. J., & Edwards, P. G.
742 2003, PASJ, 55, 351
- 743 Unger, S. W., Booler, R. V., & Pedlar, A. 1984, MNRAS, 207, 679
- 744 Urry, C. M., & Padovani, P. 1995, PASP, 107, 803
- 745 Wall, J. V., & Jenkins, C. R. 2003, Practical Statistics for Astronomers, ed. Wall, J. V. & Jenkins,
746 C. R.

Table 1. Source list and radio data.

1FGL name	Other name	RA ($^{\circ}$)	Dec ($^{\circ}$)	Opt. type	SED type	z	S_8 (mJy)	Ref.	$S_{15, 1\text{yr mean}}$ (mJy)	$S_{15, 1\text{yr peak}}$ (mJy)	$S_{15, \text{non c.}}$ (mJy)
1FGL J0000.9−0745	CRATES J0001−0746	0.32512	−7.77417	BLL	LSP	...	116.2	Cr
1FGL J0004.7−4737	PKS 0002−478	1.14867	−47.60517	FSRQ	LSP	0.88	780.4	Cr
1FGL J0005.7+3815	B2 0003+38A	1.48825	38.33755	FSRQ	LSP	0.229	1078	Cr	541.9	703.3	541.2
1FGL J0008.9+0635	CRATES J0009+0628	2.26638	6.47256	BLL	LSP	...	196.5	Cr
1FGL J0011.1+0050	CGRaBS J0011+0057	2.87667	0.96439	FSRQ	LSP	1.492	278.7	Cr	249.3	364.8	205.6
1FGL J0013.1−3952	PKS 0010−401	3.24962	−39.90717	BLL	1554	Cr
1FGL J0013.7−5022	BZB J0014−5022	3.54675	−50.37575	BLL	HSP	...	13.4	N
1FGL J0017.4−0510	CGRaBS J0017−0512	4.39925	−5.21158	FSRQ	LSP	0.227	225.2	Cr	297.8	497.3	173.1
1FGL J0018.6+2945	BZB J0018+2947	4.61562	29.79178	BLL	HSP	...	3.5	F
1FGL J0019.3+2017	PKS 0017+200	4.90771	20.36267	BLL	LSP	...	1233	Cr	649.9	753.8	537.4
1FGL J0021.7−2556	CRATES J0021−2550	5.38563	−25.84703	BLL	ISP	...	37.6	Cr
1FGL J0022.5+0607	PKS 0019+058	5.63517	6.13450	BLL	LSP	...	301.2	Cr	396.3	471.3	534.5
1FGL J0023.0+4453	B3 0020+446	5.89767	44.94328	FSRQ	...	1.062	240	Cr	155.8	490.2	153.3
1FGL J0029.9−4221	PKS 0027−426	7.57283	−42.41292	FSRQ	LSP	0.495	596.4	Cr
1FGL J0033.5−1921	RBS 76	8.39292	−19.35944	BLL	HSP	0.61	38.8	F
1FGL J0035.1+1516	RX J0035.2+1515	8.81125	15.25111	BLL	HSP	...	15.2	F
1FGL J0038.4−2504	PKS 0035−252	9.56137	−24.98394	FSRQ	LSP	1.196	886.8	Cr
1FGL J0041.9+2318	PKS 0039+230	10.51896	23.33367	FSRQ	...	1.426	906.2	Cr	468.3	504.8	464.9
1FGL J0048.0−8412	PKS 0044−84	11.11192	−84.37781	FSRQ	...	1.032	426.6	Cr
1FGL J0045.3+2127	BZB J0045+2127	11.33042	21.46113	BLL	HSP	...	52.1	Cl
1FGL J0047.3−2512	NGC 253	11.88806	−25.28812	AGN	LSP	0.001	283.1	Cr
1FGL J0050.2+0235	PKS 0047+023	12.43017	2.61772	BLL	525.7	Cr	200.8	321.2	247.2
1FGL J0049.8−5738	PKS 0047−579	12.49775	−57.64067	FSRQ	LSP	1.797	1359	Cr
1FGL J0050.0−0446	PKS 0047−051	12.58971	−4.87242	FSRQ	...	0.92	534.4	Cr	262.2	364.5	279.9
1FGL J0050.6−0928	PKS 0048−09	12.67217	−9.48478	BLL	ISP	...	1207	Cr	1494	2378	728.7
1FGL J0051.1−0649	PKS 0048−071	12.78421	−6.83394	FSRQ	LSP	1.975	755.3	Cr	1281	1444	1209
1FGL J0058.4−3235	PKS 0055−328	14.50925	−32.57286	BLL	252.3	Cr
1FGL J0058.0+3314	CRATES J0058+3311	14.63363	33.18811	BLL	...	1.371	148.7	Cr
1FGL J0100.2+0747	CRATES J0100+0745	15.08662	7.76428	88	Cr
1FGL J0102.2+4223	CRATES J0102+4214	15.61313	42.23861	FSRQ	...	0.874	128.6	Cr
1FGL J0104.4−2406	PKS 0102−245	16.24250	−24.27456	FSRQ	...	1.747	260.9	Cr
1FGL J0108.6+0135	4C +01.02	17.16154	1.58342	FSRQ	LSP	2.107	2263	Cr	2445	2756	3665
1FGL J0109.0+1816	CRATES J0109+1816	17.28408	18.26875	BLL	HSP	0.145	83.7	Cr
1FGL J0112.0+2247	CGRaBS J0112+2244	18.02425	22.74411	BLL	ISP	0.265	493.4	Cr	787.3	1231	327.8

Table 1—Continued

1FGL name	Other name	RA ($^{\circ}$)	Dec ($^{\circ}$)	Opt. type	SED type	z	S_8 (mJy)	Ref.	$S_{15, 1\text{yr mean}}$ (mJy)	$S_{15, 1\text{yr peak}}$ (mJy)	$S_{15, \text{non c.}}$ (mJy)
1FGL J0112.9+3207	4C +31.03	18.20971	32.13822	FSRQ	LSP	0.603	386	Cr
1FGL J0113.8+4945	CGRaBS J0113+4948	18.36254	49.80669	FSRQ	LSP	0.395	528.9	Cr	866.9	1003	682.4
1FGL J0115.5+2519	BZB J0115+2519	18.94208	25.33139	BLL	HSP	...	26.9	Cl
1FGL J0115.5−1132	PKS 0113−118	19.05217	−11.60428	FSRQ	LSP	0.672	1391	Cr	961.1	1031	1129
1FGL J0118.7−2137	PKS 0116−219	19.73858	−21.69167	FSRQ	LSP	1.165	531.4	Cr
1FGL J0120.5−2700	PKS 0118−272	20.13192	−27.02347	BLL	ISP	0.557	774.4	Cr
1FGL J0128.6+4439	CLASS J0128+4439	22.17225	44.65499	FSRQ	...	0.228	56.4	Cl
1FGL J0132.6−1655	PKS 0130−17	23.18121	−16.91347	FSRQ	LSP	1.02	907.2	Cr	1739	2224	1591
1FGL J0136.5+3905	B3 0133+388	24.13581	39.09977	BLL	HSP	...	42.4	Cl
1FGL J0137.0+4751	OC 457	24.24413	47.85808	FSRQ	LSP	0.859	1644	Cr	3769	4322	4053
1FGL J0137.5−2428	PKS 0135−247	24.40979	−24.51489	FSRQ	LSP	0.835	761.3	Cr
1FGL J0141.7−0929	PKS 0139−09	25.35762	−9.47881	BLL	LSP	0.733	539.4	Cr	684.1	909.7	988.3
1FGL J0144.6+2703	CRATES J0144+2705	26.13983	27.08419	BLL	202.5	Cr
1FGL J0144.9−2732	PKS 0142−278	26.26417	−27.55953	FSRQ	LSP	1.148	666.5	Cr
1FGL J0154.1+0823	CRATES J0154+0823	28.51154	8.39753	BLL	157.5	Cr
1FGL J0155.0+4433	CLASS J0154+4433	28.72695	44.56055	BLL	38.9	Cl
1FGL J0157.5−4613	CGRaBS J0157−4614	29.46304	−46.23978	FSRQ	...	2.287	230.5	Cr
1FGL J0158.0−3931	CGRaBS J0158−3932	29.65883	−39.53431	BLL	ISP	...	296.1	Cr
1FGL J0159.5+1047	BZB J0159+1047	29.89292	10.78472	BLL	HSP	0.195	30.3	Cl
1FGL J0159.7−2741	CRATES J0159−2740	29.93062	−27.67739	BLL	LSP	...	64.9	Cr
1FGL J0202.1+0849	RX J0202.4+0849	30.61000	8.82028	BLL	LSP	...	40.9	F
1FGL J0203.5+7234	CGRaBS J0203+7232	30.88912	72.54825	BLL	281.3	Cr	439.5	511.4	472.5
1FGL J0203.5+3044	B2 0200+30	30.93898	30.69142	235	Cl
1FGL J0204.5+1516	4C +15.05	31.21004	15.23639	AGN	LSP	0.405	3325	Cr	1005	1262	1083
1FGL J0205.0−1702	PKS 0202−17	31.24029	−17.02217	FSRQ	LSP	1.74	1199	Cr	1475	1529	1436
1FGL J0205.3+3217	B2 0202+31	31.27054	32.20836	FSRQ	LSP	1.466	765.5	Cr	3215	3468	2691
1FGL J0208.6+3522	BZB J0208+3523	32.15913	35.38686	BLL	HSP	0.318	8.3	F
1FGL J0209.3−5229	BZB J0209−5229	32.33983	−52.48978	BLL	HSP	...	35.8	N
1FGL J0210.6−5101	PKS 0208−512	32.69254	−51.01733	BLL	LSP	1.003	2779	Cr
1FGL J0211.2+1049	CGRaBS J0211+1051	32.80492	10.85967	BLL	357.6	Cr	610.9	775.2	1109
1FGL J0213.2+2244	CLASS J0212+2244	33.22015	22.74784	BLL	HSP	0.459	55.9	Cl
1FGL J0217.0−0829	PKS 0214−085	34.26108	−8.34786	FSRQ	LSP	0.607	277.8	Cr
1FGL J0217.2+0834	CGRaBS J0217+0837	34.32138	8.61775	...	ISP	...	323.2	Cr	497.8	637.6	438.3
1FGL J0217.9+0144	PKS 0215+015	34.45400	1.74714	FSRQ	LSP	1.715	1179	Cr	1659	2095	1988

Table 1—Continued

1FGL name	Other name	RA ($^{\circ}$)	Dec ($^{\circ}$)	Opt. type	SED type	z	S_8 (mJy)	Ref.	$S_{15, 1\text{yr mean}}$ (mJy)	$S_{15, 1\text{yr peak}}$ (mJy)	$S_{15, \text{non c.}}$ (mJy)
1FGL J0221.0+3555	B2 0218+35	35.27279	35.93714	FSRQ	LSP	0.944	1240	Cr	1445	1653	1504
1FGL J0222.1–1618	PKS 0219–164	35.50304	–16.25461	FSRQ	LSP	0.698	556.8	Cr	251.7	320.7	224.2
1FGL J0222.6+4302	3C 66A	35.66500	43.03528	BLL	HSP	...	728.4	Cl
1FGL J0229.3–3644	PKS 0227–369	37.36854	–36.73245	FSRQ	LSP	2.115	287.2	Cr
1FGL J0230.8+4031	B3 0227+403	37.69046	40.54808	FSRQ	...	1.019	581.1	Cr	477.6	602.1	461.7
1FGL J0238.3–6132	PKS 0235–618	39.22179	–61.60422	FSRQ	LSP	0.465	416.7	Cr
1FGL J0237.5–3603	RBS 334	39.39169	–36.05899	...	HSP	...	23.8	F
1FGL J0237.9+2848	4C +28.07	39.46838	28.80250	FSRQ	LSP	1.213	2770	Cr	3016	3366	2278
1FGL J0238.6–3117	BZB J0238–3116	39.63533	–31.28283	BLL	HSP	...	5.4	F
1FGL J0238.6+1637	PKS 0235+164	39.66221	16.61647	BLL	LSP	0.94	5454	Cr	3576	6571	1022
1FGL J0243.5+7116	CRATES J0243+7120	40.87871	71.33830	BLL	166	Cr
1FGL J0245.4+2413	B2 0242+23	41.32025	24.09311	FSRQ	...	2.243	242.2	Cr
1FGL J0245.9–4652	PKS 0244–470	41.50046	–46.85483	FSRQ	LSP	1.385	600.6	Cr
1FGL J0252.8–2219	PKS 0250–225	43.19983	–22.32372	FSRQ	LSP	1.427	390.3	Cr
1FGL J0257.8–1204	CGRaBS J0257–1212	44.42083	–12.20042	FSRQ	...	1.391	238.5	Cr	211.1	247.3	223.8
1FGL J0259.5+0743	PKS 0256+075	44.86283	7.79433	FSRQ	LSP	0.893	456.3	Cr
1FGL J0303.5–2406	PKS 0301–243	45.86042	–24.11981	BLL	ISP	0.26	213.3	Cr
1FGL J0303.4–6209	PKS 0302–623	45.96092	–62.19044	FSRQ	LSP	1.351	1477	Cr
1FGL J0305.0–0601	CRATES J0305–0607	46.25238	–6.12819	BLL	45.4	Cr
1FGL J0308.3+0403	NGC 1218	47.10927	4.11092	AGN	LSP	0.029	750	U84
1FGL J0310.1–6058	PKS 0308–611	47.48363	–60.97761	FSRQ	LSP	1.48	968.6	Cr
1FGL J0310.6+3812	B3 0307+380	47.70783	38.24828	FSRQ	LSP	0.816	460.2	Cr	499.4	851.6	718
1FGL J0312.6+0131	PKS 0310+013	48.18167	1.55486	FSRQ	...	0.664	453.4	Cr	467.1	554.2	326.6
1FGL J0315.9–1033	PKS 0313–107	48.98696	–10.52761	FSRQ	...	1.565	163.6	Cr
1FGL J0316.1+0904	BZB J0316+0904	49.05306	9.07870	BLL	HSP	...	47.2	Cl
1FGL J0315.9–2609	RX J0316.2–2607	49.06250	–26.13222	BLL	HSP	0.443	23.5	F
1FGL J0319.7+4130	NGC 1275	49.95067	41.51170	AGN	LSP	0.018	28 010	Cr	18 160	19 730	20 820
1FGL J0319.7+1847	BZB J0319+1845	49.96583	18.75950	BLL	HSP	0.19	18.5	N
1FGL J0322.1+2336	BZB J0321+2326	50.49987	23.60313	BLL	ISP	...	47.6	Cl
1FGL J0325.0+3403	B2 0321+33B	51.17150	34.17939	AGN	HSP	0.061	277	Cr
1FGL J0325.9+2219	CGRaBS J0325+2224	51.40337	22.40011	FSRQ	LSP	2.066	528.2	Cr	757.8	963.5	1216
1FGL J0325.9–1649	RBS 421	51.42167	–16.77111	BLL	HSP	0.291	22.3	F
1FGL J0326.2+0222	1ES 0323+022	51.55812	2.42076	BLL	HSP	0.147	40.4	Cl
1FGL J0334.2–4010	PKS 0332–403	53.55692	–40.14034	BLL	LSP	...	960.4	Cr

Table 1—Continued

1FGL name	Other name	RA ($^{\circ}$)	Dec ($^{\circ}$)	Opt. type	SED type	z	S_8 (mJy)	Ref.	$S_{15, 1\text{yr mean}}$ (mJy)	$S_{15, 1\text{yr peak}}$ (mJy)	$S_{15, \text{non c.}}$ (mJy)
1FGL J0334.4–3727	CRATES J0334–3725	53.56425	–37.42870	BLL	ISP	...	165.2	Cr
1FGL J0339.1–1734	PKS 0336–177	54.80712	–17.60022	AGN	HSP	0.065	56.8	Cr
1FGL J0343.4–2536	PKS 0341–256	55.83138	–25.50480	FSRQ	LSP	1.419	308.1	Cr
1FGL J0348.5–2751	PKS 0346–279	57.15896	–27.82042	FSRQ	LSP	0.987	1351	Cr
1FGL J0349.9–2104	PKS 0347–211	57.49096	–21.04658	FSRQ	LSP	2.944	319	Cr
1FGL J0354.6+8009	CRATES J0354+8009	58.69221	80.15800	348.2	Cr
1FGL J0357.1–4949	PKS 0355–500	59.25062	–49.93017	BLL	ISP	...	92.3	Cr
1FGL J0402.1–2618	CRATES J0402–2615	60.50325	–26.26094	85	Cr
1FGL J0403.9–3603	PKS 0402–362	60.97396	–36.08386	FSRQ	LSP	1.417	2529	Cr
1FGL J0407.4–3827	PKS 0405–385	61.74600	–38.44111	FSRQ	LSP	1.285	1230	Cr
1FGL J0413.4–5334	CRATES J0413–5332	63.30629	–53.53361	FSRQ	...	1.027	44	Cr
1FGL J0416.5–1851	PKS 0414–189	64.15225	–18.85231	FSRQ	LSP	1.536	1066	Cr	893.3	1125	846.7
1FGL J0416.8+0107	CRATES J0416+0105	64.21871	1.08997	BLL	HSP	0.287	46.8	Cr
1FGL J0422.0–0647	CRATES J0422–0643	65.54500	–6.72925	FSRQ	ISP	0.242	173.7	Cr
1FGL J0422.1+0211	PKS 0420+022	65.71754	2.32414	FSRQ	LSP	2.277	975	Cr	908.2	1139	873.5
1FGL J0423.2–0118	PKS 0420–01	65.81583	–1.34253	FSRQ	LSP	0.915	2409	Cr	4656	6037	8284
1FGL J0424.8+0036	PKS 0422+00	66.19517	0.60175	BLL	LSP	...	283.9	Cr
1FGL J0428.6–3756	PKS 0426–380	67.16842	–37.93878	BLL	LSP	1.111	1614	Cr
1FGL J0430.4–2509	CRATES J0430–2507	67.56679	–25.12750	BLL	LSP	...	31.9	Cr
1FGL J0433.5+2905	CGRaBS J0433+2905	68.40762	29.09875	BLL	LSP	...	432.8	Cr	296.8	450.1	253.3
1FGL J0434.1–2018	CRATES J0434–2015	68.53296	–20.25475	BLL	82.2	Cr
1FGL J0438.8–1250	PKS 0436–129	69.64592	–12.85097	FSRQ	...	1.286	352.7	Cr	374.1	446.5	466.2
1FGL J0440.6+2748	B2 0437+27B	70.20987	27.84633	BLL	45.5	Cr
1FGL J0448.5–1633	BZB J0448–1632	72.15683	–16.54522	BLL	HSP	...	8.6	F
1FGL J0449.5–4350	PKS 0447–439	72.35367	–43.83603	BLL	HSP	0.205	114.1	Cr
1FGL J0453.2–2805	PKS 0451–28	73.31104	–28.12703	FSRQ	LSP	2.56	1583	Cr
1FGL J0455.6–4618	PKS 0454–46	73.96146	–46.26647	FSRQ	LSP	0.858	2300	Cr
1FGL J0456.4–3132	CRATES J0456–3136	74.15283	–31.60347	FSRQ	LSP	0.865	150.6	Cr
1FGL J0457.0–2325	PKS 0454–234	74.26325	–23.41444	FSRQ	LSP	1.003	1561	Cr
1FGL J0457.9+0649	4C +06.21	74.28212	6.75203	FSRQ	LSP	0.405	434.8	Cr	630.6	775.2	562.3
1FGL J0501.0–0200	PKS 0458–02	75.30338	–1.98731	FSRQ	LSP	2.291	1958	Cr	955.1	1108	1139
1FGL J0505.2+0420	CRATES J0505+0415	76.39487	4.26517	BLL	HSP	...	63.1	Cr
1FGL J0505.8–0416	CRATES J0505–0419	76.46346	–4.32408	FSRQ	LSP	1.481	79.2	Cr
1FGL J0507.9+6738	1ES 0502+675	76.98405	67.62341	BLL	HSP	0.416	24.1	Cl

Table 1—Continued

1FGL name	Other name	RA (°)	Dec (°)	Opt. type	SED type	z	S_8 (mJy)	Ref.	$S_{15, 1\text{yr mean}}$ (mJy)	$S_{15, 1\text{yr peak}}$ (mJy)	$S_{15, \text{non c.}}$ (mJy)
1FGL J0509.3+0540	CGRaBS J0509+0541	77.35817	5.69314	BLL	LSP	...	702.4	Cr	609.9	669.6	555.4
1FGL J0509.2+1015	PKS 0506+101	77.36442	10.19572	FSRQ	...	0.621	276.5	Cr
1FGL J0516.7-6207	PKS 0516-621	79.18754	-62.11806	...	LSP	...	702.8	Cr
1FGL J0522.8-3632	PKS 0521-36	80.74160	-36.45857	BLL	ISP	0.055	4990	T03
1FGL J0526.3-4829	PKS 0524-485	81.56942	-48.51017	FSRQ	LSP	1.299	419.5	Cr
1FGL J0531.0+1331	PKS 0528+134	82.73508	13.53197	FSRQ	LSP	2.07	2458	Cr	2860	3311	1702
1FGL J0532.9+0733	OG 050	83.16250	7.54536	FSRQ	LSP	1.254	2763	Cr	1429	2176	1361
1FGL J0533.0-8324	PKS 0541-834	83.41038	-83.40997	FSRQ	...	0.774	149.6	Cr
1FGL J0536.2-3348	FRBA J0536-3343	84.12131	-33.71737	BLL	HSP	...	51.4	F
1FGL J0538.8-4404	PKS 0537-441	84.70979	-44.08575	BLL	LSP	0.892	3073	Cr
1FGL J0539.1-2847	PKS 0537-286	84.97617	-28.66553	FSRQ	LSP	3.104	1330	Cr
1FGL J0543.8-5531	BZB J0543-5532	85.98667	-55.53442	BLL	HSP	...	41	N
1FGL J0557.6-3831	CRATES J0558-3838	89.52696	-38.64214	BLL	HSP	0.302	39.9	Cr
1FGL J0559.2-7500	PKS 0600-749	89.69192	-74.98480	BLL	178.9	Cr
1FGL J0600.7-7037	PKS 0601-70	90.29717	-70.60239	FSRQ	...	2.409	117.2	Cr
1FGL J0607.2+4739	CGRaBS J0607+4739	91.84687	47.66306	BLL	ISP	...	403.4	Cr	334.6	452.9	275.6
1FGL J0608.2-0837	PKS 0605-08	91.99875	-8.58056	FSRQ	LSP	0.872	1970	Cr	1193	1467	1829
1FGL J0608.0-1521	CRATES J0608-1520	92.00638	-15.34361	...	LSP	...	215.3	Cr
1FGL J0612.7+4120	B3 0609+413	93.21329	41.37706	BLL	245.2	Cr	327.6	512.9	268.4
1FGL J0616.9+5701	CRATES J0617+5701	94.32050	57.02122	BLL	335.2	Cr
1FGL J0617.7-1718	CRATES J0617-1715	94.38925	-17.25697	BLL	LSP	0.32	154.3	Cr
1FGL J0622.3-2604	CRATES J0622-2606	95.59888	-26.10767	44.2	Cr
1FGL J0625.4+4440	CGRaBS J0625+4440	96.32608	44.66711	BLL	185.6	Cr	162.5	260.1	118.4
1FGL J0625.9-5430	CGRaBS J0625-5438	96.46771	-54.64739	FSRQ	LSP	2.051	291.8	Cr
1FGL J0626.6-4254	CRATES J0626-4253	96.53292	-42.89219	69.2	Cr
1FGL J0627.3-3530	PKS 0625-35	96.77808	-35.48761	AGN	ISP	0.055	701	Cr
1FGL J0629.6-2000	PKS 0627-199	97.34900	-19.98881	BLL	LSP	...	1084	Cr	806.1	1240	961.1
1FGL J0630.9-2406	CRATES J0630-2406	97.74804	-24.11281	BLL	HSP	...	84.9	Cr
1FGL J0636.1-7521	PKS 0637-75	98.94358	-75.27131	FSRQ	LSP	0.651	4564	Cr
1FGL J0639.9+7325	CGRaBS J0639+7324	99.84150	73.41611	FSRQ	LSP	1.854	733.1	Cr	876.4	990.5	882.1
1FGL J0645.5+6033	BZU J0645+6024	101.25571	60.41175	AGN	ISP	0.832	25.7	F
1FGL J0650.7+2503	1ES 0647+250	102.69371	25.04989	BLL	HSP	...	66.5	Cr
1FGL J0654.4+5042	CGRaBS J0654+5042	103.59204	50.70664	305	Cr	228.1	299.2	201.6
1FGL J0654.3+4514	B3 0650+453	103.59879	45.23986	FSRQ	LSP	0.933	392.9	Cr	546.1	904.9	187.9

Table 1—Continued

1FGL name	Other name	RA (°)	Dec (°)	Opt. type	SED type	z	S_8 (mJy)	Ref.	$S_{15, 1\text{yr mean}}$ (mJy)	$S_{15, 1\text{yr peak}}$ (mJy)	$S_{15, \text{non c.}}$ (mJy)
1FGL J0700.4–6611	PKS 0700–661	105.13017	–66.17939	...	ISP	...	193.5	Cr
1FGL J0702.0–4628	PKS 0700–465	105.39392	–46.57683	FSRQ	LSP	0.822	607	Cr
1FGL J0706.3–4849	CRATES J0705–4847	106.49454	–48.79014	43.8	Cr
1FGL J0710.6+5911	BZB J0710+5908	107.62528	59.13899	BLL	HSP	0.125	41.7	Cl
1FGL J0711.4+4731	B3 0707+476	107.69213	47.53642	BLL	LSP	...	620.1	Cr
1FGL J0712.7+5033	CGRaBS J0712+5033	108.18183	50.55630	BLL	ISP	...	396.3	Cr	394.6	648.4	216.5
1FGL J0714.0+1935	CLASS J0713+1935	108.48200	19.58344	FSRQ	...	0.534	209.7	Cl
1FGL J0718.7–4320	CRATES J0718–4319	109.68183	–43.33047	...	ISP	...	68.4	Cr
1FGL J0719.3+3306	B2 0716+33	109.83092	33.11936	FSRQ	LSP	0.779	176.1	Cr
1FGL J0721.9+7120	CGRaBS J0721+7120	110.47271	71.34344	BLL	ISP	0.31	594.8	Cr	2008	3186	2206
1FGL J0722.3+5837	BZB J0723+5841	110.80817	58.68844	BLL	HSP	...	8.9	F
1FGL J0725.3+1431	4C+14.23	111.32004	14.42047	FSRQ	...	1.038	1148	Cr	628.8	728.8	734.1
1FGL J0730.0+3305	BZB J0730+3307	112.60854	33.12297	BLL	HSP	0.112	6.7	F
1FGL J0734.1–7715	PKS 0736–770	113.68133	–77.18692	404.9	Cr
1FGL J0738.2+1741	PKS 0735+17	114.53079	17.70528	BLL	LSP	0.424	3738	Cr	709.8	837.4	673.4
1FGL J0739.1+0138	PKS 0736+01	114.82512	1.61794	FSRQ	LSP	0.191	1711	Cr	1389	1897	1117
1FGL J0742.2+5443	CRATES J0742+5444	115.66579	54.74020	FSRQ	LSP	0.723	142.8	Cr
1FGL J0745.2+7438	1ES 0737+746	116.02192	74.56600	BLL	HSP	0.315	20.1	N
1FGL J0746.6+2548	B2 0743+25	116.60783	25.81725	FSRQ	LSP	2.979	291.7	Cr
1FGL J0750.6+1235	PKS 0748+126	117.71688	12.51800	FSRQ	LSP	0.889	1968	Cr	4373	4784	4379
1FGL J0752.8+5353	4C+54.15	118.25575	53.88322	BLL	LSP	0.2	1197	Cr	877.1	1056	622.4
1FGL J0757.2+0956	PKS 0754+100	119.27767	9.94303	BLL	ISP	0.266	1364	Cr	1195	1459	1608
1FGL J0800.5+4407	B3 0757+441	120.28447	44.01949	230.6	Cl
1FGL J0806.2+6148	CGRaBS J0805+6144	121.32575	61.73992	FSRQ	LSP	3.033	725.7	Cr	599.7	727.9	501.7
1FGL J0804.7+7534	RX J0805.4+7534	121.36042	75.57361	BLL	HSP	0.121	34.6	F
1FGL J0807.0–0544	PKS 0804–05	121.79008	–5.68719	288.2	Cr
1FGL J0808.2–0750	PKS 0805–07	122.06475	–7.85275	FSRQ	LSP	1.837	1784	Cr	1058	1958	2309
1FGL J0809.4+3455	B2 0806+35	122.41204	34.92700	BLL	HSP	0.082	152.1	Cr
1FGL J0809.5+5219	CRATES J0809+5218	122.45496	52.31619	BLL	HSP	0.138	154.2	Cr
1FGL J0811.1–7527	CRATES J0811–7530	122.76321	–75.50772	...	ISP	...	82.2	Cr
1FGL J0811.2+0148	PKS 0808+019	122.86129	1.78117	BLL	LSP	1.148	1285	Cr	1034	1267	1103
1FGL J0815.0+6434	CGRaBS J0814+6431	123.66329	64.52278	BLL	ISP	...	221.6	Cr	144.6	168.7	170.3
1FGL J0816.7+5739	BZB J0816+5739	124.09926	57.65264	BLL	HSP	...	92	Cl
1FGL J0816.4–1311	BZB J0816–1311	124.11336	–13.19794	BLL	HSP	...	41.4	Cr

Table 1—Continued

1FGL name	Other name	RA ($^{\circ}$)	Dec ($^{\circ}$)	Opt. type	SED type	z	S_8 (mJy)	Ref.	$S_{15, 1\text{yr mean}}$ (mJy)	$S_{15, 1\text{yr peak}}$ (mJy)	$S_{15, \text{non c.}}$ (mJy)
1FGL J0818.0–0938	CGRaBS J0817–0933	124.45729	−9.55847	BLL	407.4	Cr	238.5	319.3	258.8
1FGL J0818.2+4222	B3 0814+425	124.56667	42.37928	BLL	LSP	...	1041	Cr	1321	1609	1978
1FGL J0825.0+5555	OJ 535	126.19683	55.87853	FSRQ	LSP	1.417	1736	Cr	652.3	767.1	783.8
1FGL J0825.9+0309	PKS 0823+033	126.45975	3.15681	BLL	LSP	0.506	1873	Cr	1570	1998	588.3
1FGL J0830.5+2407	B2 0827+24	127.71704	24.18328	FSRQ	LSP	0.94	793.7	Cr	1467	1606	812.9
1FGL J0831.6+0429	PKS 0829+046	127.95367	4.49419	BLL	LSP	0.174	1225	Cr	581.7	764.2	603.8
1FGL J0834.4+4221	B3 0830+425	128.47454	42.40053	FSRQ	LSP	0.249	560.8	Cr	346.5	1892	353
1FGL J0835.4+0936	CRATES J0835+0937	128.93008	9.62167	BLL	57.4	Cr
1FGL J0839.5+0059	PKS 0837+012	129.95671	1.07408	FSRQ	LSP	1.123	620.3	Cr	571.6	627.5	552.9
1FGL J0842.2+7054	4C+71.07	130.35150	70.89506	FSRQ	LSP	2.218	1752	Cr
1FGL J0842.2+0251	BZB J0842+0252	130.60630	2.88131	BLL	HSP	0.425	13	F
1FGL J0844.0+5314	BZB J0844+5312	131.04876	53.21405	BLL	HSP	...	42.2	Cl
1FGL J0846.9–2334	CRATES J0847–2337	131.75650	−23.61711	...	HSP	...	126.5	Cr
1FGL J0847.2+1134	BZB J0847+1133	131.80388	11.56396	BLL	HSP	0.198	12.3	Cl
1FGL J0849.9+4852	CRATES J0850+4854	132.50221	48.91461	...	ISP	...	71.1	Cr
1FGL J0850.0–1213	CGRaBS J0850–1213	132.54012	−12.22656	FSRQ	LSP	0.566	783.2	Cr	573.3	848.7	465.5
1FGL J0850.2+3457	RX J0850.6+3455	132.65083	34.92305	BLL	HSP	0.149	32.8	F
1FGL J0854.8+2006	OJ 287	133.70362	20.10850	BLL	ISP	0.306	3415	Cr	3687	4667	9208
1FGL J0856.6–1105	CGRaBS J0856–1105	134.17417	−11.08736	...	LSP	...	519.5	Cr	532.6	643.7	411.7
1FGL J0905.5+1356	CRATES J0905+1358	136.39579	13.96842	42.8	Cr
1FGL J0909.2+2310	RX J0909.0+2311	137.25250	23.18722	BLL	HSP	0.223	31.9	F
1FGL J0909.0+0126	PKS 0906+01	137.29204	1.35989	FSRQ	LSP	1.024	1031	Cr	1356	1481	964.7
1FGL J0909.6–0229	PKS 0907–023	137.43717	−2.52511	FSRQ	...	0.957	323	Cr
1FGL J0910.7+3332	Ton 1015	137.65433	33.49011	BLL	HSP	0.354	88.6	Cr
1FGL J0911.0+2247	CGRaBS J0910+2248	137.67554	22.80989	FSRQ	...	2.661	178.8	Cr	152	190.3	169.1
1FGL J0912.3+4127	B3 0908+416B	138.04842	41.43594	FSRQ	...	2.563	166.9	Cr
1FGL J0915.7+2931	B2 0912+29	138.96833	29.55667	BLL	HSP	...	186.1	Cr
1FGL J0920.9+4441	B3 0917+449	140.24358	44.69833	FSRQ	LSP	2.19	1368	Cr	1942	2136	2118
1FGL J0919.6+6216	OK 630	140.40096	62.26450	FSRQ	LSP	1.446	1532	Cr	1366	1580	1253
1FGL J0923.2+4121	B3 0920+416	140.88042	41.42428	AGN	...	0.028	235.2	Cr	354.9	698.7	326.2
1FGL J0924.2+2812	B2 0920+28	140.96467	28.25694	FSRQ	...	0.744	218.4	Cr
1FGL J0934.5+3929	CGRaBS J0934+3926	143.52779	39.44225	BLL	188.3	Cr	155.1	551.8	125.8
1FGL J0937.7+5005	CGRaBS J0937+5008	144.30138	50.14780	FSRQ	LSP	0.276	372.5	Cr	241.6	379.8	420.7
1FGL J0941.2+6149	BZB J0940+6148	145.09353	61.80728	BLL	HSP	0.211	14.2	F

Table 1—Continued

1FGL name	Other name	RA (°)	Dec (°)	Opt. type	SED type	z	S_8 (mJy)	Ref.	$S_{15, 1\text{yr mean}}$ (mJy)	$S_{15, 1\text{yr peak}}$ (mJy)	$S_{15, \text{non c.}}$ (mJy)
1FGL J0941.2+2722	CGRaBS J0941+2728	145.45046	27.47744	FSRQ	...	1.306	227	Cr	200.4	248.5	225.8
1FGL J0945.6+5754	CRATES J0945+5757	146.42600	57.96325	BLL	ISP	0.229	69	Cr
1FGL J0946.6+1012	CRATES J0946+1017	146.64613	10.28503	FSRQ	...	1.007	292.8	Cr
1FGL J0949.0+0021	CGRaBS J0948+0022	147.23883	0.37378	FSRQ	HSP	0.585	226.8	Cr	268.7	429.3	392
1FGL J0952.2+3926	BZB J0952+3936	148.06129	39.60442	BLL	HSP	...	2.5	N
1FGL J0953.0−0838	CRATES J0953−0840	148.26133	−8.67178	BLL	HSP	...	73.7	Cr
1FGL J0956.5+6938	M 82	148.96969	69.67938	AGN	ISP	0.001	22.4	Cr
1FGL J0956.9+2513	B2 0954+25A	149.20779	25.25444	FSRQ	LSP	0.712	1787	Cr	911.5	1274	820.4
1FGL J0957.7+5523	4C +55.17	149.40908	55.38269	FSRQ	LSP	0.896	1499	Cr
1FGL J1000.1+6539	CGRaBS J0958+6533	149.69688	65.56522	BLL	ISP	0.367	1247	Cr	1398	2569	1481
1FGL J1000.9+2915	CGRaBS J1001+2911	150.29254	29.19375	BLL	LSP	...	296	Cr	416.9	497	501.9
1FGL J1007.1−2157	PKS 1004−217	151.69338	−21.98900	FSRQ	LSP	0.33	482.5	Cr
1FGL J1007.0+3454	BZB J1006+3454	151.73527	34.91255	BLL	HSP	...	6.5	N
1FGL J1007.9+0619	CGRaBS J1008+0621	152.00342	6.35589	BLL	ISP	...	657.1	Cr	507.8	629.1	331.2
1FGL J1011.0−0156	CRATES J1010−0200	152.71529	−2.00544	FSRQ	...	0.887	490.6	Cr
1FGL J1012.2+0634	CRATES J1012+0630	153.05562	6.51589	BLL	LSP	0.727	154.2	Cr
1FGL J1012.7+2440	CRATES J1012+2439	153.17242	24.65650	FSRQ	...	1.805	73.8	Cr
1FGL J1015.1+4927	1ES 1011+496	153.76721	49.43353	BLL	HSP	0.2	252.2	Cr	277.9	333.9	272.7
1FGL J1016.1+0514	CRATES J1016+0513	154.01308	5.21731	FSRQ	...	1.713	298.7	Cr
1FGL J1022.8−0115	BZB J1022−0113	155.68219	−1.21736	BLL	HSP	...	4.7	F
1FGL J1024.0−4332	BZB J1023−4336	155.98379	−43.60069	BLL	HSP	...	32.3	N
1FGL J1028.7−8543	PKS 1029−85	156.64650	−85.72086	97.5	Cr
1FGL J1027.1−1747	BZB J1026−1748	156.74383	−17.81625	BLL	HSP	0.114	11.5	N
1FGL J1031.0+5051	1ES 1028+511	157.82716	50.89328	BLL	HSP	0.361	32.6	Cl
1FGL J1032.7+3737	TXS 1029+378	158.16959	37.64056	BLL	63.1	F
1FGL J1033.2+4116	B3 1030+415	158.26546	41.26839	FSRQ	LSP	1.117	384.4	Cr	989.7	1145	2374
1FGL J1037.7−2820	PKS B1035−281	159.42692	−28.38447	277.6	Cr
1FGL J1037.7+5711	CRATES J1037+5711	159.43463	57.19878	BLL	HSP	...	82.5	Cr
1FGL J1043.1+2404	B2 1040+24A	160.78762	24.14317	BLL	ISP	0.56	685.4	Cr	956.8	1713	1077
1FGL J1048.7+8054	CGRaBS J1044+8054	161.09613	80.91094	FSRQ	LSP	1.26	1021	Cr	667.9	803	710.4
1FGL J1048.5+7239	CRATES J1047+7238	161.94800	72.63695	31.2	Cr
1FGL J1048.8+7145	CGRaBS J1048+7143	162.11508	71.72664	FSRQ	LSP	1.15	1284	Cr	1117	1350	1336
1FGL J1051.9+0106	BZB J1051+0103	162.96598	1.05300	BLL	LSP	0.265	11.5	Cl
1FGL J1053.6+4927	BZB J1053+4929	163.43386	49.49888	BLL	HSP	0.14	40.3	Cl

Table 1—Continued

1FGL name	Other name	RA (°)	Dec (°)	Opt. type	SED type	z	S_8 (mJy)	Ref.	$S_{15, 1\text{yr mean}}$ (mJy)	$S_{15, 1\text{yr peak}}$ (mJy)	$S_{15, \text{non c.}}$ (mJy)
1FGL J1054.5+2212	CLASS J1054+2210	163.62760	22.18189	BLL	ISP	...	41.6	Cl
1FGL J1058.4+0134	PKS 1055+01	164.62333	1.56633	FSRQ	LSP	0.888	3365	Cr	4612	5033	5003
1FGL J1058.6+5628	CGRaBS J1058+5628	164.65721	56.46978	BLL	HSP	0.143	189.8	Cr	163.3	188.6	152.7
1FGL J1058.1−8006	PKS 1057−79	164.68083	−80.06506	BLL	LSP	0.581	1683	Cr
1FGL J1059.3−1132	PKS B1056−113	164.80179	−11.57297	BLL	ISP	...	184.4	Cr
1FGL J1103.7−2329	CRATES J1103−2329	165.90671	−23.49200	BLL	HSP	0.186	38.8	Cr
1FGL J1104.4+0734	CRATES J1104+0730	166.10029	7.51478	BLL	98.7	Cr
1FGL J1104.4+3812	Mkn 421	166.11379	38.20883	BLL	HSP	0.03	631.6	Cr	444.8	483.5	463.1
1FGL J1106.5+2809	CRATES J1106+2812	166.53025	28.21305	193.2	Cr
1FGL J1107.8+1502	BZB J1107+1502	166.95027	15.03626	BLL	HSP	0.259	24.8	Cl
1FGL J1110.2−1839	CRATES J1110−1835	167.61571	−18.59800	18.1	Cr
1FGL J1109.9+7134	BZB J1110+7133	167.65666	71.56571	BLL	HSP	...	19.9	Cl
1FGL J1112.8+3444	CRATES J1112+3446	168.16154	34.77753	FSRQ	...	1.949	160.5	Cr
1FGL J1117.1+2013	CRATES J1117+2014	169.27608	20.23539	BLL	HSP	0.138	67.3	Cr
1FGL J1118.0+5354	BZB J1117+5355	169.48931	53.93189	BLL	HSP	...	15.6	F
1FGL J1119.5−3044	BZB J1119−3047	169.91458	−30.78894	BLL	HSP	0.412	9.4	N
1FGL J1121.0+4209	1ES 1118+424	170.20025	42.20346	BLL	HSP	0.124	27	Cl
1FGL J1121.5−0554	PKS 1118−05	170.35462	−5.89900	FSRQ	LSP	1.297	374.6	Cr
1FGL J1123.9+2339	OM 235	171.01129	23.61275	BLL	472.7	Cr	465.7	2363	548.9
1FGL J1125.5−3559	CRATES J1125−3557	171.38117	−35.95089	...	ISP	...	129.4	Cr
1FGL J1126.0−0741	BZB J1125−0742	171.46662	−7.70586	BLL	HSP	0.279	35.5	N
1FGL J1126.8−1854	PKS 1124−186	171.76829	−18.95483	FSRQ	LSP	1.048	1418	Cr	1701	2129	1632
1FGL J1136.6+7009	Mkn 180	174.11004	70.15759	BLL	HSP	0.045	213.7	Cr	174.8	871.4	169.9
1FGL J1136.2+6739	BZB J1136+6737	174.12536	67.61787	BLL	HSP	0.136	37.4	Cl
1FGL J1136.9+2551	BZB J1136+2550	174.20879	25.84788	BLL	HSP	0.156	14.5	F
1FGL J1141.8+1549	CRATES J1142+1547	175.53225	15.79839	274	Cr
1FGL J1146.8+4004	B2 1144+40	176.74292	39.97620	FSRQ	...	1.089	575.7	Cr	862.7	961.8	872.1
1FGL J1146.9−3812	PKS 1144−379	176.75571	−38.20306	FSRQ	LSP	1.048	2476	Cr
1FGL J1147.7−0722	PKS 1145−071	176.96479	−7.41142	FSRQ	LSP	1.342	884.9	Cr	630.4	696.8	680
1FGL J1150.2+2419	B2 1147+24	177.58004	24.29831	BLL	LSP	0.2	745.7	Cr	731.9	827.5	717.2
1FGL J1150.5+4152	BZB J1150+4154	177.64437	41.91133	BLL	HSP	...	22.2	F
1FGL J1151.6+5857	CRATES J1151+5859	177.85275	58.98822	BLL	ISP	...	102.2	Cr
1FGL J1151.4−1345	CRATES J1151−1347	177.87488	−13.79744	30.6	Cr
1FGL J1152.2−0836	PKS B1149−084	178.06858	−8.68425	FSRQ	...	2.367	563.9	Cr	860	1269	1424

Table 1—Continued

1FGL name	Other name	RA ($^{\circ}$)	Dec ($^{\circ}$)	Opt. type	SED type	z	S_8 (mJy)	Ref.	$S_{15, 1\text{yr mean}}$ (mJy)	$S_{15, 1\text{yr peak}}$ (mJy)	$S_{15, \text{non c.}}$ (mJy)
1FGL J1154.0–0008	BZB J1154–0010	178.51898	−0.16940	BLL	HSP	0.254	11.7	F
1FGL J1154.2–3242	PKS 1151–324	178.52671	−32.71331	305.8	Cr
1FGL J1159.4+2914	4C+29.45	179.88262	29.24550	FSRQ	LSP	0.729	1233	Cr	2932	3533	1489
1FGL J1202.9+6032	CRATES J1203+6031	180.76462	60.52197	AGN	ISP	0.065	191.4	Cr
1FGL J1204.4+1139	BZB J1204+1145	181.05049	11.76539	BLL	HSP	0.296	14.3	N
1FGL J1204.3–0714	CRATES J1204–0710	181.06942	−7.16917	BLL	ISP	0.185	153.8	Cr
1FGL J1205.9–2637	PKS 1203–26	181.38842	−26.56792	FSRQ	LSP	0.786	596.2	Cr
1FGL J1209.3+5444	CRATES J1208+5441	182.22608	54.69950	FSRQ	...	1.344	262	Cr
1FGL J1209.4+4119	B3 1206+416	182.34492	41.32817	BLL	LSP	...	485.1	Cr	178.3	1088	118.6
1FGL J1209.7+1806	CRATES J1209+1810	182.46567	18.16856	FSRQ	...	0.845	136.3	Cr
1FGL J1214.9+5004	BZB J1215+5002	183.75327	50.03768	BLL	67.5	N
1FGL J1217.7+3007	B2 1215+30	184.46700	30.11683	BLL	HSP	0.13	334.9	Cr	376.8	452.9	342.3
1FGL J1219.8–0309	FRBA J1219–0314	184.94041	−3.24000	BLL	HSP	0.299	26.2	F
1FGL J1221.5+7106	CRATES J1220+7105	185.01513	71.09197	FSRQ	...	0.451	188.1	Cr
1FGL J1220.2+3432	CGRaBS J1220+3431	185.03454	34.52269	BLL	LSP	...	314.1	Cr	151.3	187.6	124.1
1FGL J1221.3+3008	B2 1218+30	185.34144	30.17699	BLL	HSP	0.182	55.4	Cl
1FGL J1221.5+2814	W Com	185.38204	28.23292	BLL	LSP	0.102	1056	Cr	397.9	461.1	405
1FGL J1222.5+0415	4C+04.42	185.59396	4.22106	FSRQ	LSP	0.965	1022	Cr	1085	1254	1127
1FGL J1224.8+8044	CRATES J1223+8040	185.91875	80.66786	BLL	LSP	...	432.4	Cr
1FGL J1224.7+2121	4C+21.35	186.22692	21.37955	FSRQ	LSP	0.435	1074	Cr
1FGL J1226.8+0638	BZB J1226+0638	186.68428	6.64811	BLL	HSP	...	11.6	F
1FGL J1226.7–1332	CGRaBS J1226–1328	186.72675	−13.47753	BLL	...	0.456	185.2	Cr	76.05	237.4	88.5
1FGL J1228.2+4855	CRATES J1228+4858	187.21571	48.96703	FSRQ	LSP	1.722	265.5	Cr
1FGL J1229.1+0203	3C 273	187.27792	2.05239	FSRQ	LSP	0.158	41 720	Cr	27 750	29 860	27 730
1FGL J1230.4+2520	ON 246	187.55871	25.30197	BLL	LSP	0.135	326.4	Cr	222.7	325.9	264.3
1FGL J1230.8+1223	M 87	187.70593	12.39112	AGN	LSP	0.004	2 640	N01
1FGL J1231.6+2850	B2 1229+29	187.93158	28.79717	BLL	HSP	0.236	56.9	Cr
1FGL J1233.6–0146	BZB J1233–0144	188.42221	−1.73993	BLL	28	N
1FGL J1239.5+0443	CRATES J1239+0443	189.88650	4.71811	FSRQ	...	1.761	290.7	Cr
1FGL J1243.1+3627	B2 1240+36	190.80308	36.46222	BLL	HSP	...	53.9	Cr
1FGL J1246.7–2545	PKS 1244–255	191.69500	−25.79703	FSRQ	LSP	0.633	1864	Cr
1FGL J1248.2+5820	CGRaBS J1248+5820	192.07825	58.34130	BLL	LSP	...	324.4	Cr	160.4	249.8	146.8
1FGL J1253.7+0326	CRATES J1253+0326	193.44588	3.44178	BLL	HSP	0.065	62.2	Cr
1FGL J1254.0+6236	BZB J1253+6242	193.49708	62.71600	BLL	HSP	...	12.7	F

Table 1—Continued

1FGL name	Other name	RA (°)	Dec (°)	Opt. type	SED type	z	S_8 (mJy)	Ref.	$S_{15, 1\text{yr mean}}$ (mJy)	$S_{15, 1\text{yr peak}}$ (mJy)	$S_{15, \text{non c.}}$ (mJy)
1FGL J1256.2–0547	3C 279	194.04654	−5.78931	FSRQ	LSP	0.536	25 850	Cr	15 360	17 660	11 360
1FGL J1256.5–1148	CRATES J1256–1146	194.06646	−11.77706	...	HSP	...	71.1	Cr
1FGL J1258.3+3227	B2 1255+32	194.48846	32.49148	FSRQ	LSP	0.806	477.1	Cr	621.5	779.6	444.8
1FGL J1258.4–1802	PKS B1256–177	194.65959	−18.00087	FSRQ	...	1.956	433.9	Cr
1FGL J1258.7–2221	PKS 1256–220	194.72700	−22.32531	FSRQ	...	1.303	780.8	Cr
1FGL J1303.0+2433	CRATES J1303+2433	195.76337	24.56547	BLL	135.7	Cr
1FGL J1304.0–4622	CGRaBS J1303–4621	195.91779	−46.35069	FSRQ	...	1.664	156.6	Cr
1FGL J1306.0+7852	CRATES J1305+7854	196.25008	78.90992	255.8	Cr
1FGL J1305.4–4928	NGC 4945	196.36446	−49.46806	AGN	LSP	0.002	1080	Cr
1FGL J1308.5+3550	CGRaBS J1308+3546	197.09879	35.77700	FSRQ	LSP	1.055	527	Cr	407.4	458.8	537.5
1FGL J1309.5+4304	B3 1307+433	197.35635	43.08489	BLL	ISP	...	31	Cl
1FGL J1309.2+1156	4C +12.46	197.39138	11.90683	BLL	LSP	...	785.1	Cr	566.1	706.8	526.6
1FGL J1310.6+3222	B2 1308+32	197.61942	32.34550	FSRQ	LSP	0.997	3032	Cr	1790	2184	2803
1FGL J1312.4–2156	CRATES J1312–2156	198.13150	−21.93983	BLL	151.5	Cr
1FGL J1312.4+4827	CGRaBS J1312+4828	198.18062	48.47525	FSRQ	...	0.501	250.3	Cr	130.5	240.6	120.4
1FGL J1314.7+2346	CRATES J1314+2348	198.68250	23.80742	BLL	ISP	...	158.2	Cr
1FGL J1316.1–3341	PKS 1313–333	199.03329	−33.64978	FSRQ	LSP	1.21	1165	Cr
1FGL J1317.8+3425	B2 1315+34A	199.40204	34.42108	FSRQ	LSP	1.05	541.3	Cr	415.7	473.9	401.9
1FGL J1321.1+2214	CGRaBS J1321+2216	200.29667	22.27003	FSRQ	...	0.943	323.6	Cr	236.4	622.2	391
1FGL J1321.3+8310	CRATES J1321+8316	200.43996	83.27039	275.4	Cr
1FGL J1322.7–0943	OP −034	200.65379	−9.62717	FSRQ	...	1.864	588.3	Cr	684.2	1585	380.1
1FGL J1325.6–4300	Cen A	201.36506	−43.01911	AGN	ISP	0.002	2950	T03
1FGL J1326.6+2213	B2 1324+22	201.75358	22.18061	FSRQ	LSP	1.4	984	Cr	912.2	1117	1282
1FGL J1331.0+5202	CGRaBS J1330+5202	202.67750	52.03761	AGN	...	0.688	171.9	Cr	150.1	204.9	156.6
1FGL J1331.9–0506	PKS 1329–049	203.01858	−5.16203	FSRQ	LSP	2.15	629.5	Cr	915.3	1292	1309
1FGL J1332.6–1255	CRATES J1332–1256	203.16354	−12.93758	FSRQ	...	1.498	150.6	Cr
1FGL J1332.9+4728	B3 1330+476	203.18850	47.37297	FSRQ	LSP	0.669	457.5	Cr	262.6	558.9	368.8
1FGL J1333.2+5056	CLASS J1333+5057	203.47409	50.95998	107.6	Cl
1FGL J1337.7–1255	PKS 1335–127	204.41575	−12.95686	FSRQ	LSP	0.539	4996	Cr	5976	6838	4254
1FGL J1338.9+1153	FRBA J1338+1153	204.74545	11.88822	BLL	11.8	Cl
1FGL J1340.6+4406	BZB J1340+4410	205.12414	44.16776	BLL	HSP	0.546	19.4	Cl
1FGL J1341.3+3951	BZB J1341+3959	205.27127	39.99595	BLL	HSP	0.172	39.3	N
1FGL J1344.2–1723	CGRaBS J1344–1723	206.06000	−17.39456	FSRQ	...	2.49	300.1	Cr	374.9	451.3	584.5
1FGL J1345.4+4453	B3 1343+451	206.38821	44.88322	FSRQ	LSP	2.534	255.6	Cr

Table 1—Continued

1FGL name	Other name	RA ($^{\circ}$)	Dec ($^{\circ}$)	Opt. type	SED type	z	S_8 (mJy)	Ref.	$S_{15, 1\text{yr mean}}$ (mJy)	$S_{15, 1\text{yr peak}}$ (mJy)	$S_{15, \text{non c.}}$ (mJy)
1FGL J1346.0+0703	CRATES J1345+0706	206.45546	7.10864	...	LSP	...	145.5	Cr
1FGL J1347.8−3751	CRATES J1347−3750	206.91846	−37.84350	FSRQ	LSP	1.3	83.7	Cr
1FGL J1351.0+3035	B2 1348+30B	207.71971	30.58156	FSRQ	LSP	0.714	671.7	Cr	317.4	1058	353.1
1FGL J1351.5+1115	BZB J1351+1114	207.83685	11.24804	BLL	HSP	...	29.2	Cl
1FGL J1353.3+1434	PKS 1350+148	208.34517	14.59425	BLL	177.1	Cr
1FGL J1354.9−1041	PKS 1352−104	208.69383	−10.68408	FSRQ	LSP	0.332	401.4	Cr
1FGL J1358.1+7646	CGRaBS J1357+7643	209.48071	76.72250	FSRQ	...	1.585	715.7	Cr	566.1	825.5	564
1FGL J1359.1+5539	CRATES J1359+5544	209.77392	55.74150	FSRQ	...	1.014	143.8	Cr
1FGL J1400.1−3743	CRATES J1359−3746	209.95717	−37.76689	BLL	73.9	Cr
1FGL J1407.5−4256	CGRaBS J1407−4302	211.91587	−43.04217	...	ISP	...	190.5	Cr
1FGL J1408.9−0751	PKS 1406−076	212.23534	−7.87407	FSRQ	LSP	1.494	953.3	Cr
1FGL J1417.8+2541	2E 1415+2557	214.48601	25.72346	BLL	HSP	0.237	34.3	F
1FGL J1418.3−0235	SDSS J141826.33−023334.1	214.60959	−2.55944	BLL	38.6	F
1FGL J1422.2+5757	1ES 1421+582	215.66206	58.03208	BLL	HSP	...	9.9	F
1FGL J1422.7+3743	CLASS J1423+3737	215.76921	37.62516	BLL	31.1	Cl
1FGL J1425.0+3614	CLASS J1424+3615	216.23131	36.26002	BLL	ISP	...	59.2	Cl
1FGL J1426.0+3403	BZB J1426+3404	216.53214	34.07397	BLL	ISP	...	25.1	Cl
1FGL J1426.9+2347	PKS 1424+240	216.75162	23.80000	BLL	HSP	...	241.6	Cr
1FGL J1428.2−4204	PKS 1424−41	216.98471	−42.10519	FSRQ	LSP	1.522	2443	Cr
1FGL J1428.7+4239	1ES 1426+428	217.13586	42.67252	BLL	HSP	0.129	27.4	Cl
1FGL J1433.9+4204	B3 1432+422	218.52375	42.05444	FSRQ	...	1.24	286.8	Cr	174.2	1947	136.1
1FGL J1436.9+2314	PKS 1434+235	219.17079	23.35092	FSRQ	...	1.545	650.7	Cr	629	761	826.5
1FGL J1437.0+5640	BZB J1436+5639	219.24051	56.65691	BLL	HSP	...	14.1	F
1FGL J1439.2+3930	PG 1437+398	219.82292	39.54500	BLL	HSP	0.349	45.7	F
1FGL J1440.9+0613	CRATES J1440+0610	220.22058	6.17117	BLL	ISP	...	36.5	Cr
1FGL J1442.1+4348	CLASS J1442+4348	220.52979	43.81020	BLL	18.9	Cl
1FGL J1442.8+1158	1ES 1440+122	220.70116	12.01122	BLL	HSP	0.163	31.2	Cl
1FGL J1443.8+2457	PKS 1441+25	220.98704	25.02903	FSRQ	LSP	0.939	229.4	Cr
1FGL J1444.0−3906	PKS 1440−389	220.98833	−39.14436	BLL	HSP	...	38.1	Cr
1FGL J1447.9+3608	RX J1448.0+3608	222.00250	36.14194	BLL	HSP	...	19.1	F
1FGL J1451.0+5204	CLASS J1450+5201	222.74995	52.01992	BLL	86.9	Cl
1FGL J1454.6+5125	CRATES J1454+5124	223.61300	51.40936	BLL	ISP	...	96.3	Cr
1FGL J1457.5−3540	PKS 1454−354	224.36129	−35.65278	FSRQ	LSP	1.424	628.9	Cr
1FGL J1501.1+2237	MS 14588+2249	225.25792	22.63500	BLL	HSP	0.235	62.5	F

Table 1—Continued

1FGL name	Other name	RA ($^{\circ}$)	Dec ($^{\circ}$)	Opt. type	SED type	z	S_8 (mJy)	Ref.	$S_{15, 1\text{yr mean}}$ (mJy)	$S_{15, 1\text{yr peak}}$ (mJy)	$S_{15, \text{non c.}}$ (mJy)
1FGL J1503.5–1544	BZB J1503–1541	225.91917	–15.68719	BLL	HSP	...	10.5	F
1FGL J1503.3+4759	CLASS J1503+4759	225.94999	47.99195	BLL	LSP	...	94.1	Cl
1FGL J1504.4+1029	PKS 1502+106	226.10408	10.49422	FSRQ	LSP	1.839	1687	Cr	2468	3308	1304
1FGL J1505.1–3435	CRATES J1505–3432	226.25987	–34.54903	71.8	Cr
1FGL J1505.0+0328	PKS 1502+036	226.27700	3.44189	AGN	LSP	0.409	847.6	Cr	555.1	654.5	543.9
1FGL J1505.8+3725	B2 1504+37	226.53971	37.51419	FSRQ	...	0.674	948.8	Cr	694.7	1736	632.8
1FGL J1511.1–0545	PKS 1508–05	227.72330	–5.71873	FSRQ	LSP	1.185	699.1	Cr
1FGL J1512.3+0201	PKS 1509+022	228.06560	2.05472	FSRQ	LSP	0.219	130	L97
1FGL J1512.8–0906	PKS 1510–08	228.21056	–9.09995	FSRQ	LSP	0.36	2630	Cr
1FGL J1514.7+4447	BZQ J1514+4450	228.65263	44.83447	FSRQ	LSP	0.57	47.4	Cl
1FGL J1516.9+1928	PKS 1514+197	229.23667	19.53695	BLL	609.3	Cr	1458	1746	995.9
1FGL J1517.8–2423	AP Lib	229.42421	–24.37208	BLL	ISP	0.048	2446	Cr
1FGL J1517.8+6530	BZB J1517+6525	229.44825	65.42313	BLL	HSP	0.702	36.2	Cl
1FGL J1519.7+4216	B3 1518+423	230.16550	42.18653	FSRQ	...	0.484	56.5	Cr
1FGL J1522.1+3143	B2 1520+31	230.54163	31.73733	FSRQ	LSP	1.487	493.8	Cr	426.3	465.8	505.8
1FGL J1522.6–2732	PKS 1519–273	230.65700	–27.50300	BLL	LSP	1.294	1538	Cr
1FGL J1531.8+3018	BZU J1532+3016	233.00929	30.27468	BLL	HSP	0.065	43.8	Cl
1FGL J1536.6+8200	CLASS J1537+8154	234.25036	81.90862	174.9	Cl
1FGL J1539.7+2747	CGRaBS J1539+2744	234.91308	27.74397	FSRQ	...	2.19	291.5	Cr	256.1	423.4	230.2
1FGL J1542.9+6129	CRATES J1542+6129	235.73729	61.49872	BLL	ISP	...	144	Cr
1FGL J1548.7–2250	CRATES J1548–2251	237.20729	–22.85069	BLL	HSP	...	106.7	Cr
1FGL J1549.3+0235	PKS 1546+027	237.37267	2.61700	FSRQ	LSP	0.414	918.7	Cr	1866	2641	1671
1FGL J1550.7+0527	4C +05.64	237.64696	5.45292	FSRQ	LSP	1.422	1615	Cr	2795	3012	2887
1FGL J1553.4–2425	PKS 1550–242	238.38462	–24.36756	240.6	Cr
1FGL J1553.4+1255	PKS 1551+130	238.38625	12.94769	FSRQ	...	1.308	412.4	Cr
1FGL J1555.7+1111	PG 1553+113	238.92933	11.19011	BLL	HSP	...	506.5	Cr	181.2	209.1	142.5
1FGL J1558.9+5627	CRATES J1558+5625	239.70121	56.42058	BLL	LSP	0.3	169.7	Cr
1FGL J1604.3+5710	CGRaBS J1604+5714	241.15567	57.24353	FSRQ	LSP	0.72	485.3	Cr	525.4	620.3	368
1FGL J1607.1+1552	4C +15.54	241.77679	15.85958	AGN	LSP	0.496	286.9	Cr
1FGL J1609.0+1031	4C +10.45	242.19250	10.48550	FSRQ	LSP	1.226	1756	Cr	1163	1471	785.1
1FGL J1610.6–6649	CRATES J1610–6649	242.69333	–66.81702	BLL	HSP	...	73.1	Cr
1FGL J1613.5+3411	B2 1611+34	243.42108	34.21331	FSRQ	LSP	1.397	3088	Cr	2919	3086	2327
1FGL J1616.1+4637	CRATES J1616+4632	244.01571	46.54033	FSRQ	...	0.95	125.5	Cr
1FGL J1617.9–7716	PKS 1610–77	244.45583	–77.28844	FSRQ	LSP	1.71	2378	Cr

Table 1—Continued

1FGL name	Other name	RA (°)	Dec (°)	Opt. type	SED type	z	S_8 (mJy)	Ref.	$S_{15, 1\text{yr mean}}$ (mJy)	$S_{15, 1\text{yr peak}}$ (mJy)	$S_{15, \text{non c.}}$ (mJy)
1FGL J1624.7−0642	4C −06.46	246.13717	−6.83047	253.4	Cr
1FGL J1625.7−2524	PKS 1622−253	246.44538	−25.46064	FSRQ	LSP	0.786	2391	Cr
1FGL J1626.2−2956	PKS 1622−29	246.52509	−29.85749	FSRQ	LSP	0.815	3550	Cr
1FGL J1630.2+5220	CRATES J1630+5221	247.67979	52.36072	BLL	ISP	...	37.9	Cr
1FGL J1635.4+8228	NGC 6251	248.13325	82.53789	AGN	ISP	0.025	738.4	Cr	872.8	939.2	890.5
1FGL J1635.0+3808	4C +38.41	248.81454	38.13458	FSRQ	LSP	1.814	2404	Cr	2751	2883	3864
1FGL J1641.0+1143	CRATES J1640+1144	250.24537	11.73450	AGN	...	0.078	178	Cr
1FGL J1647.4+4948	CGRaBS J1647+4950	251.89546	49.83350	AGN	ISP	0.047	232.3	Cr	245.2	267.4	253.7
1FGL J1653.9+3945	Mkn 501	253.46758	39.76017	BLL	HSP	0.034	1158	Cr	1149	1203	1158
1FGL J1656.9+6017	CRATES J1656+6012	254.20104	60.20458	FSRQ	LSP	0.623	226.5	Cr
1FGL J1700.1+6830	CGRaBS J1700+6830	255.03875	68.50195	FSRQ	LSP	0.301	383.5	Cr	290.3	333	436.4
1FGL J1709.6+4320	B3 1708+433	257.42121	43.31236	FSRQ	LSP	1.027	197.2	Cr	251.7	354.8	322.8
1FGL J1719.2+1745	PKS 1717+177	259.80437	17.75178	BLL	LSP	0.137	579.9	Cr	588.2	655.7	707.1
1FGL J1722.5+1012	CRATES J1722+1013	260.68575	10.22661	FSRQ	LSP	0.732	191.2	Cr
1FGL J1724.0+4002	B2 1722+40	261.02263	40.07681	AGN	...	1.049	296.1	Cr
1FGL J1725.0+1151	CGRaBS J1725+1152	261.26808	11.87097	BLL	HSP	...	198	Cr	63.28	93.38	68.97
1FGL J1725.5+5854	BZB J1725+5851	261.39593	58.86111	BLL	ISP	...	49.7	Cl
1FGL J1727.3+4525	B3 1726+455	261.86521	45.51103	FSRQ	LSP	0.714	1360	Cr	1248	1556	1970
1FGL J1728.2+0431	PKS 1725+044	262.10396	4.45136	FSRQ	LSP	0.293	622	Cr	672	1161	1068
1FGL J1730.4+0008	PKS 1728+004	262.64583	0.41075	FSRQ	...	1.335	123.4	Cr
1FGL J1730.8+3716	CRATES J1730+3714	262.69604	37.24864	BLL	ISP	...	68.7	Cr
1FGL J1733.0−1308	PKS 1730−13	263.26129	−13.08042	FSRQ	LSP	0.902	5389	Cr	4649	4960	3885
1FGL J1734.4+3859	B2 1732+38A	263.58575	38.96428	FSRQ	LSP	0.976	1160	Cr	866.1	1165	945.7
1FGL J1735.4−1118	CRATES J1735−1117	263.86325	−11.29292	62	Cr
1FGL J1742.1+5947	CRATES J1742+5945	265.63338	59.75186	BLL	ISP	...	116.2	Cr
1FGL J1744.2+1934	1ES 1741+196	265.99096	19.58583	BLL	HSP	0.083	170.4	Cr
1FGL J1745.6−0751	CGRaBS J1745−0753	266.36292	−7.88439	BLL	LSP	...	931.5	Cr	639.6	710.3	628.5
1FGL J1748.5+7004	CGRaBS J1748+7005	267.13683	70.09744	BLL	ISP	0.77	572.8	Cr	506.9	558.5	536.9
1FGL J1749.0+4323	B3 1747+433	267.25150	43.36425	BLL	LSP	...	284.9	Cr	391.7	428.9	443.6
1FGL J1751.5+0937	4C +09.57	267.88675	9.65019	BLL	LSP	0.322	2015	Cr	5337	7380	4420
1FGL J1800.4+7827	CGRaBS J1800+7828	270.19033	78.46778	BLL	LSP	0.68	2874	Cr	2523	3142	2628
1FGL J1804.1+0336	CRATES J1803+0341	270.98450	3.68544	FSRQ	...	1.42	104.3	Cr
1FGL J1807.0+6945	3C 371	271.71117	69.82447	BLL	LSP	0.051	1596	Cr	1627	1802	1551
1FGL J1809.6+2908	CRATES J1809+2910	272.43912	29.17219	BLL	52.6	Cr

Table 1—Continued

1FGL name	Other name	RA ($^{\circ}$)	Dec ($^{\circ}$)	Opt. type	SED type	z	S_8 (mJy)	Ref.	$S_{15, 1\text{yr mean}}$ (mJy)	$S_{15, 1\text{yr peak}}$ (mJy)	$S_{15, \text{non c.}}$ (mJy)
1FGL J1813.4+3141	B2 1811+31	273.39671	31.73822	BLL	ISP	0.117	92	Cr
1FGL J1818.1+0905	CRATES J1818+0903	274.66692	9.06283	FSRQ	...	0.354	120.6	Cr
1FGL J1824.0+5651	4C +56.27	276.02946	56.85042	BLL	LSP	...	1193	Cr	1563	1741	1619
1FGL J1829.8+5404	BZB J1829+5402	277.35121	54.04994	BLL	HSP	...	18	N
1FGL J1829.8+4845	3C 380	277.38242	48.74616	AGN	LSP	0.692	2854	A95
1FGL J1832.6−5700	CRATES J1832−5659	278.12946	−56.98856	BLL	154.6	Cr
1FGL J1838.6+4756	BZB J1838+4802	279.70485	48.04285	BLL	HSP	...	32.7	Cl
1FGL J1848.5+3224	B2 1846+32A	282.09208	32.31739	FSRQ	LSP	0.798	640.5	Cr	591.8	733.3	401.7
1FGL J1849.3+6705	CGRaBS J1849+6705	282.31700	67.09492	FSRQ	LSP	0.657	476	Cr	2354	2950	2024
1FGL J1849.6−4314	CRATES J1849−4314	282.35783	−43.23697	BLL	104.7	Cr
1FGL J1852.5+4853	CGRaBS J1852+4855	283.11896	48.92986	FSRQ	LSP	1.25	374.1	Cr	358	471.8	574.7
1FGL J1902.3−6802	CGRaBS J1903−6749	285.75513	−67.82655	FSRQ	...	0.255	359.7	Cr
1FGL J1903.0+5539	CRATES J1903+5540	285.79838	55.67733	BLL	ISP	...	166.3	Cr
1FGL J1911.2−2007	PKS B1908−201	287.79021	−20.11530	FSRQ	LSP	1.119	3013	Cr
1FGL J1917.7−1922	CGRaBS J1917−1921	289.43675	−19.35878	BLL	ISP	0.137	322.2	Cr	337.8	537.3	293.5
1FGL J1918.4−4108	CRATES J1918−4111	289.56738	−41.19192	BLL	189.8	Cr
1FGL J1921.1−1234	CRATES J1921−1231	290.34967	−12.53178	96.1	Cr
1FGL J1922.0−1608	CRATES J1921−1607	290.46471	−16.12017	BLL	84	Cr
1FGL J1923.5−2104	OV −235	290.88412	−21.07594	FSRQ	LSP	0.874	2740	Cr
1FGL J1925.2−2919	PKS B1921−293	291.21275	−29.24169	FSRQ	LSP	0.352	14 820	Cr
1FGL J1925.1−1018	CRATES J1925−1018	291.26333	−10.30344	BLL	99.4	Cr
1FGL J1936.9−4720	BZB J1936−4719	294.23375	−47.33056	BLL	HSP	0.265	53.5	N
1FGL J1941.6+7214	CRATES J1941+7221	295.36242	72.36172	165.2	Cr
1FGL J1946.1−3118	PKS 1942−313	296.49737	−31.19397	BLL	154.8	Cr
1FGL J1954.8−1124	CGRaBS J1954−1123	298.67146	−11.38964	FSRQ	...	0.683	404.6	Cr	428.2	599.7	451.3
1FGL J1958.4−3847	PKS 1954−388	299.49925	−38.75178	FSRQ	LSP	0.63	2825	Cr
1FGL J1959.3−4241	CGRaBS J1959−4246	299.80579	−42.76886	FSRQ	...	2.174	269.3	Cr
1FGL J2000.0+6508	1ES 1959+650	299.99937	65.14853	BLL	HSP	0.049	222.8	Cr	215.6	315.6	193.2
1FGL J2000.9−1749	PKS 1958−179	300.23787	−17.81603	FSRQ	LSP	0.652	2144	Cr	2011	3267	1660
1FGL J2001.9+7040	CRATES J2001+7040	300.39146	70.67384	61.1	Cr
1FGL J2006.0+7751	CGRaBS J2005+7752	301.37917	77.87867	BLL	LSP	0.342	2675	Cr	982.4	1149	1579
1FGL J2006.6−2302	CRATES J2005−2310	301.48579	−23.17417	FSRQ	LSP	0.833	193.3	Cr
1FGL J2007.9−4430	PKS 2004−447	301.97992	−44.57900	AGN	LSP	0.24	300.7	Cr
1FGL J2008.6−0419	3C 407	302.10161	−4.30814	AGN	...	0.589	127.8	Cr

Table 1—Continued

1FGL name	Other name	RA ($^{\circ}$)	Dec ($^{\circ}$)	Opt. type	SED type	z	S_8 (mJy)	Ref.	$S_{15, 1\text{yr mean}}$ (mJy)	$S_{15, 1\text{yr peak}}$ (mJy)	$S_{15, \text{non c.}}$ (mJy)
1FGL J2009.5–4849	PKS 2005–489	302.35579	–48.83128	BLL	HSP	0.071	874.1	Cr
1FGL J2009.1+7228	4C +72.28	302.46792	72.48872	BLL	LSP	...	791.9	Cr	712.9	991.1	935.9
1FGL J2015.3–0129	PKS 2012–017	303.81317	–1.62569	BLL	585.3	Cr
1FGL J2020.4+7608	CGRaBS J2022+7611	305.64829	76.19061	BLL	400	Cr	514.6	1365	647.3
1FGL J2023.7–1141	CRATES J2023–1139	305.90292	–11.66619	FSRQ	...	0.698	92.1	Cr
1FGL J2025.6–0735	PKS 2023–07	306.41942	–7.59797	FSRQ	LSP	1.388	754.5	Cr
1FGL J2025.9–2852	CGRaBS J2025–2845	306.47337	–28.76353	...	LSP	...	527.7	Cr
1FGL J2030.3–0617	CRATES J2030–0622	307.56304	–6.37083	FSRQ	...	0.667	137	Cr
1FGL J2031.5+1219	PKS 2029+121	307.97917	12.32814	BLL	1098	Cr	1380	1709	1774
1FGL J2035.4+1100	PKS 2032+107	308.84308	10.93522	FSRQ	LSP	0.601	463.4	Cr
1FGL J2039.0–1047	CRATES J2039–1046	309.75292	–10.77831	BLL	129.6	Cr
1FGL J2050.1+0407	PKS 2047+039	312.52600	4.13025	BLL	452.5	Cr	554.5	1067	541.1
1FGL J2055.5–0023	SDSS J205528.20–002117.2	313.86749	–0.35472	BLL	HSP	...	22.4	F
1FGL J2056.3–4714	PKS 2052–47	314.06862	–47.24650	FSRQ	LSP	1.489	1534	Cr
1FGL J2103.9–6237	CRATES J2103–6232	315.90975	–62.54072	...	HSP	...	79.3	Cr
1FGL J2108.5–0249	CRATES J2108–0250	317.18637	–2.84286	86.2	Cr
1FGL J2108.6–6646	PKS 2104–668	317.21612	–66.62302	...	LSP	...	126.1	Cr
1FGL J2110.0+0811	CRATES J2110+0809	317.54033	8.16539	FSRQ	...	1.58	66.1	Cr
1FGL J2115.5+2937	B2 2113+29	318.87258	29.56067	FSRQ	LSP	1.514	888.7	Cr	831	1067	664.3
1FGL J2116.1+3338	B2 2114+33	319.06050	33.65567	BLL	ISP	...	98.5	Cr
1FGL J2117.8+0016	CRATES J2118+0013	319.57250	0.22133	FSRQ	...	0.463	94.7	Cr
1FGL J2120.9+1901	OX 131	320.25254	19.02453	FSRQ	LSP	2.18	290.3	Cr
1FGL J2126.1–4603	PKS 2123–463	321.62846	–46.09633	FSRQ	...	1.67	470.7	Cr
1FGL J2131.7–0914	RBS 1752	322.89792	–9.25611	BLL	HSP	0.449	30.3	F
1FGL J2134.0–0203	4C –02.81	323.54296	–1.88811	FSRQ	LSP	1.284	1709	Cr	2312	2471	2615
1FGL J2135.8–4957	CRATES J2135–5006	323.83371	–50.11395	FSRQ	...	2.181	236.1	Cr
1FGL J2139.3–4235	CRATES J2139–4235	324.85071	–42.58905	BLL	ISP	...	95.4	Cr
1FGL J2143.1–3927	CRATES J2143–3929	325.76192	–39.49022	BLL	35.6	Cr
1FGL J2143.4+1742	OX 169	325.89808	17.73019	FSRQ	LSP	0.211	613.8	Cr	815.7	1134	821.7
1FGL J2145.4–3358	CGRaBS J2145–3357	326.25471	–33.95456	FSRQ	...	1.36	212.5	Cr
1FGL J2147.2+0929	PKS 2144+092	326.79237	9.49631	FSRQ	LSP	1.113	1002	Cr	912.7	1272	861.4
1FGL J2148.5+0654	4C +06.69	327.02275	6.96072	FSRQ	LSP	0.999	7027	Cr	5544	5811	5379
1FGL J2149.7+0327	PKS B2147+031	327.42446	3.38094	BLL	79.6	Cr
1FGL J2150.3–1410	BZB J2150–1410	327.56458	–14.18058	BLL	HSP	0.229	24	F

Table 1—Continued

1FGL name	Other name	RA ($^{\circ}$)	Dec ($^{\circ}$)	Opt. type	SED type	z	S_8 (mJy)	Ref.	$S_{15, 1\text{yr mean}}$ (mJy)	$S_{15, 1\text{yr peak}}$ (mJy)	$S_{15, \text{non c.}}$ (mJy)
1FGL J2152.5+1734	PKS 2149+17	328.10342	17.57717	BLL	LSP	0.871	628.4	Cr	496.3	564.9	480.3
1FGL J2157.4+3129	B2 2155+31	329.37008	31.45039	FSRQ	LSP	1.486	490	Cr	545.8	771.9	606.5
1FGL J2157.9–1503	PKS 2155–152	329.52617	–15.01925	FSRQ	LSP	0.672	2207	Cr	1579	1767	1781
1FGL J2158.8–3013	PKS 2155–304	329.71696	–30.22558	BLL	HSP	0.116	355.5	Cr
1FGL J2201.6–8327	PKS 2155–83	330.58221	–83.63653	FSRQ	...	1.865	487.3	Cr
1FGL J2202.8+4216	BL Lac	330.68038	42.27777	BLL	LSP	0.069	3322	Cl
1FGL J2203.5+1726	PKS 2201+171	330.86204	17.43008	FSRQ	LSP	1.076	1089	Cr	1100	1407	968.3
1FGL J2204.6+0442	4C+04.77	331.07358	4.66722	AGN	ISP	0.027	333.8	Cr
1FGL J2207.8–5344	PKS 2204–54	331.93175	–53.77642	FSRQ	LSP	1.206	1158	Cr
1FGL J2212.1+2358	PKS 2209+236	333.02488	23.92794	FSRQ	LSP	1.125	719.6	Cr	924.4	1148	908.6
1FGL J2213.1–2529	PKS 2210–25	333.26042	–25.49169	FSRQ	...	1.831	449.7	Cr
1FGL J2217.1+2423	B2 2214+24B	334.25346	24.36278	BLL	LSP	0.505	583.7	Cr	821.4	1452	625.3
1FGL J2219.3+1804	CGRaBS J2219+1806	334.80871	18.10989	FSRQ	...	1.071	377.9	Cr	235.2	766.8	182.6
1FGL J2222.5–5218	BZB J2221–5225	335.37242	–52.42375	BLL	HSP	...	52.5	N
1FGL J2225.8–0457	3C 446	336.44692	–4.95039	FSRQ	LSP	1.404	4204	Cr
1FGL J2229.7–0832	PKS 2227–08	337.41700	–8.54844	FSRQ	LSP	1.559	1227	Cr	2697	3197	1742
1FGL J2232.5+1144	CTA 102	338.15171	11.73080	FSRQ	LSP	1.037	2924	Cl
1FGL J2235.7–4817	PKS 2232–488	338.80517	–48.59969	FSRQ	LSP	0.51	904.1	Cr
1FGL J2236.2+2828	B2 2234+28A	339.09362	28.48261	FSRQ	LSP	0.795	1742	Cr	1271	1533	1294
1FGL J2236.4–1432	PKS 2233–148	339.14204	–14.55617	BLL	LSP	...	468.2	Cr	411.6	587	582.4
1FGL J2237.2–3919	CRATES J2237–3921	339.28379	–39.36061	FSRQ	...	0.297	163.5	Cr
1FGL J2243.1–2541	PKS 2240–260	340.85983	–25.74083	BLL	LSP	0.774	711.6	Cr
1FGL J2244.0+2021	CRATES J2243+2021	340.97808	20.35106	BLL	HSP	...	106.4	Cr
1FGL J2247.3+0000	PKS 2244–002	341.87583	0.00167	BLL	215.6	Cr
1FGL J2250.1+3825	B3 2247+381	342.52396	38.41033	BLL	HSP	0.119	61.1	Cr
1FGL J2250.8–2809	CGRaBS J2250–2806	342.68521	–28.10981	AGN	LSP	0.525	316.6	Cr
1FGL J2251.7+4030	CRATES J2251+4030	342.99904	40.51617	BLL	137.9	Cr
1FGL J2253.9+1608	3C 454.3	343.49063	16.14822	FSRQ	LSP	0.859	10 380	Cr	10 920	14 650	12 850
1FGL J2256.3–2009	PKS 2254–204	344.17171	–20.19456	BLL	400.2	Cr
1FGL J2258.9–5525	BZB J2258–5525	344.57921	–55.42681	BLL	HSP	0.479	42.5	N
1FGL J2304.3+3709	FRBA J2304+3705	346.15250	37.08556	BLL	HSP	...	19.1	F
1FGL J2307.3+1452	CGRaBS J2307+1450	346.89167	14.83833	BLL	239.7	Cr	71.29	135.6	126.2
1FGL J2311.0+3425	B2 2308+34	347.77221	34.41969	FSRQ	LSP	1.817	638.5	Cr
1FGL J2314.1+1444	BZU J2313+1444	348.48899	14.73994	...	HSP	...	25.9	F

Table 1—Continued

1FGL name	Other name	RA (°)	Dec (°)	Opt. type	SED type	z	S_8 (mJy)	Ref.	$S_{15, 1\text{yr mean}}$ (mJy)	$S_{15, 1\text{yr peak}}$ (mJy)	$S_{15, \text{non c.}}$ (mJy)
1FGL J2315.9–5014	PKS 2312–505	348.93458	–50.31108	BLL	563.8	Cr
1FGL J2322.0+3208	B2 2319+31	350.47896	32.06878	FSRQ	LSP	1.489	180.4	Cr
1FGL J2321.6+2726	4C +27.50	350.49942	27.54622	FSRQ	LSP	1.253	505.9	Cr
1FGL J2322.6+3435	CRATES J2322+3436	350.68338	34.60386	BLL	HSP	0.098	38	Cr
1FGL J2322.3–0153	PKS 2320–021	350.76929	–1.84669	FSRQ	...	1.774	241.8	Cr
1FGL J2323.5–0315	PKS 2320–035	350.88313	–3.28472	FSRQ	LSP	1.41	761.9	Cr	1079	1291	914.7
1FGL J2323.5+4211	1ES 2321+419	350.96707	42.18297	BLL	HSP	...	20.7	F
1FGL J2325.2+3957	B3 2322+396	351.32446	39.96014	BLL	LSP	...	115.5	Cr
1FGL J2325.6–4758	PKS 2322–482	351.36250	–48.00467	BLL	ISP	0.221	197	Cr
1FGL J2325.5–3559	CTS A13.10	351.36917	–35.96500	FSRQ	...	0.36	49.4	F
1FGL J2327.7+0943	PKS 2325+093	351.88992	9.66931	FSRQ	LSP	1.843	652.7	Cr	2110	2800	1446
1FGL J2329.2–4954	PKS 2326–502	352.33692	–49.92803	FSRQ	...	0.518	427.7	Cr
1FGL J2331.0–2145	CRATES J2331–2148	352.76679	–21.80428	FSRQ	...	0.556	57.2	Cr
1FGL J2334.3+0735	CGRaBS J2334+0736	353.55342	7.60764	FSRQ	ISP	0.401	922.2	Cr	1149	1475	904.9
1FGL J2334.7+1429	BZB J2334+1408	353.72432	14.53743	BLL	43.4	Cl
1FGL J2338.3–0231	PKS 2335–027	354.48892	–2.51600	FSRQ	...	1.072	570	Cr	644.6	711.6	760.6
1FGL J2339.0+2123	BZB J2338+2124	354.73495	21.41147	BLL	HSP	0.291	38.2	Cl
1FGL J2341.6+8015	FRBA J2340+8015	355.22616	80.25447	BLL	HSP	0.274	42.5	F
1FGL J2344.6–1554	CGRaBS J2345–1555	356.30192	–15.91883	FSRQ	LSP	0.621	462	Cr	520.6	685.4	613.5
1FGL J2348.0–1629	PKS 2345–16	357.01087	–16.52000	FSRQ	LSP	0.576	2240	Cr	2037	2314	1996
1FGL J2359.0–3035	1H 2351–315	359.78250	–30.62750	BLL	HSP	0.165	34.2	F

Note. — The optical data reported in this table are taken directly from the 1LAC (Abdo et al. 2010d) and have been used in the data shuffling. We note that the measure of z for a few sources has improved (e.g. PG 1553+113, Danforth et al. 2010) and that for local sources (e.g. Cen A) the redshift information does not necessarily provide the most accurate estimate of the actual distance.

References. — Cr: CRATES (Healey et al. 2007); Cl: CLASS (Myers et al. 2003; Browne et al. 2003); F: FRBA (Finding and Rejecting Blazar Associations for Fermi-LAT gamma-ray sources, from 8.4 GHz VLA program AH996); N: data extrapolated from NED/NVSS/Bzcat; A95: Akujor & Garrington (1995); L97: Laurent-Muehleisen et al. (1997); N01: Nagar et al. (2001, $S_8 = 2.92$ Jy used in the calculation); T03: Tingay et al. (2003, $S_8 = 4.99$ Jy and $S_8 = 2.95$ Jy used in the calculation for 1FGL J0522.8–3632 and 1FGL J1325.6–4300, respectively); U84: Unger et al. (1984).

Table 2. Spearman rank correlation coefficient ρ for the 1LAC clean sample, divided by source type. For each energy band (E measured in GeV), the number of significant sources n and the correlation coefficient ρ are given.

Source class	$E > 0.1$		$0.1 < E < 0.3$		$0.3 < E < 1$		$1 < E < 3$		$3 < E < 10$		$10 < E < 100$	
	n	ρ	n	ρ	n	ρ	n	ρ	n	ρ	n	ρ
All sources	599	0.43	193	0.41	384	0.51	493	0.43	373	0.31	127	0.30
FSRQ	248	0.39	128	0.32	214	0.41	220	0.35	140	0.29	22	0.42
BL Lacs	275	0.46	47	0.48	135	0.54	214	0.54	197	0.35	99	0.31
LSP	242	0.40	133	0.37	200	0.42	219	0.38	158	0.39	35	0.35
ISP	60	0.33	18	0.58	41	0.40	53	0.44	42	0.29	15	0.30
HSP	129	0.55	12	0.16	47	0.62	87	0.64	88	0.57	64	0.55

Table 3. Spearman rank correlation coefficient ρ for the subset of the 1LAC clean sample monitored by OVRO, divided by source type. For each energy band (E measured in GeV), the number of significant sources n and the correlation coefficient ρ are given.

Source class	$E > 0.1$		$0.1 < E < 0.3$		$0.3 < E < 1$		$1 < E < 3$		$3 < E < 10$		$10 < E < 100$	
	n	ρ	n	ρ	n	ρ	n	ρ	n	ρ	n	ρ
8 GHz non simultaneous radio data												
All sources	199	0.27	97	0.40	163	0.41	179	0.25	134	0.15	40	−0.04
FSRQ	120	0.38	67	0.36	104	0.41	109	0.36	73	0.27	13	0.38
BL Lacs	69	0.08	24	0.30	51	0.28	61	0.14	57	0.03	25	−0.19
LSP	131	0.30	77	0.42	113	0.41	120	0.29	89	0.28	24	0.16
ISP	17	0.07	6	0.09	16	0.37	16	0.09	13	−0.19	4	0.00
HSP	10	0.73	6	−0.02	10	0.64	10	0.79	10	0.67	9	0.67
15 GHz concurrent radio data, 1-yr mean values												
All sources	199	0.35	97	0.56	163	0.47	179	0.35	134	0.17	40	−0.02
FSRQ	120	0.48	67	0.56	104	0.54	109	0.49	73	0.35	13	0.57
BL Lacs	69	0.13	24	0.41	51	0.22	61	0.14	57	0.00	25	−0.23
LSP	131	0.42	77	0.60	113	0.53	120	0.44	89	0.30	24	0.26
ISP	17	0.29	6	0.66	16	0.54	16	0.29	13	0.20	4	0.40
HSP	10	0.58	6	−0.02	10	0.56	10	0.65	10	0.48	9	0.50
15 GHz concurrent radio data, 1-yr peak values												
All sources	199	0.28	97	0.56	163	0.41	179	0.27	134	0.11	40	−0.06
FSRQ	120	0.43	67	0.55	104	0.51	109	0.41	73	0.31	13	0.59
BL Lacs	69	−0.01	24	0.42	51	0.11	61	0.06	57	−0.07	25	−0.35
LSP	131	0.42	77	0.60	113	0.52	120	0.43	89	0.30	24	0.30
ISP	17	0.28	6	0.66	16	0.45	16	0.36	13	0.18	4	0.40
HSP	10	0.13	6	0.09	10	0.16	10	0.16	10	0.12	9	0.08
15 GHz non concurrent radio data, 9-days mean values												
All sources	199	0.33	97	0.48	163	0.42	179	0.31	134	0.16	40	−0.06
FSRQ	120	0.45	67	0.49	104	0.51	109	0.47	73	0.35	13	0.34
BL Lacs	69	0.13	24	0.24	51	0.15	61	0.11	57	0.01	25	−0.20
LSP	131	0.40	77	0.51	113	0.46	120	0.39	89	0.29	24	0.12
ISP	17	0.12	6	0.43	16	0.31	16	0.06	13	0.10	4	0.80
HSP	10	0.37	6	0.09	10	0.53	10	0.39	10	0.24	9	0.32

Table 4. Spearman rank correlation coefficient ρ for 1LAC sources with a detection in at least 4 energy bands, divided by source type. For each energy band (E measured in GeV), the number of significant sources n and the correlation coefficient ρ are given.

Source class	$E > 0.1$		$0.1 < E < 0.3$		$0.3 < E < 1$		$1 < E < 3$		$3 < E < 10$		$10 < E < 100$	
	n	ρ	n	ρ	n	ρ	n	ρ	n	ρ	n	ρ
All sources	192	0.45	149	0.45	192	0.60	192	0.44	192	0.15	94	0.21
FSRQ	94	0.30	93	0.34	94	0.30	94	0.24	94	0.15	22	0.42
BL Lacs	84	0.55	44	0.48	84	0.72	84	0.62	84	0.41	67	0.23
LSP	107	0.40	102	0.42	107	0.39	107	0.33	107	0.24	33	0.29
ISP	20	0.46	15	0.52	20	0.63	20	0.26	20	0.16	12	0.02
HSP	41	0.71	12	0.16	41	0.65	41	0.74	41	0.64	40	0.64

Table 5. Significances of intrinsic correlations after common-distance effects are taken into account, for sources with known redshift, using 8 GHz archival data, as a function of source type and γ -ray energy band.

Source type	Energy Band	Number of sources	Number of z-bins	Spearman ρ	Pearson r	significance
All sources	$E > 0.1$	390	10	0.46	0.47	$< 10^{-7}$
	$0.1 < E < 0.3$	164	10	0.36	0.42	3.4×10^{-5}
	$0.3 < E < 1$	281	10	0.45	0.48	$< 10^{-7}$
	$1 < E < 3$	329	10	0.42	0.44	$< 10^{-7}$
	$3 < E < 10$	235	10	0.34	0.36	8.1×10^{-6}
	$10 < E < 100$	72	5	0.34	0.37	0.046
FSRQ	$E > 0.1$	248	10	0.39	0.42	$< 10^{-7}$
	$0.1 < E < 0.3$	128	10	0.32	0.40	1.13×10^{-4}
	$0.3 < E < 1$	214	10	0.41	0.44	$< 10^{-7}$
	$1 < E < 3$	220	10	0.35	0.38	1.0×10^{-7}
	$3 < E < 10$	140	10	0.29	0.33	5.7×10^{-4}
	$10 < E < 100$	22	2	0.42	0.39	0.084
BL Lacs	$E > 0.1$	116	10	0.63	0.62	$< 10^{-7}$
	$0.1 < E < 0.3$	27	3	0.42	0.43	0.034
	$0.3 < E < 1$	54	5	0.58	0.57	1.5×10^{-4}
	$1 < E < 3$	88	10	0.66	0.62	1.9×10^{-6}
	$3 < E < 10$	83	10	0.45	0.46	2.5×10^{-3}
	$10 < E < 100$	49	5	0.43	0.39	0.26
LSP	$E > 0.1$	209	10	0.38	0.42	1.3×10^{-6}
	$0.1 < E < 0.3$	123	10	0.37	0.43	1.8×10^{-4}
	$0.3 < E < 1$	181	10	0.42	0.46	1.8×10^{-7}
	$1 < E < 3$	192	10	0.37	0.41	2.0×10^{-6}
	$3 < E < 10$	134	10	0.39	0.41	7.5×10^{-4}
	$10 < E < 100$	29	2	0.28	0.40	0.077
ISP	$E > 0.1$	26	2	0.49	0.52	0.01
	$0.1 < E < 0.3$	9	1	0.62	0.55	0.13
	$0.3 < E < 1$	19	2	0.59	0.58	0.033
	$1 < E < 3$	22	2	0.45	0.44	0.082
	$3 < E < 10$	17	1	0.02	0.12	0.65
	$10 < E < 100$		– Not enough sources with redshift –			
HSP	$E > 0.1$	73	7	0.49	0.68	3.0×10^{-7}
	$0.1 < E < 0.3$	9	1	0.15	0.003	0.99
	$0.3 < E < 1$	21	2	0.64	0.62	0.02
	$1 < E < 3$	48	4	0.66	0.74	7.0×10^{-7}
	$3 < E < 10$	45	5	0.56	0.70	2.6×10^{-4}
	$10 < E < 100$	35	3	0.59	0.71	5.5×10^{-4}

Table 6. Significances of intrinsic correlations after common-distance effects are taken into account, for sources in the OVRO sample with known redshift, using 15 GHz concurrent data, as a function of source type and γ -ray energy band.

Source type	Energy Band	Number of sources	Number of z-bins	Spearman ρ	Pearson r	significance
All sources	$E > 0.1$	160	10	0.39	0.46	9.0×10^{-8}
	$0.1 < E < 0.3$	87	5	0.55	0.60	1.3×10^{-6}
	$0.3 < E < 1$	136	10	0.50	0.57	3.0×10^{-8}
	$1 < E < 3$	146	10	0.40	0.47	2.7×10^{-6}
	$3 < E < 10$	104	10	0.22	0.28	0.021
	$10 < E < 100$	29	3	0.06	0.03	0.89
FSRQ	$E > 0.1$	120	10	0.48	0.53	1.4×10^{-7}
	$0.1 < E < 0.3$	67	6	0.56	0.61	9.0×10^{-8}
	$0.3 < E < 1$	104	10	0.54	0.59	4.0×10^{-8}
	$1 < E < 3$	109	10	0.49	0.54	4.9×10^{-6}
	$3 < E < 10$	73	7	0.35	0.39	0.011
	$10 < E < 100$	13	1	0.57	0.46	0.11
BL Lacs	$E > 0.1$	33	3	0.01	0.12	0.57
	$0.1 < E < 0.3$	16	1	0.36	0.44	0.11
	$0.3 < E < 1$	27	2	0.18	0.35	0.17
	$1 < E < 3$	31	3	0.07	0.22	0.27
	$3 < E < 10$	29	2	-0.08	0.05	0.90
	$10 < E < 100$	15	1	-0.15	-0.15	0.57
LSP	$E > 0.1$	114	10	0.43	0.51	5.2×10^{-6}
	$0.1 < E < 0.3$	70	7	0.59	0.62	7.0×10^{-7}
	$0.3 < E < 1$	102	10	0.54	0.60	$< 10^{-7}$
	$1 < E < 3$	106	10	0.47	0.54	5.6×10^{-6}
	$3 < E < 10$	74	7	0.34	0.40	0.025
	$10 < E < 100$	19	1	0.30	0.38	0.11
ISP	$E > 0.1$	11	1	0.13	0.33	0.34
	$0.1 < E < 0.3$		– Not enough sources with redshift –			
	$0.3 < E < 1$	10	1	0.39	0.51	0.20
	$1 < E < 3$	10	1	0.31	0.35	0.36
	$3 < E < 10$	8	1	0.00	0.11	0.80
	$10 < E < 100$		– Not enough sources with redshift –			
HSP	$E > 0.1$	8	1	0.64	0.52	0.18
	$0.1 < E < 0.3$		– Not enough sources with redshift –			
	$0.3 < E < 1$	8	1	0.52	0.44	0.26
	$1 < E < 3$	8	1	0.76	0.50	0.20
	$3 < E < 10$	8	1	0.62	0.44	0.29
	$10 < E < 100$		– Not enough sources with redshift –			

Table 7. Significances of intrinsic correlations after common-distance effects are taken into account, for sources in the OVRO sample with known redshift, using 15 GHz non concurrent data, as a function of source type and γ -ray energy band.

Source type	Energy Band	Number of sources	Number of z-bins	Spearman ρ	Pearson r	significance
All sources	$E > 0.1$	160	10	0.36	0.42	1.9×10^{-6}
	$0.1 < E < 0.3$	87	5	0.47	0.51	7.2×10^{-5}
	$0.3 < E < 1$	136	10	0.45	0.50	2.0×10^{-7}
	$1 < E < 3$	146	10	0.36	0.42	4.1×10^{-5}
	$3 < E < 10$	104	10	0.21	0.25	0.045
	$10 < E < 100$	29	2	-0.06	-0.05	0.78
FSRQ	$E > 0.1$	120	10	0.45	0.50	1.0×10^{-6}
	$0.1 < E < 0.3$	67	6	0.49	0.54	2.5×10^{-6}
	$0.3 < E < 1$	104	10	0.51	0.55	1.5×10^{-6}
	$1 < E < 3$	109	10	0.47	0.51	3.7×10^{-5}
	$3 < E < 10$	73	7	0.35	0.37	0.012
	$10 < E < 100$	13	1	0.34	0.30	0.31
BL Lacs	$E > 0.1$	33	3	-0.02	0.02	0.92
	$0.1 < E < 0.3$	16	1	0.21	0.19	0.49
	$0.3 < E < 1$	27	2	0.05	0.15	0.60
	$1 < E < 3$	31	3	-0.01	0.05	0.80
	$3 < E < 10$	29	2	-0.07	-0.01	0.97
	$10 < E < 100$	15	1	-0.19	-0.22	0.41
LSP	$E > 0.1$	114	10	0.40	0.46	7.1×10^{-5}
	$0.1 < E < 0.3$	70	7	0.50	0.53	6.4×10^{-5}
	$0.3 < E < 1$	102	10	0.46	0.51	2.8×10^{-6}
	$1 < E < 3$	106	10	0.42	0.47	6.7×10^{-5}
	$3 < E < 10$	74	7	0.33	0.34	0.07
	$10 < E < 100$	19	1	0.07	0.20	0.43
ISP	$E > 0.1$	11	1	0.14	0.23	0.50
	$0.1 < E < 0.3$		– Not enough sources with redshift –			
	$0.3 < E < 1$	10	1	0.36	0.36	0.38
	$1 < E < 3$	10	1	0.25	0.17	0.65
	$3 < E < 10$	8	1	0.00	0.06	0.90
	$10 < E < 100$		– Not enough sources with redshift –			
HSP	$E > 0.1$	8	1	0.52	0.48	0.21
	$0.1 < E < 0.3$		– Not enough sources with redshift –			
	$0.3 < E < 1$	8	1	0.69	0.50	0.19
	$1 < E < 3$	8	1	0.57	0.44	0.27
	$3 < E < 10$	8	1	0.43	0.31	0.47
	$10 < E < 100$		– Not enough sources with redshift –			

Table 8. Significances of intrinsic correlations after common-distance effects are taken into account, for sources detected in at least 4 bands, with known redshift, using 8 GHz archival data, as a function of source type and γ -ray energy band.

Source type	Energy Band	Number of sources	Number of z-bins	Spearman ρ	Pearson r	significance
All sources	$E > 0.1$	138	10	0.33	0.38	1.2×10^{-3}
	$0.1 < E < 0.3$	125	10	0.39	0.44	1.4×10^{-4}
	$0.3 < E < 1$	138	10	0.42	0.50	1.5×10^{-5}
	$1 < E < 3$	138	10	0.28	0.36	3.3×10^{-3}
	$3 < E < 10$	138	10	0.12	0.19	0.21
	$10 < E < 100$	52	5	0.11	0.15	0.32
FSRQ	$E > 0.1$	94	9	0.30	0.38	4.5×10^{-4}
	$0.1 < E < 0.3$	93	9	0.34	0.41	1.9×10^{-4}
	$0.3 < E < 1$	94	9	0.30	0.39	2.9×10^{-4}
	$1 < E < 3$	94	9	0.24	0.33	2.2×10^{-3}
	$3 < E < 10$	94	9	0.15	0.23	0.039
	$10 < E < 100$	22	2	0.42	0.39	0.084
BL Lacs	$E > 0.1$	38	3	0.34	0.33	0.19
	$0.1 < E < 0.3$	26	2	0.42	0.42	0.075
	$0.3 < E < 1$	38	3	0.56	0.60	1.2×10^{-3}
	$1 < E < 3$	38	3	0.35	0.38	0.064
	$3 < E < 10$	38	3	0.15	0.18	0.43
	$10 < E < 100$	29	2	0.09	0.09	0.73
LSP	$E > 0.1$	96	9	0.40	0.45	1.4×10^{-3}
	$0.1 < E < 0.3$	93	9	0.40	0.46	3.3×10^{-4}
	$0.3 < E < 1$	96	9	0.37	0.45	1.4×10^{-3}
	$1 < E < 3$	96	9	0.35	0.41	5.8×10^{-3}
	$3 < E < 10$	96	9	0.30	0.34	0.035
	$10 < E < 100$	28	2	0.21	0.35	0.16
ISP	$E > 0.1$	9	1	−0.06	−0.10	0.81
	$0.1 < E < 0.3$	8	1	0.52	0.48	0.23
	$0.3 < E < 1$	9	1	0.25	0.13	0.74
	$1 < E < 3$	9	1	−0.58	−0.42	0.30
	$3 < E < 10$	9	1	−0.45	−0.42	0.27
	$10 < E < 100$		– Not enough sources with redshift –			
HSP	$E > 0.1$	18	1	0.64	0.62	0.01
	$0.1 < E < 0.3$	9	1	0.15	0.003	0.99
	$0.3 < E < 1$	18	1	0.63	0.60	0.017
	$1 < E < 3$	18	1	0.66	0.61	0.013
	$3 < E < 10$	18	1	0.54	0.55	0.032
	$10 < E < 100$	17	1	0.63	0.60	0.018

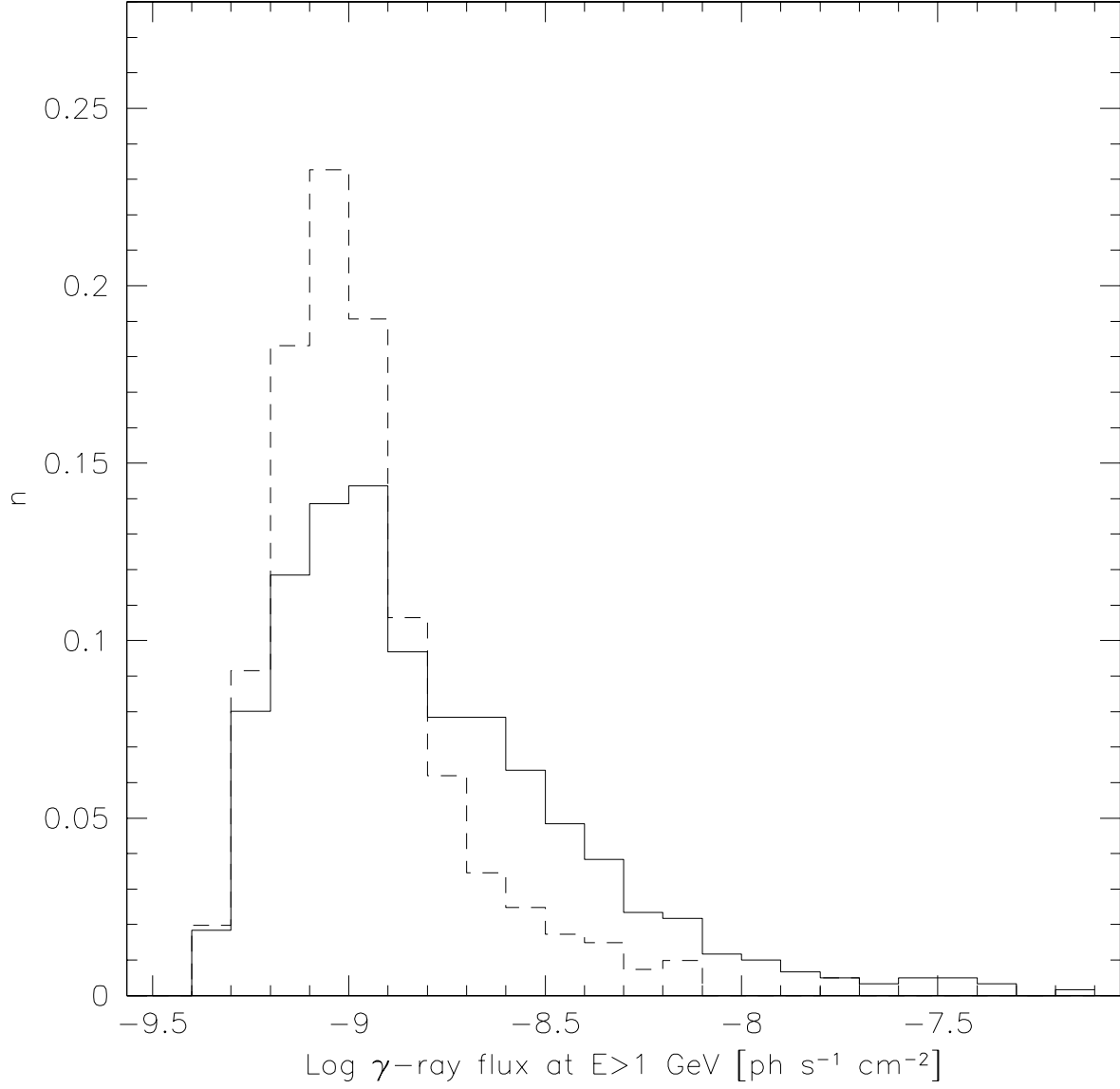


Fig. 1.— Normalized distribution of the gamma-ray photon flux for high latitude ($|b| \geq 10^\circ$) associated (solid line) and unassociated (dashed line) 1FGL sources.

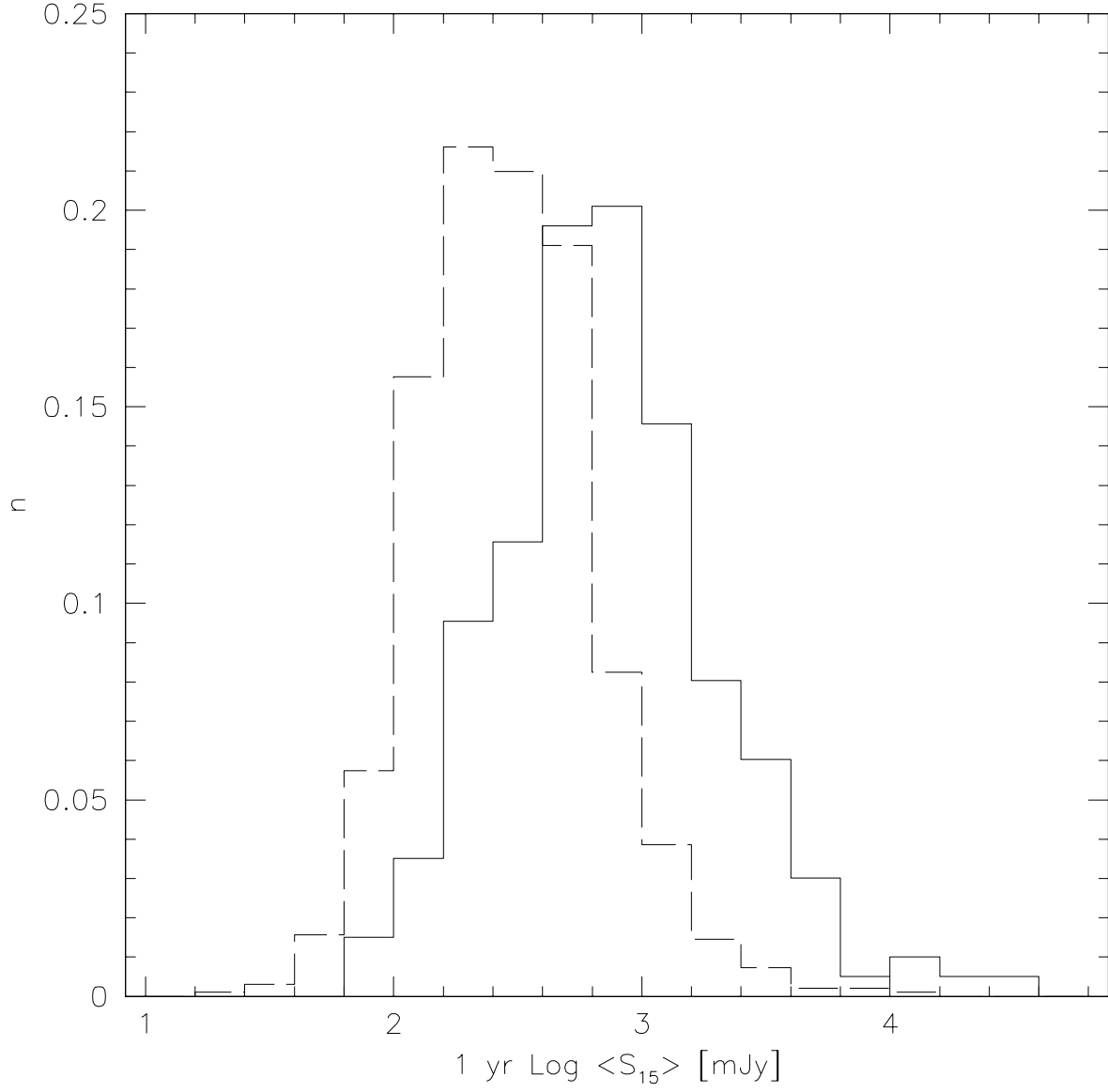


Fig. 2.— Normalized distributions of the average 15 GHz flux densities for CGRABS sources north of declination -20° , shown separately for gamma-ray associated (solid) and unassociated (dashed) sources.

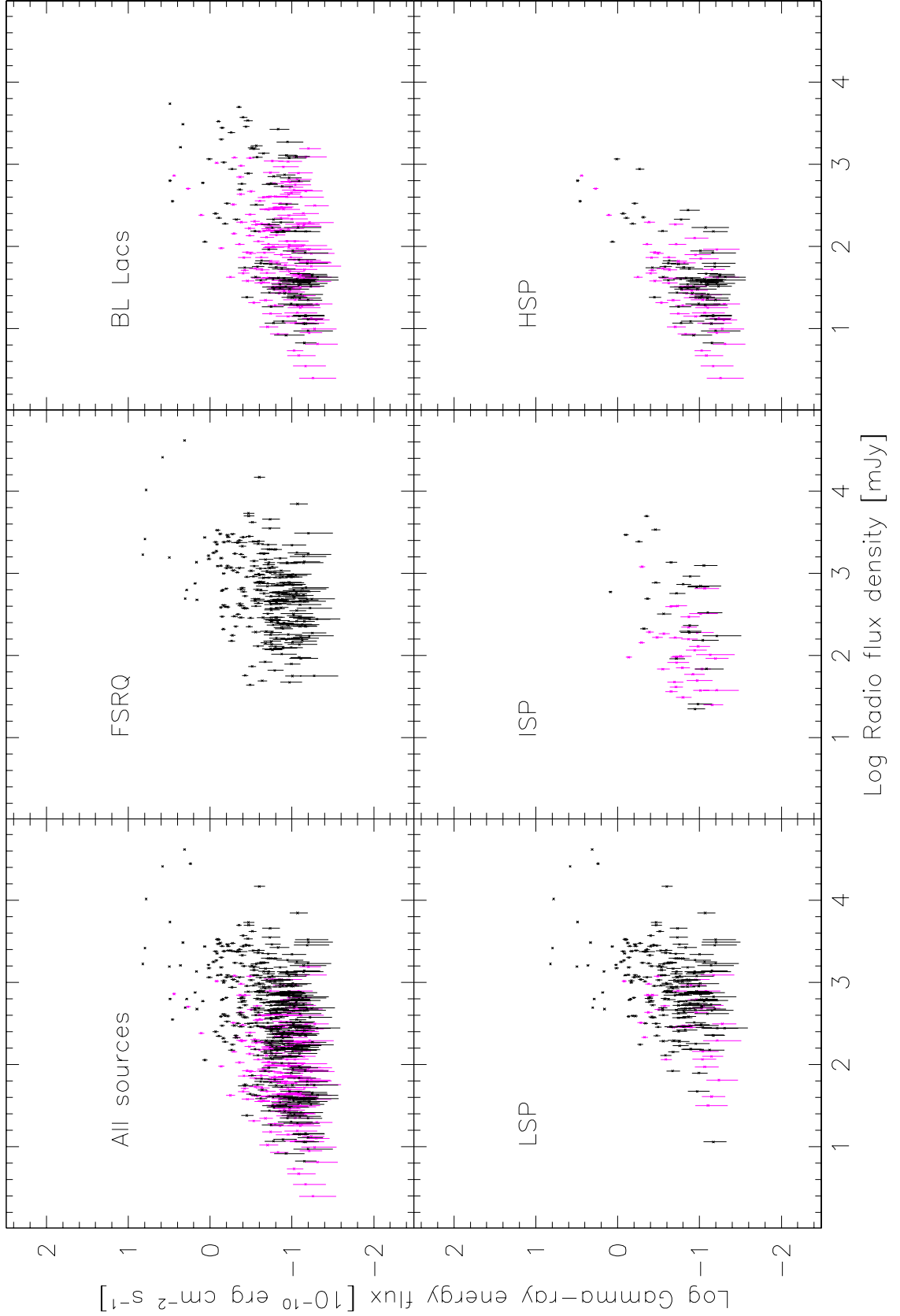


Fig. 3.— Broad band gamma-ray energy flux vs. 8 GHz archival radio flux density for the 1LAC sample, divided by source type. Top, from right to left: all AGNs, FSRQ, BL Lacs; bottom, from right to left: LSP, ISP, and HSP blazars. Sources with unknown redshift are shown in magenta.

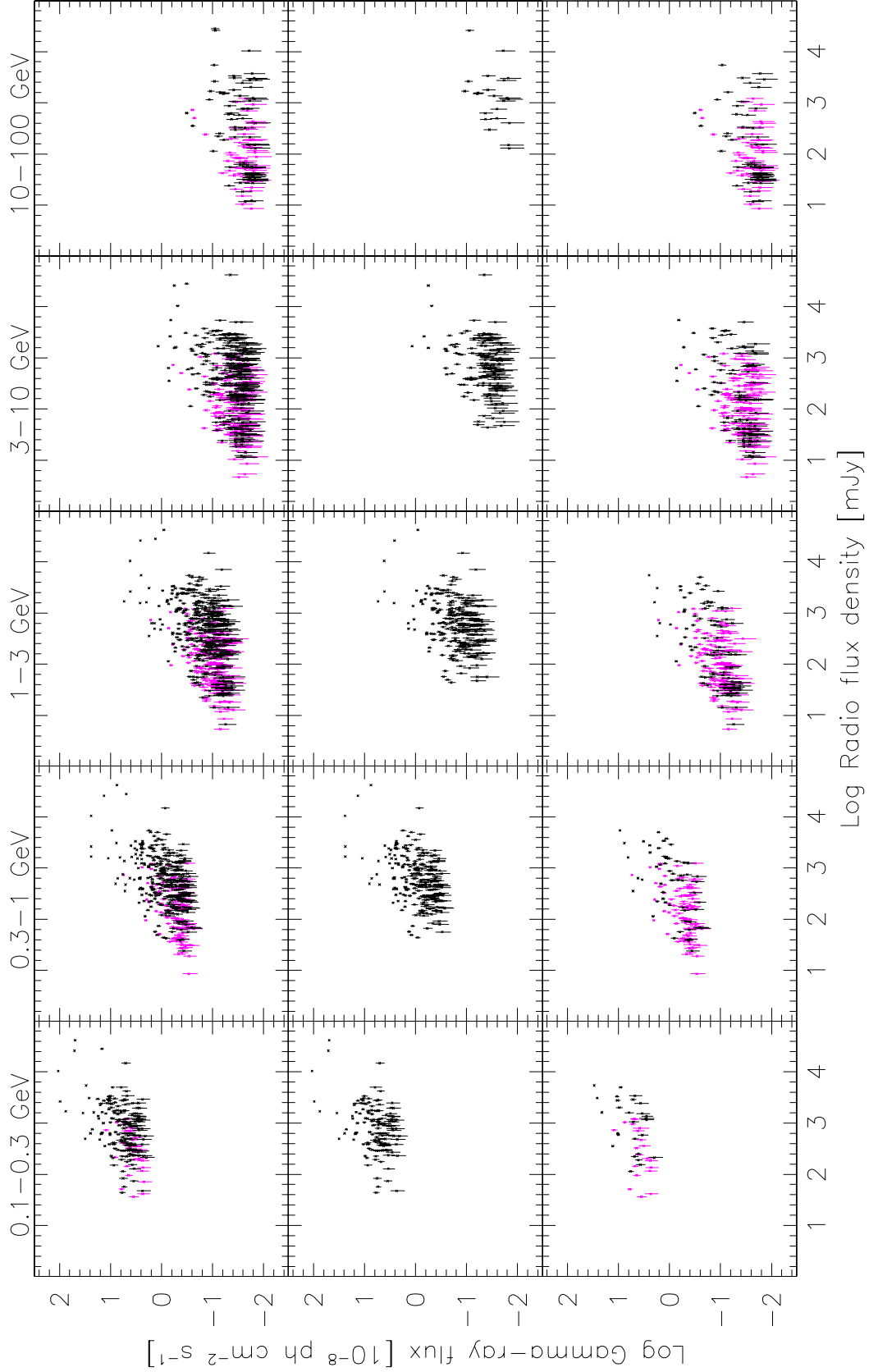


Fig. 4.— Gamma-ray photon flux vs. 8 GHz archival radio flux density for the 1LAC sample, divided by source optical type (top: all sources, middle: FSRQ, bottom: BL Lacs) and in energy bands. Sources with unknown redshift are shown in magenta.

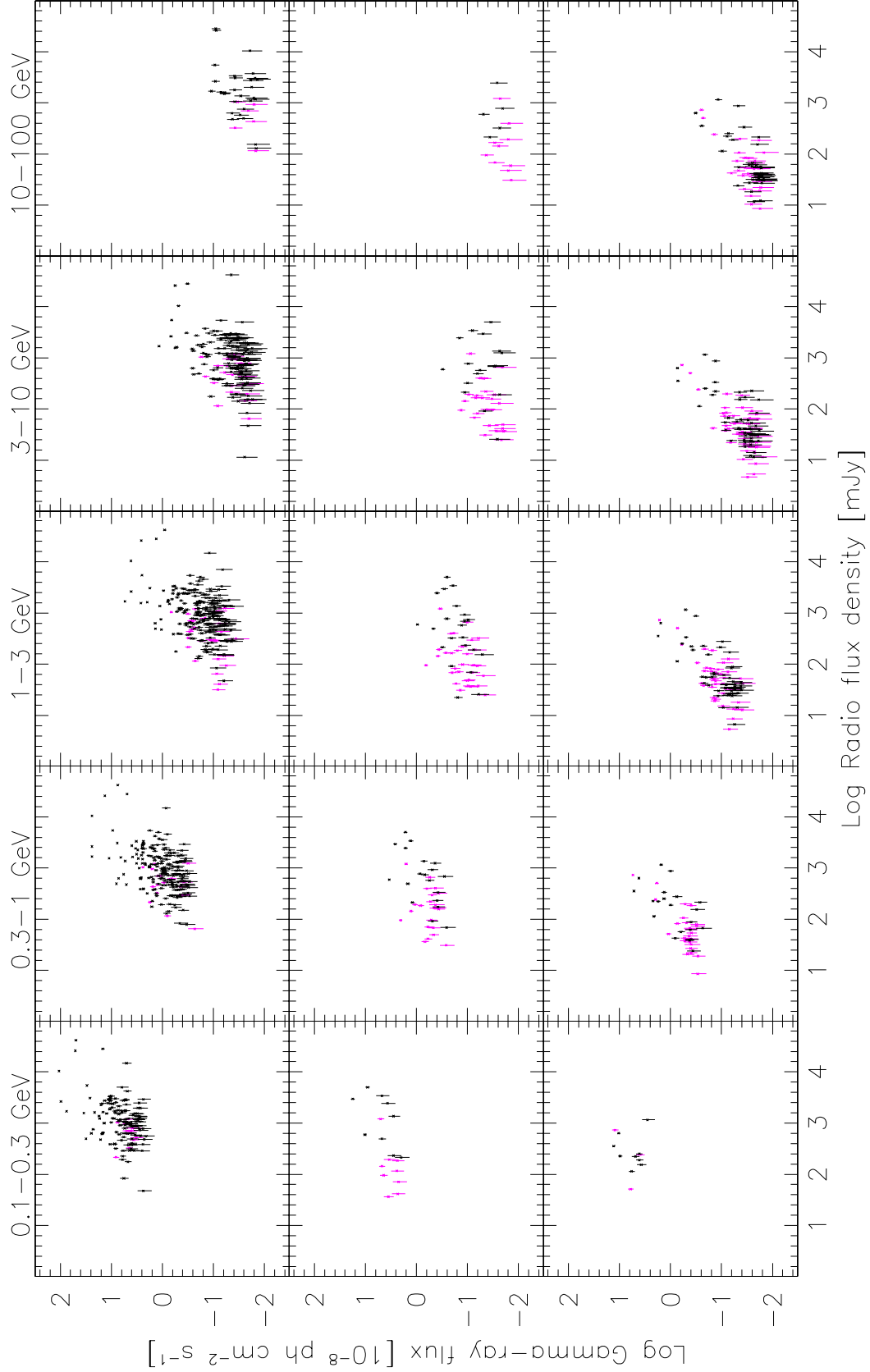


Fig. 5.— Gamma-ray photon flux vs. 8 GHz archival radio flux density for the 1LAC sample, divided by source spectral type (top: LSP, middle: ISP, bottom: HSP) and in energy bands. Sources with unknown redshift are shown in magenta.

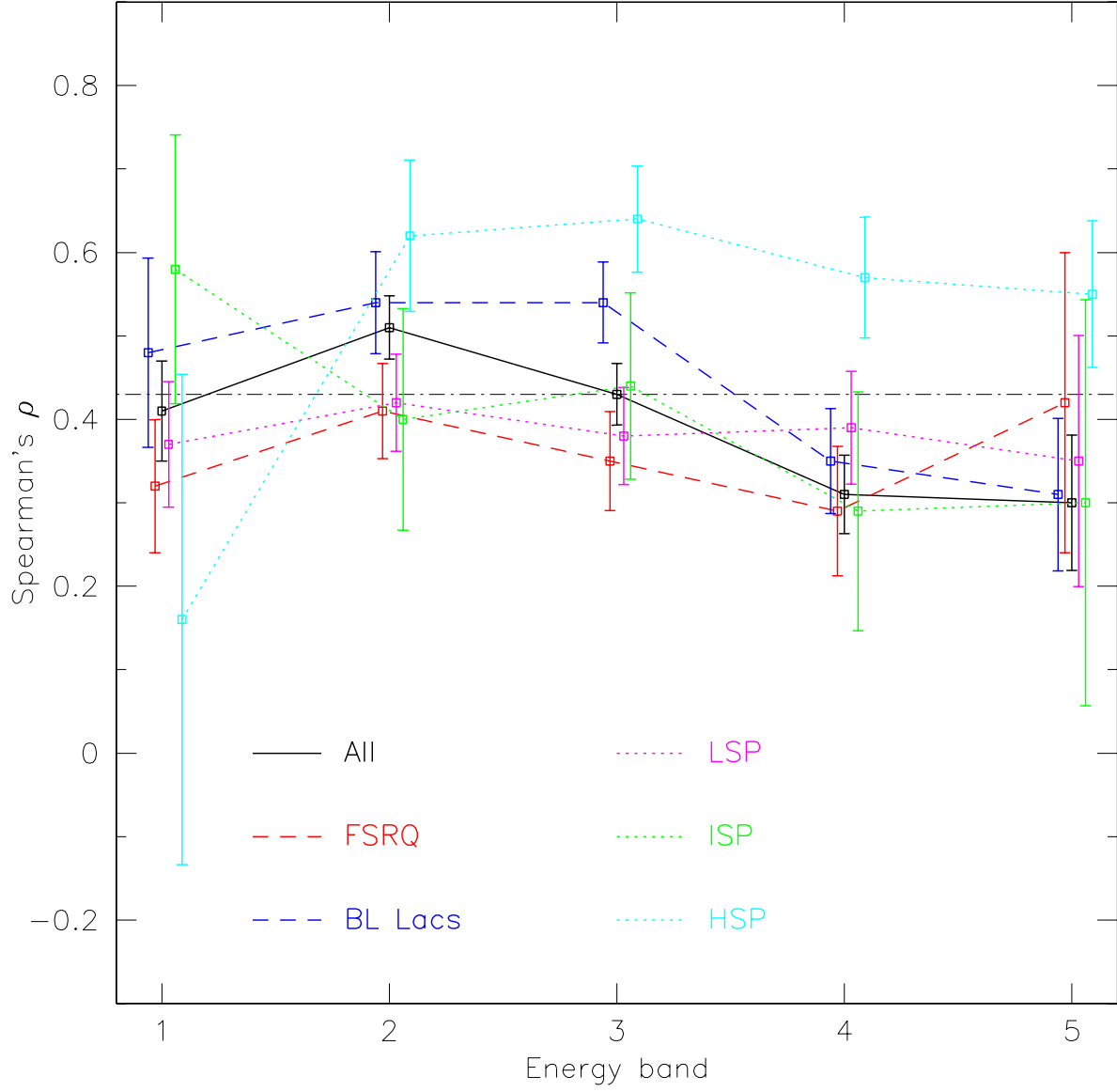


Fig. 6.— Correlation coefficient for the 1LAC sample as a function of the energy bands. Solid black line: all sources; dashed lines: sources divided by optical type: red for FSRQs and blue for BL Lacs; dotted lines: sources divided by spectral type (LSP in magenta, ISP in green, HSP in cyan). The dot-dash black line shows as a reference the value of ρ obtained using all sources and broad band gamma-ray flux. At each x -point (energy band), symbols are horizontally offset for improved clarity.

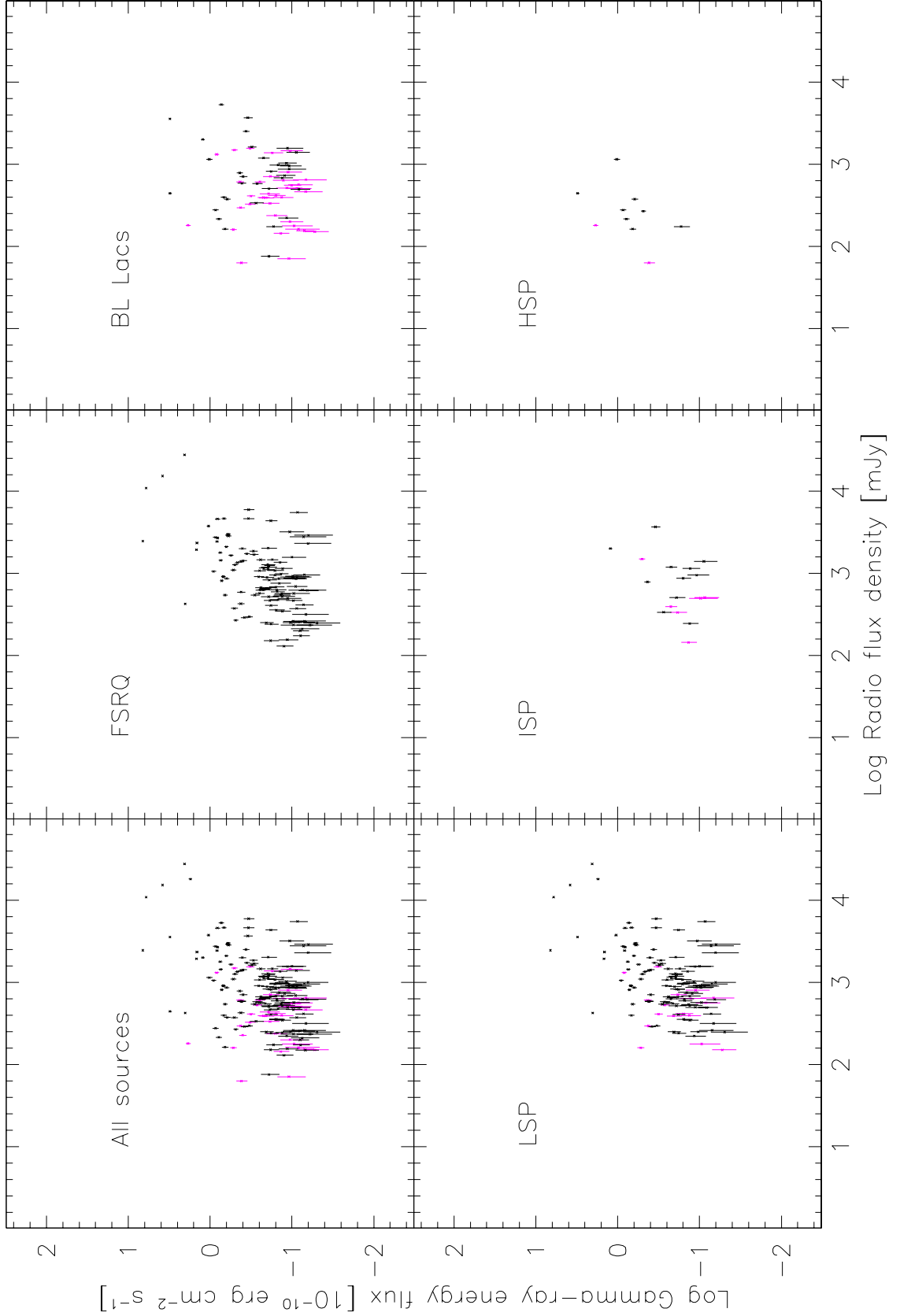


Fig. 7.— Broad band gamma-ray energy flux vs. concurrent 15 GHz mean radio flux density for OVRO sources, divided by source type. Top, from right to left: all AGNs, FSRQ, BL Lacs; bottom, from right to left: LSP, ISP, and HSP blazars. Sources with unknown redshift are shown in magenta.

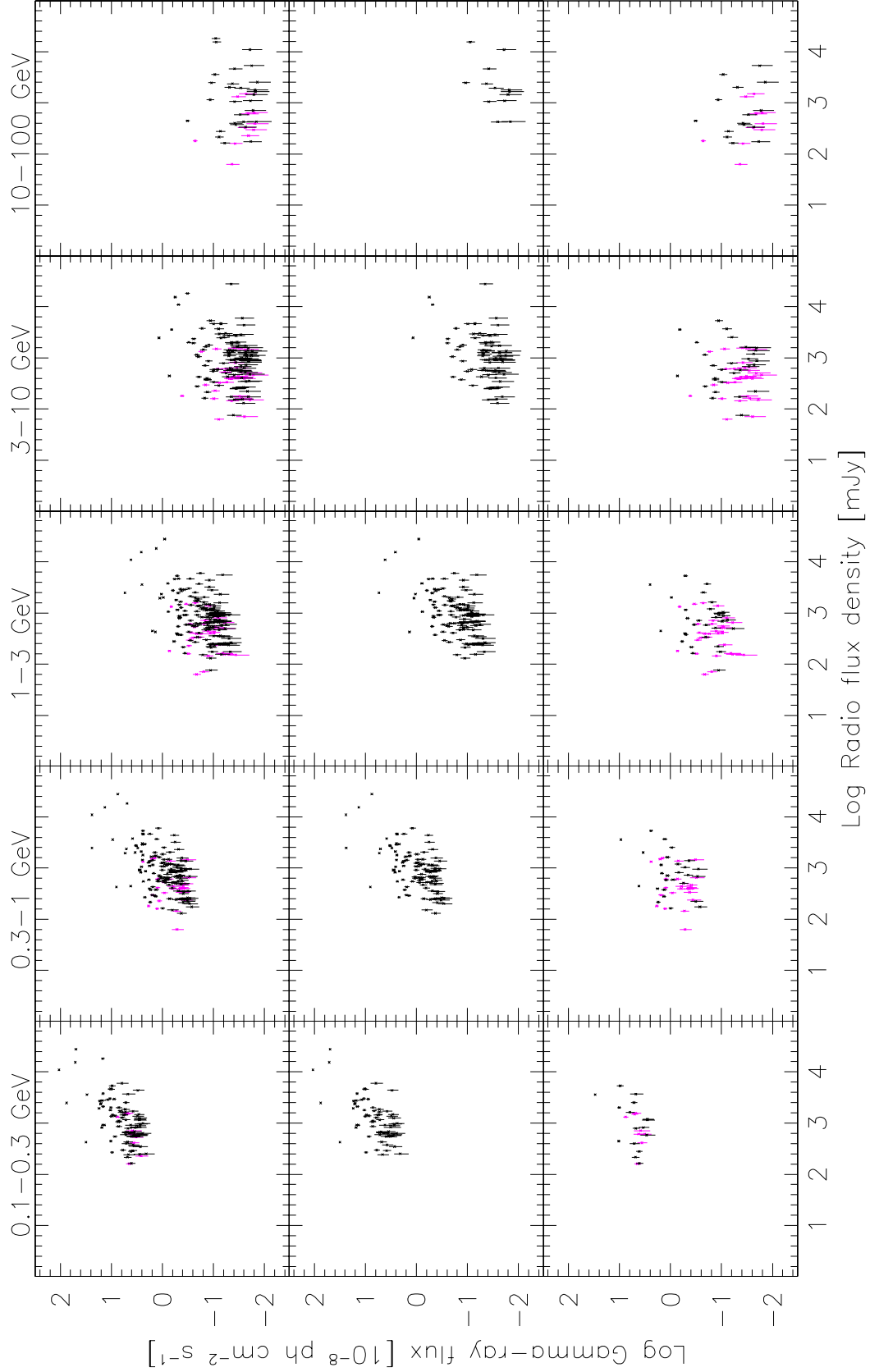


Fig. 8.— Gamma-ray photon flux vs. concurrent 15 GHz mean radio flux density for OVRO sources, divided by source optical type (top: all sources, middle: FSRQ, bottom: BL Lacs) and in energy bands. Sources with unknown redshift are shown in magenta.

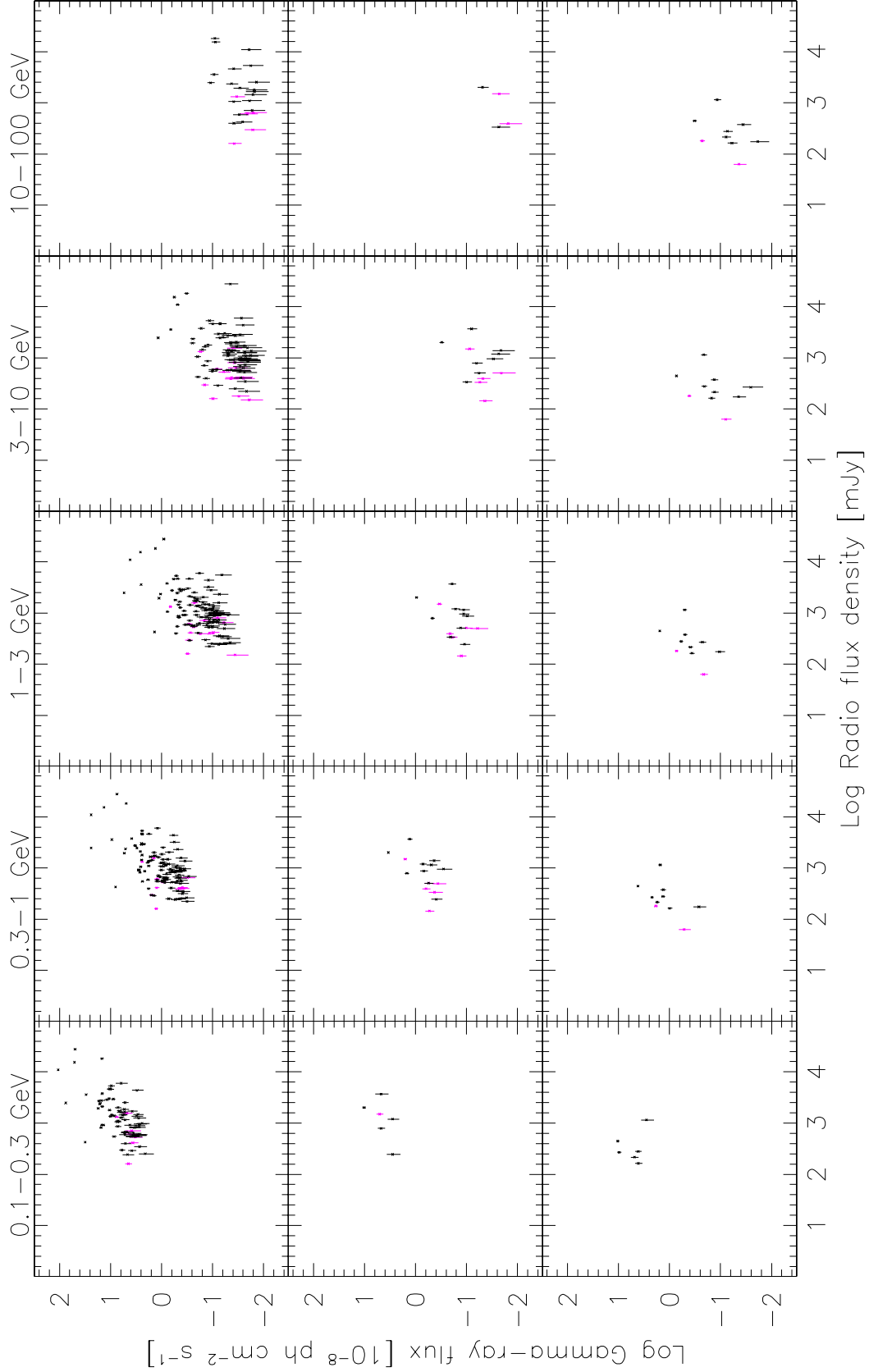


Fig. 9.— Gamma-ray photon flux vs. concurrent 15 GHz mean radio flux density for OVRO sources, divided by source spectral type (top: LSP, middle: ISP, bottom: HSP) and in energy bands. Sources with unknown redshift are shown in magenta.

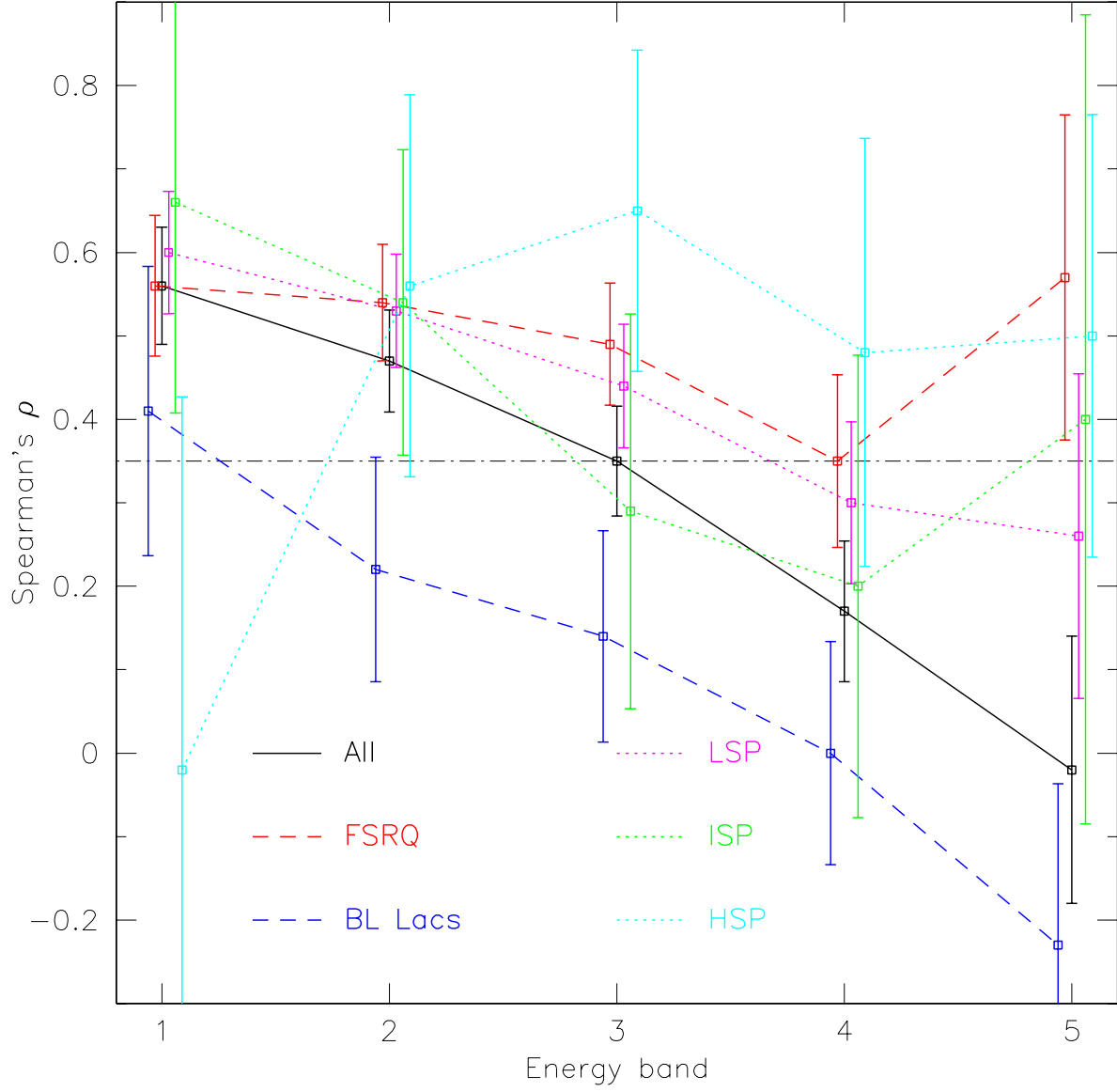


Fig. 10.— Correlation coefficients for the OVRO sample (concurrent radio and gamma-ray data) as a function of energy bands. Solid black line: all sources; dashed lines: sources divided by optical type: red for FSRQs and blue for BL Lacs; dotted lines: sources divided by spectral type (LSP in magenta, ISP in green, HSP in cyan). The dot-dash black line shows as a reference the value of ρ obtained using all sources and broad band gamma-ray flux. At each x -point (energy band), symbols are horizontally offset for improved clarity.

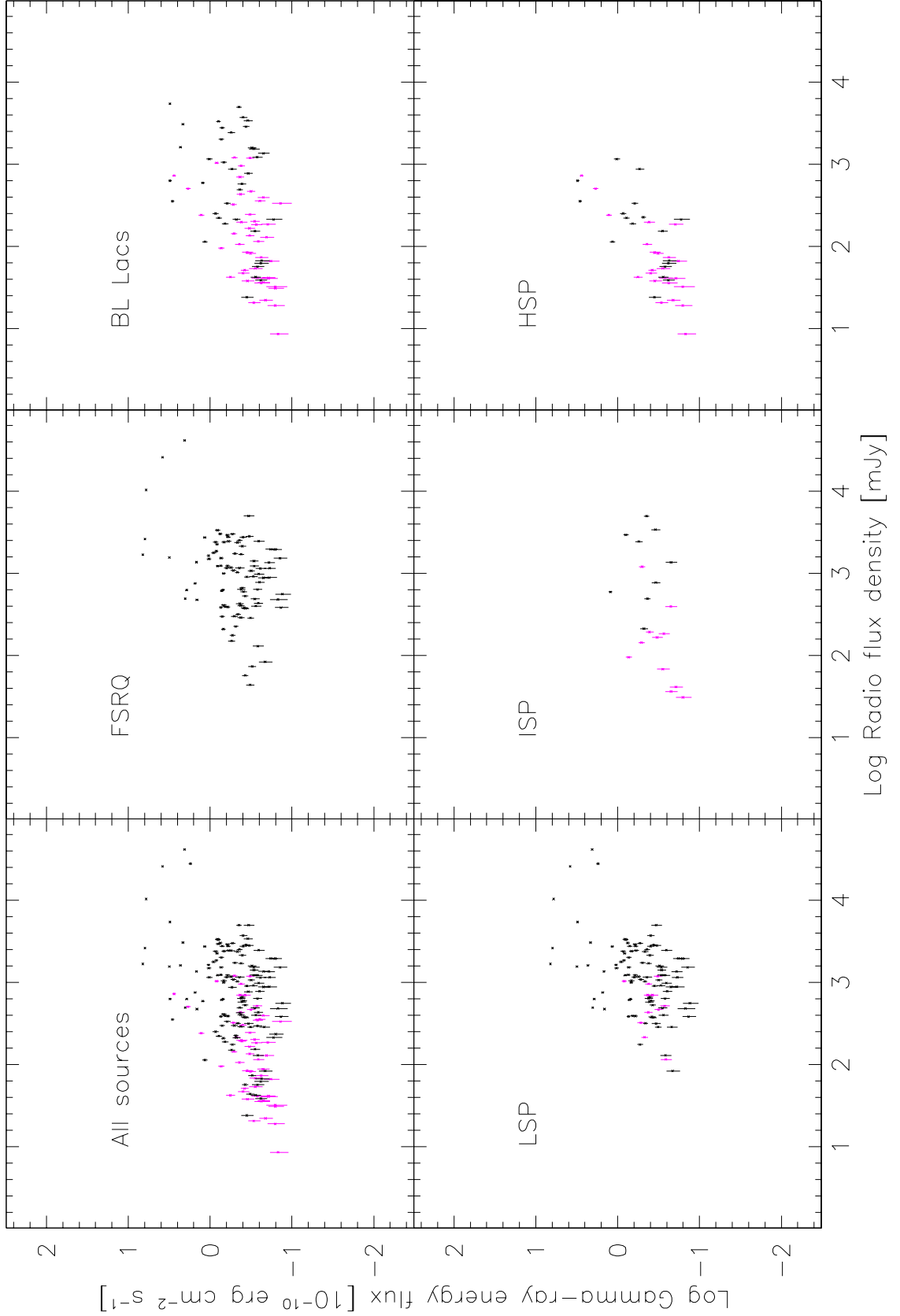


Fig. 11.— Broad band gamma-ray energy flux vs. 8 GHz archival radio flux density for sources in the 1LAC with a detection in at least 4 energy bands, divided by source type. Top, from right to left: all AGNs, FSRQ, BL Lacs; bottom, from right to left: LSP, ISP, and HSP blazars. Sources

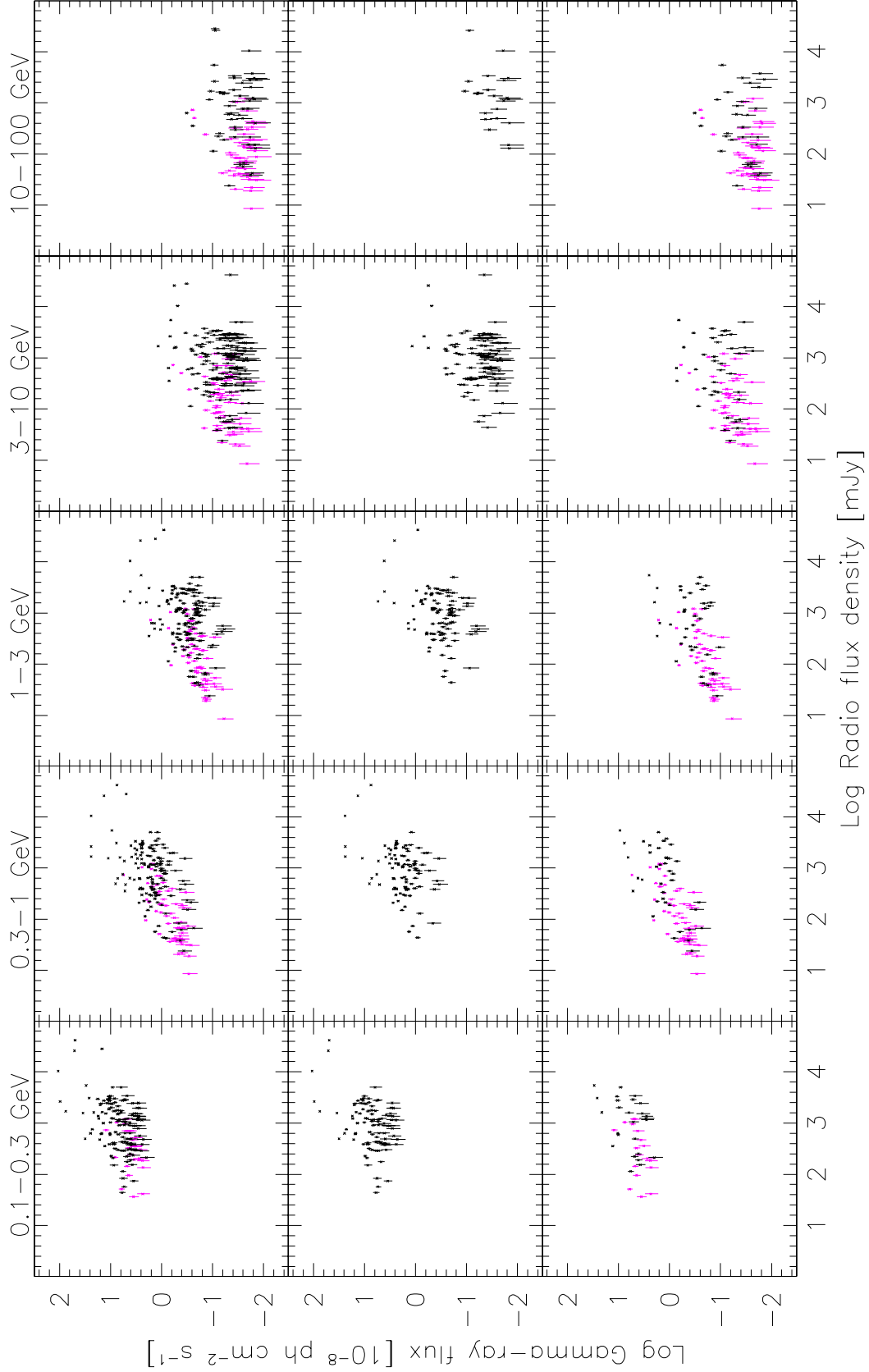


Fig. 12.— Gamma-ray photon flux vs. 8 GHz radio flux density for sources in the 1LAC with a detection in at least 4 energy bands, divided by source optical type (top: all sources, middle: FSRQ, bottom: BL Lacs) and in energy bands. Sources with unknown redshift are shown in magenta.

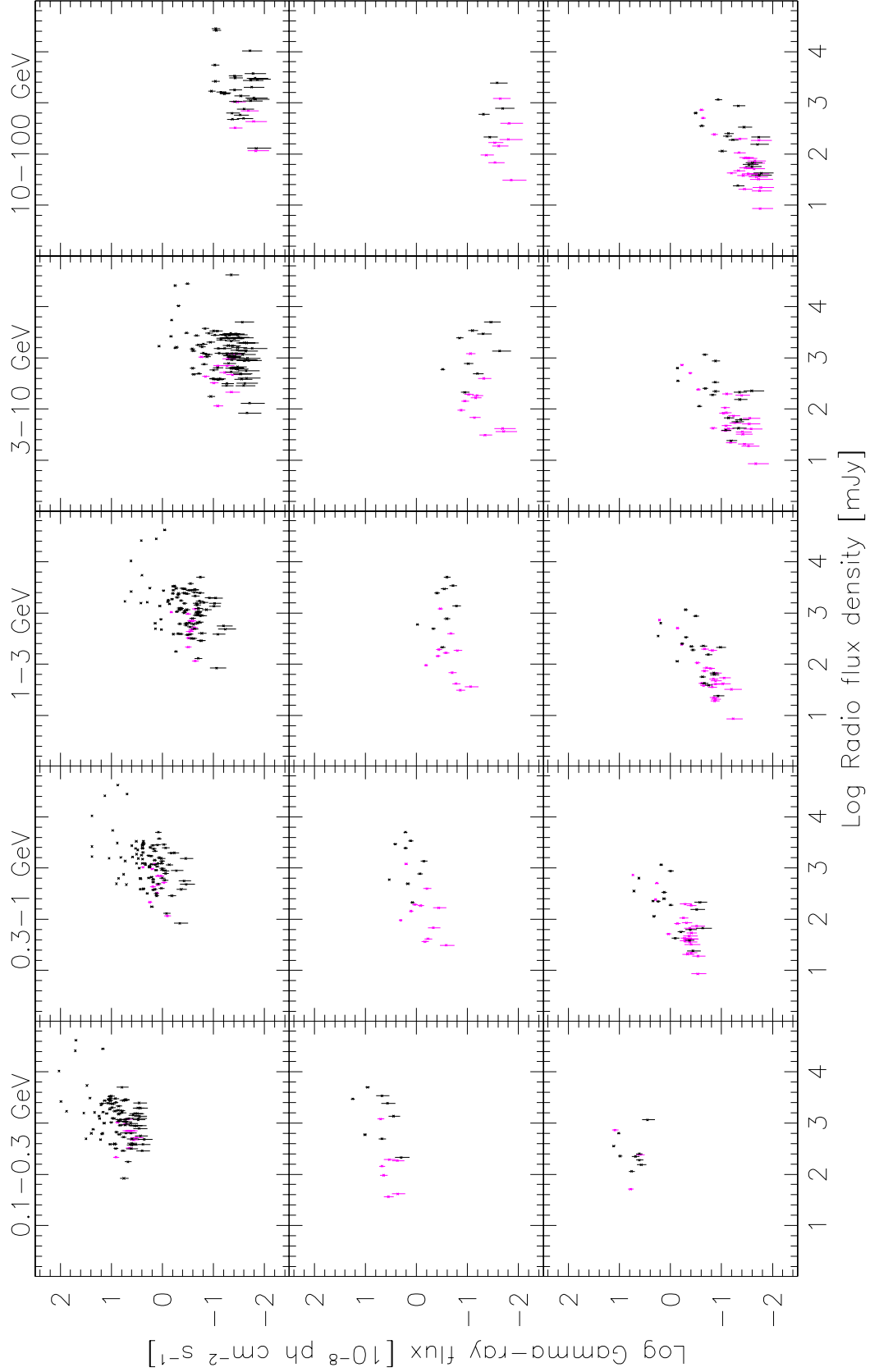


Fig. 13.— Gamma-ray photon flux vs. 8 GHz radio flux density for sources in the 1LAC with a detection in at least 4 energy bands, divided by source spectral type (top: LSP, middle: ISP, bottom: HSP) and in energy bands. Sources with unknown redshift are shown in magenta.

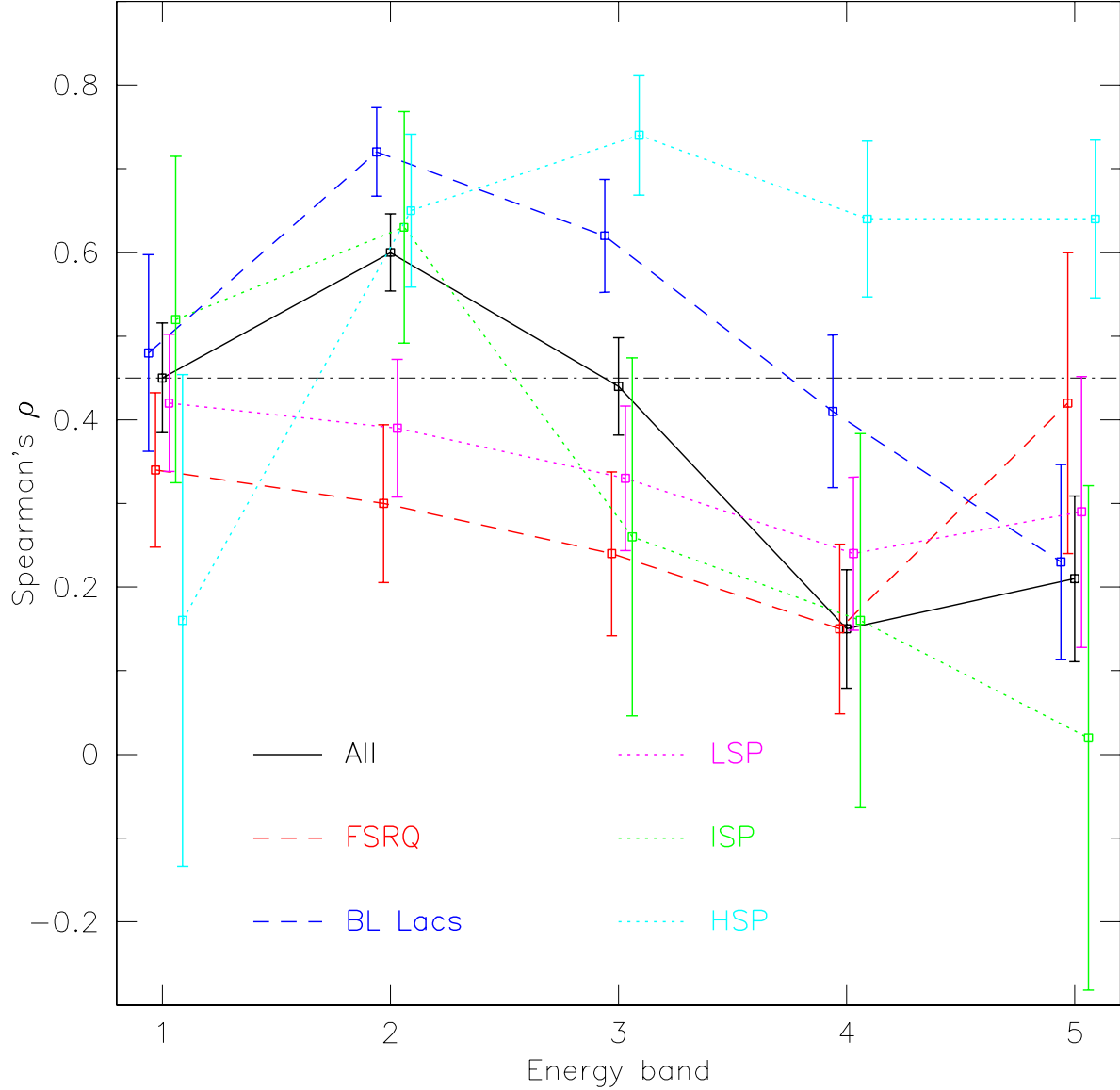


Fig. 14.— Correlation coefficient for sources in the 1LAC with a detection in at least 4 energy bands, as a function of the energy bands. Solid black line: all sources; dashed lines: sources divided by optical type: red for FSRQs and blue for BL Lacs; dotted lines: sources divided by spectral type (LSP in magenta, ISP in green, HSP in cyan). The dot-dash black line shows as a reference the value of ρ obtained using all sources and broad band gamma-ray flux. At each x -point (energy band), symbols are horizontally offset for improved clarity.

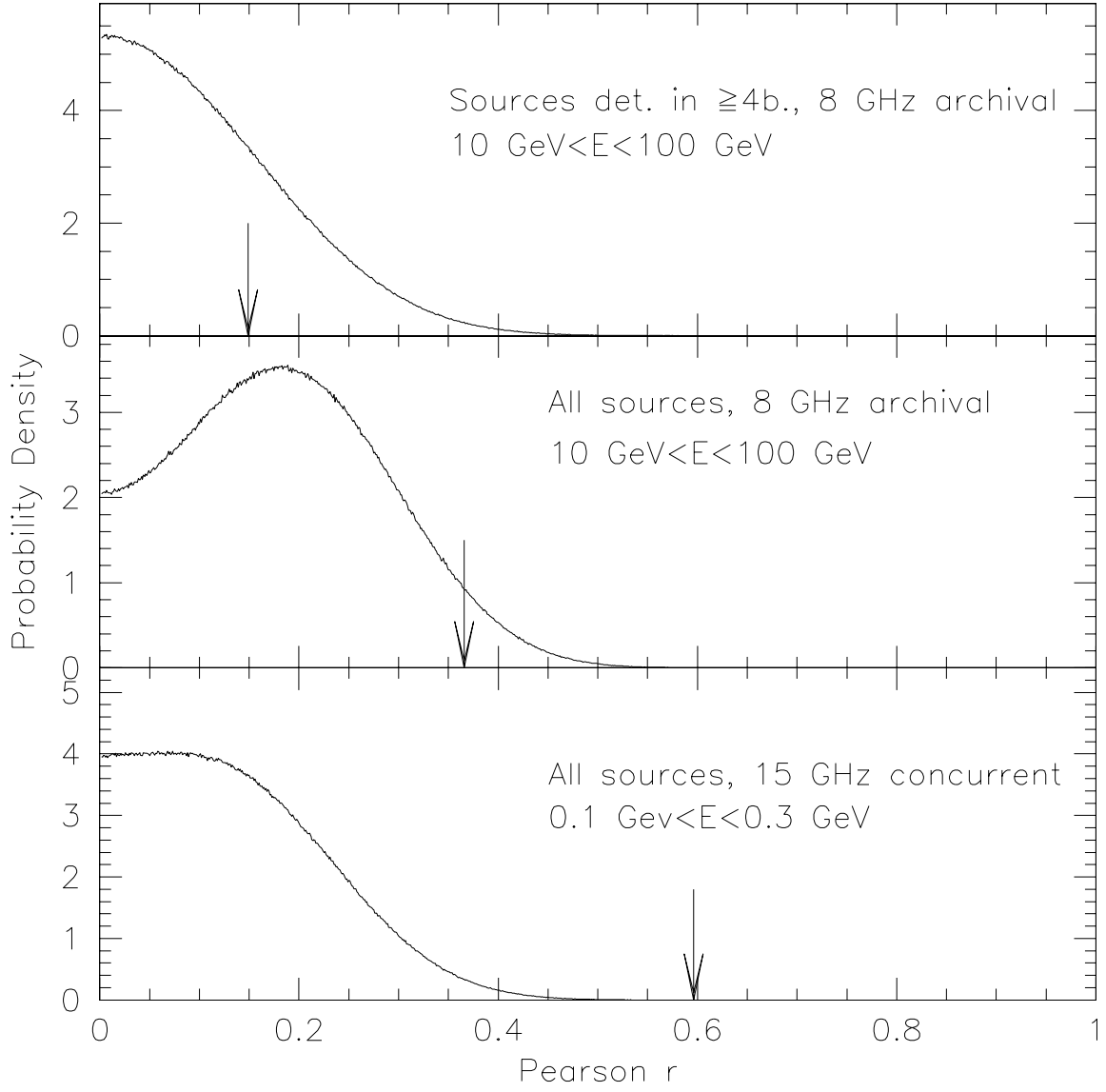


Fig. 15.— Probability density distributions of the absolute value of the Pearson product-moment r for three simulated datasets, with low (top panel), medium (middle), and high (bottom) correlation significance.

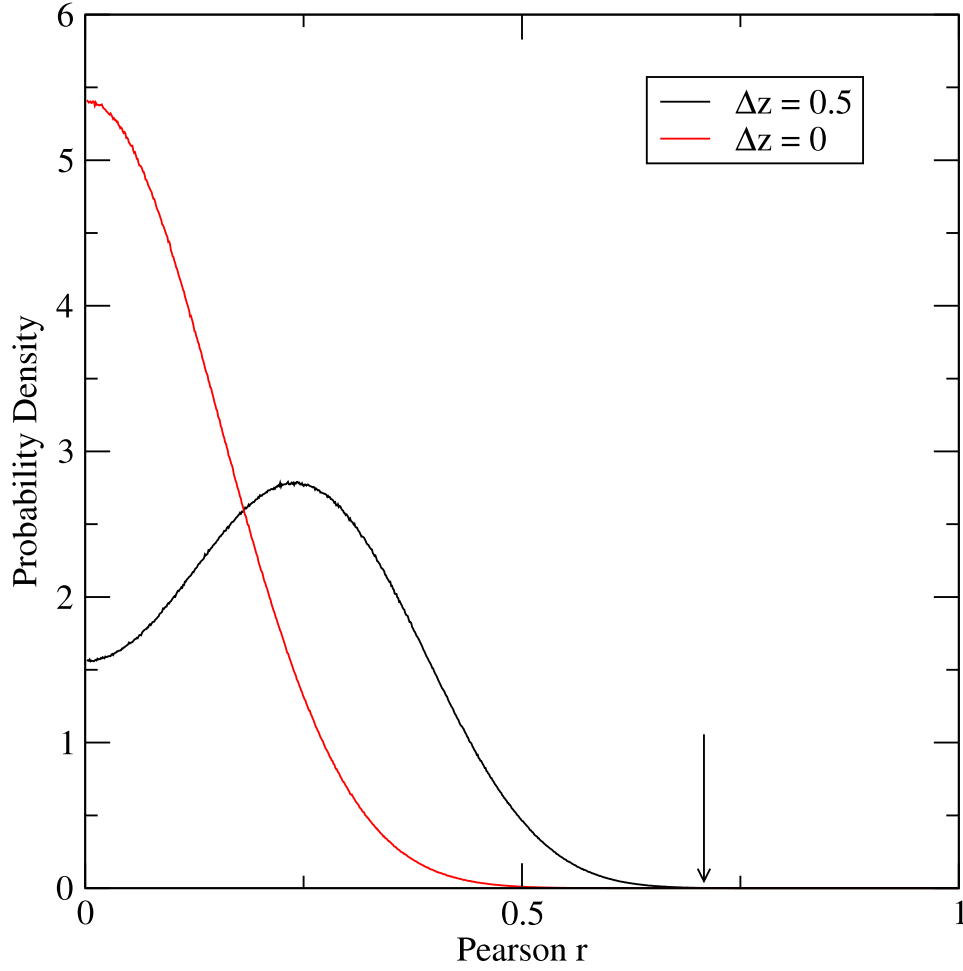


Fig. 16.— Probability density distribution of the absolute value of the Pearson product-moment r for HSP blazars using 8 GHz archival data and 10–100 GeV gamma-ray flux density, assuming that the sources without redshift follow the same redshift distribution of the ones with known z (red solid line) or with a mean shift of $\Delta z = 0.5$ (black solid line).